UNIVERSIDAD DE LAS PALMAS DE GRAN CANARIA

DOCTORAL THESIS

Shedding light into mesoscale dynamics and vertical motion through synthetic and *in situ* observations

---

Author:
Bàrbara BARCELÓ-LLULL

Supervisor:
Dr. Pablo SANGRÀ
Co-Supervisors:
Dr. Enric PALLÀS-SANZ
Dra. Ananda PASCUAL
Dra. Ángeles MARRERO-DÍAZ

Programa Oficial de Doctorado en Oceanografía
Facultad de Ciencias del Mar

May 22, 2017

UNIVERSIDAD DE LAS PALMAS DE GRAN CANARIA

Facultad de Ciencias del Mar

Programa de doctorado de Oceanografía

Título de la Tesis

Shedding light into mesoscale dynamics and vertical motion through synthetic and *in situ* observations

Tesis Doctoral presentada por D^{a} Bàrbara BARCELÓ-LLULL

Dirigida por el Dr. Pablo SANGRÀ

Codirigida por los Drs. Enric PALLÀS-SANZ, Ananda PASCUAL, Ángeles MARRERO-DÍAZ

Enric Pallàs Sanz Ananda Pascual Ascaso Ángeles Marrero Díaz Bàrbara Barceló Llull

El Director Los Codirectores La Doctoranda

Las Palmas de Gran Canaria, a 12 de mayo de 2017

A en Joan, sa dolçor de sa meva vida.

Avui, sabeu? les fades i les bruixes s'estimen.
Han canviat entre elles escombres i varetes.
I amb cucurull de nit i tarot de poetes
endevinen l'enllà, on les ombres s'animen.

És que han begut de l'aigua de la Font dels Lilàs
i han parlat amb la terra, baixet, arran d'orella.
Han ofert al no-res foc de cera d'abella
i han aviat libèl·lules per desxifrar-ne el traç.

Davallen a la plaça en revessa processó,
com la serp cargolada entorn de la pomera,
i enceten una dansa, de punta i de taló.

Jo, que aguaito de lluny la roda fetillera,
esbalaïda veig que vénen cap a mi
i em criden perquè hi entri. Ullpresa, els dic que sí.

Avui les fades i les bruixes s'estimen
Maria Mercè Marçal i Serra

Abstract

Mesoscale oceanic structures have a key role on the oceanic global circulation through the enhancement of large-scale fluxes of heat, salt, momentum, and biogeochemical tracers. Moreover, mesoscale vertical motions may have an important contribution on the nutrient replenishment of the euphotic layer, and, hence, on marine ecosystems. Furthermore, mesoscale coherent features, or eddies, have the capacity to trap fluid of their formation regions within their cores and propagate offshore over long distances. However, despite their importance, the mechanisms through which mesoscale structures, as mesoscale eddies, influence marine ecosystems are still under discussion. In this dissertation we aim to shed some light on the thermohaline and dynamical structure, including ageostrophic secondary circulation, of mesoscale features through remote sensing observations and *in situ* data, paying special attention to mesoscale eddies and induced vertical motions. To achieve this goal, the thesis is developed in four chapters self-contained, three of them are already published. First, we demonstrate the importance of mesoscale vertical motions on nutrient distribution in an oligotrophic region of the global ocean through synthetic observation-based data. Vertical motions may account for local increases of nitrate uptake rates of up to 30% in regions with mesoscale activity. Then, we take advantage of the high-resolution *in situ* data obtained from the intensively sampling of a mesoscale eddy within the Canary Eddy Corridor, the main pathway for long-lived eddies in the northeast Atlantic which constitutes a natural laboratory for the study of these structures. With these data we analyze in detail the anatomy of the eddy, revealing its main hydrographic and dynamic characteristics. Thirdly, as the eddy is moderately ageostrophic, we estimate and analyze its ageostrophic secondary circulation, revealing for the first time the distribution of the vertical velocity field within a mesoscale eddy through high-resolution *in situ* data. Finally, we perform a comparison of the synthetic observation-based product with the *in situ* data obtained from the cruise, evaluating the capacity of the synthetic fields to reproduce the eddy hydrodynamic structure.

Acknowledgements

En primer lugar mi más profundo agradecimiento es para mi director de tesis, Pablo Sangrà. Me siento muy afortunada por haber tenido la gran oportunidad de realizar el doctorado al amparo de esta mente tan brillante. Además de la formación a nivel profesional que me ha brindado, también cabe destacar lo aprendido a nivel personal. De nuestras reuniones, además de conocimientos científicos, también he obtenido un inmenso enriquecimiento personal gracias a su manera de tratarnos, siempre alegre y respetuoso, a su manera de valorar nuestras ideas e iniciativas, a su manera de tranquilizarnos, y a su manera de trabajar y de vivir. Porque algo que he aprendido de él es la importancia de disfrutar de todos los momentos que nos brinda la vida, así como también el ser una persona respetuosa y atenta con los demás. Su confianza en mí y su enseñanza me han dado la fuerza necesaria para terminar la tesis con toda la decisión y motivación posible. Solo espero que cada uno de los momentos vividos con esta gran persona, junto con sus respectivas enseñanzas, me acompañen siempre. Gràcies de tot cor Pablo! T'enyor molt!

I com que es tracta de disfrutar la vida, Enric, moltes gràcies per acollir-nos tant bé a Mèxic! Gràcies a les estades que he fet amb tu he pogut completar les anàlisis de PUMP, he après un munt sobre l'equació omega i he conegut el CICESE, Mèxic, diferents maneres de viure i una gent meravellosa. Ananda, com sempre, gràcies per salvar-me i introduir-me a aquest món que m'apassiona i em fa sentir tant realitzada. Gràcies per les estades al IMEDEA i per donar-me l'ajuda necessària per completar la tesis. Ángeles, gracias por cogerme de la mano y tirar de mí con fuerza en esta última fase de mi tesis. Te estoy muy agradecida por todo lo que estás haciendo por mí. Evan, també vull agrair el teu suport continu i les teves ensenyances, sempre aprenc molt de tu.

También agradezco el apoyo y la amistad del PUMP team. Estoy muy orgullosa del buen equipo que formamos y de las buenas amistades que han nacido de la campaña PUMP.

Agradezco el cariño y la amistad de mis compañeros del IMEDEA y del CICESE. La amistad no entiende de distancias.

Gracias a mis compañeras y a mi maestra de costura, por alegrar los lunes con risas, té, aguja e hilo. Gracias Araceli por tus bendiciones, por tu cariño y amistad, y por abrirnos las puertas de tu casa y poder conocer a tu hermosa familia. Gracias a mi entrenador, Fran, por mantener mi cordura con la locura de sus entrenamientos. Gracias a nuestros amigos salseros por la alegría, las confidencias y los bailes compartidos.

Gràcies a la família que em recolza cada dia i m'estima així com som. Gràcies als meus pares per haver fet tot el possible per oferir-nos una vida millor. Gràcies al meu germà per ser-hi.

Gracias a nuestros vecinos que nos han acogido en el seno de su familia con todo el cariño del mundo. Desde la llegada a esta isla habéis formado parte de nuestro día a día, hemos compartido mucho juntos y os llevaremos en nuestro corazón siempre. Gracias de corazón!

I, finalment, gràcies a s'amor de sa meva vida, en Joan. Gràcies amor meu per donar-me tantíssim cada dia. Gràcies pes teu suport infinit, per s'amor, ses atencions, ses rialles, ses mirades... i per tot allò que no es pot dir amb paraules. T'ador i t'estim!

Contents

List of Figures

List of Tables

Part I

General introduction to the dissertation

General introduction

Mesoscale dynamics and vertical motion

Mesoscale oceanic structures, such as fronts and eddies, have an important role on the oceanic global circulation through the enhancement of large-scale fluxes of heat, salt, momentum, and biogeochemical tracers (Danabasoglu et al., 2012, 2008; Jochum et al., 2008; Griffies, 2004). Moreover, these structures drive strong horizontal and vertical motions that have an important influence on biological processes (McGillicuddy, 2016; Rodríguez et al., 2001; Mahadevan and Archer, 2000). Coastal upwelling (Figure 1) and frontal areas are examples of mesoscale structures with intense vertical velocities that may contribute to the nutrient enrichment of the euphotic layer (Mahadevan, 2014). This nutrient replenishment may, in turn, enhance phytoplankton growth and impact on marine ecosystems.

A particular type of mesoscale structures are eddies, coherent features of the order of 100 km that trap fluid of their formation regions within their cores (e.g. Chelton et al., 2011b). Mesoscale eddies can move offshore during months, or even years, with a tangential velocity higher than the translation speed. Accordingly, eddies can transport heat, mass, and biogeochemical tracers within their cores over long distances and, hence, they may have an important contribution on the thermohaline general circulation, water mass distribution, and ocean biology (McWilliams, 2008). Moreover, vertical velocities within mesoscale eddies may have an important role on the vertical exchange of heat, salinity, and biogeochemical tracers between the deep ocean and the upper layers (McGillicuddy, 2016). However, a high uncertainty still exists in our understanding of the mechanism through which mesoscale structures, as mesoscale eddies, influence marine ecosystems.

Several hypotheses have been proposed to explain the mechanisms through which mesoscale eddies affect ocean ecosystems (McGillicuddy, 2016; Klein and Lapeyre, 2009). Simple conceptual models such as eddy pumping (McGillicuddy et al., 1998; Siegel et al., 1999; Mahadevan et al., 2012), eddy-wind interaction (Martin and Richards, 2001; McGillicuddy et al., 2007; Benítez-Barrios et al., 2011; Gaube et al., 2013), and eddy stirring (Siegel et al., 2008; Chelton et al., 2011a) have been widely discussed. However, more detailed analyses based on both modeling and

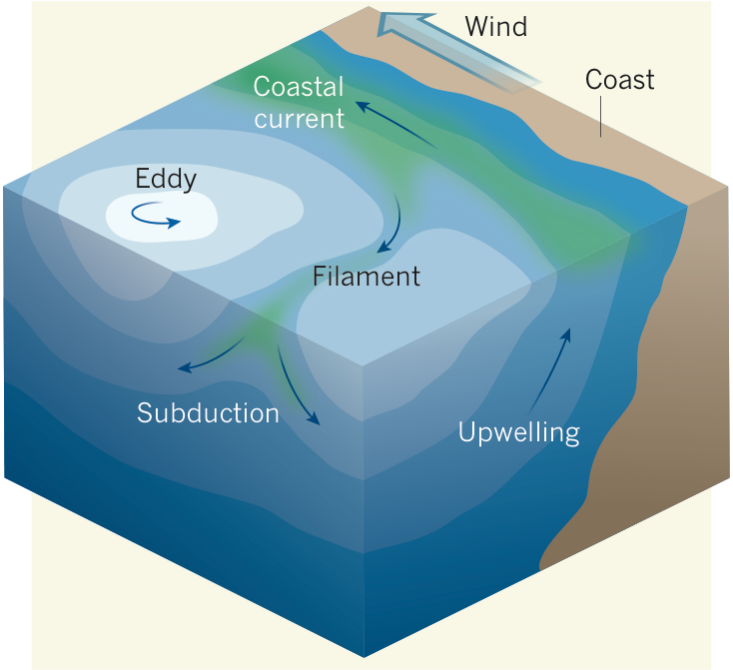

FIGURE 1: Eastern ocean margin with upwelling due to the equatorward along-shore winds in the southern hemisphere. Ekman transport causes divergence and upwelling, which brings colder, denser and nutrient-rich deep water to the surface. The developed coastal current is unstable and generates filaments and eddies. (Mahadevan, 2014)

observational approaches suggest that these simplified models are not able to provide an accurate picture of the 3D velocity field at mesoscale, highlighting the fundamental role played by quasi-geostrophic (QG) and semi-geostrophic (SG) dynamics (e.g. Tintoré et al., 1991; Pollard and Regier, 1992; Naveira Garabato et al., 2001; Pidcock et al., 2013). These advanced analyses also propose new mechanisms that may modulate vertical exchanges inside mesoscale oceanic eddies, such as submesoscale pumping (e.g. Lévy et al., 2001; Calil and Richards, 2010) and the occurrence of vortex Rossby waves (Koszalka et al., 2009, 2010; Cardona and Bracco, 2012; Buongiorno Nardelli, 2013).

Although mesoscale vertical motions induce important vertical exchanges, they are usually four orders of magnitude smaller than horizontal currents W$\sim$(10^{-3}-10^{-4})U$\sim$10 m d^{-1}. Because of this, direct measurements of vertical velocities in the ocean are difficult to obtain and they are generally determined indirectly through analyses of hydrographic and dynamic observations and assuming balance conditions for the flow. The most widely used technique to infer vertical velocity is based

on QG dynamics in the form of the QG omega equation (e.g. Tintoré et al., 1991; Allen and Smeed, 1996; Gomis et al., 2001; Buongiorno Nardelli et al., 2001; Rodríguez et al., 2001; Pascual et al., 2004; Benítez-Barrios et al., 2011; Pidcock et al., 2013; Ruiz et al., 2014). Besides the application of this methodology to data from individual field campaigns, it has also been applied to different observation-based 3D products (Ruiz et al., 2009; Buongiorno Nardelli et al., 2012; Pascual et al., 2015). Another methodology used to derive vertical velocities is based on the integration of the SG omega equation, which includes the ageostrophic advection of geostrophic velocity (Hoskins and Draghici, 1977; Pedder and Thorpe, 1999; Badin, 2012; Buongiorno Nardelli, 2013). Both formulations of the omega equation allow the inference of the vertical velocity field from only density measurements. On the other hand, Viúdez et al. (1996) propose another version of the omega equation valid for high Rossby numbers that requires both density and current measurements. This generalized omega equation is more accurate than the other two versions (Viúdez and Dritschel, 2004) and allows the diagnosis of mesoscale vertical velocities in highly ageostrophic conditions. Other formulations of the generalized omega equation have also been proposed (e.g. Davies-Jones, 1991; Xu, 1992; Giordani et al., 2006).

Figure 2 shows some illustrative examples of different proposed/estimated vertical velocity distributions inside mesoscale eddies. In accordance with eddy-wind interaction theory, the vertical velocity induced within anticyclones and intrathermocline eddies is upwards, while within cyclones is downwards (Figure 2a) (Martin and Richards, 2001; McGillicuddy et al., 2007; Gaube et al., 2013, 2014). On the other hand, if both linear and nonlinear contributions are taken into account, the resulting total Ekman pumping is characterized by a dipolar distribution aligned across the wind direction (Figure 2b) (McGillicuddy et al., 2008; Gaube et al., 2015). A horizontal section of the vertical velocity field within an Aghulas cyclonic eddy inferred by integrating the SG omega equation is shown in Figure 2c. The vertical velocity distribution is characterized by a dipolar pattern within the eddy core and by an octopolar pattern along the eddy periphery. Buongiorno Nardelli (2013) suggests the relation of these patterns with modulation by vortex Rossby waves. Finally, Figure 2d shows the vertical velocity quadripolar distribution obtained theoretically within an elliptical anticyclonic eddy (or potential vorticity ball) by Viúdez and Dritschel

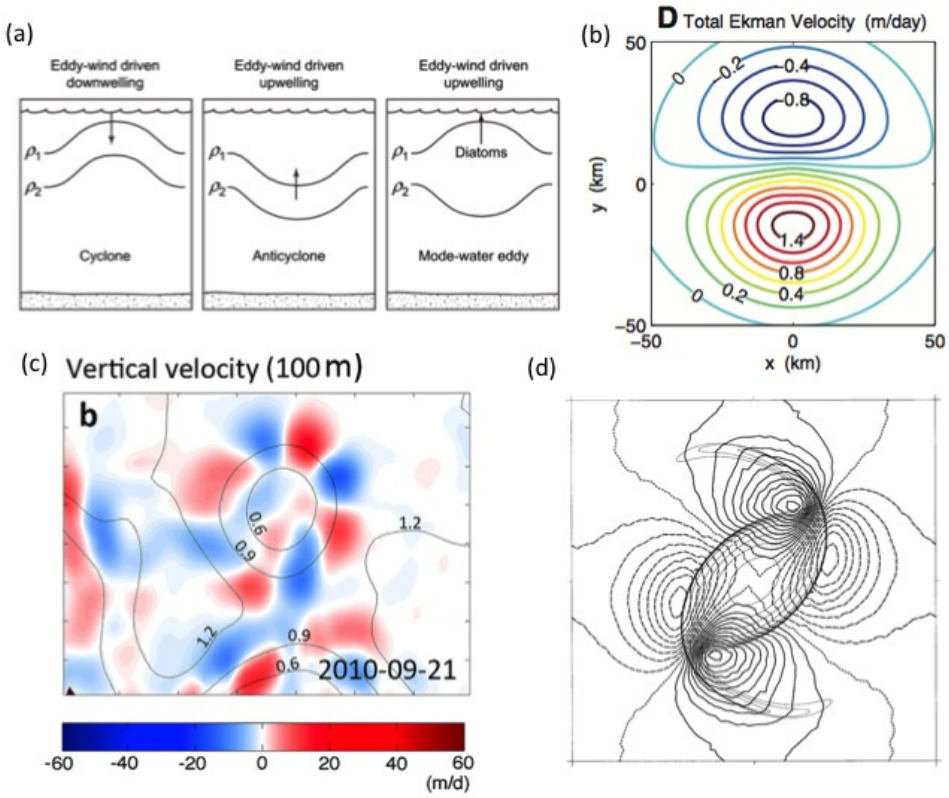

FIGURE 2: (a) Scheme of the vertical velocity induced by eddy-wind interaction associated with different types of mesoscale eddies. Arrows represent the sense of the vertical velocity: upward in anticyclones and intrathermocline (or mode water) eddies, and downward in cyclones. (McGillicuddy et al., 2007) (b) Total Ekman pumping within an intrathermocline eddy including both linear and nonlinear components. (McGillicuddy et al., 2008) (c) Horizontal section of the vertical velocity field at 100 m depth estimated by integrating the SG omega equation using observation-based data within a cyclonic eddy. (Buongiorno Nardelli, 2013) (d) Quadripolar horizontal distribution of vertical velocity (thick lines) within a non-forced and in an f-plane numerical elliptical anticyclonic potential vorticity ball. (Viúdez and Dritschel, 2003)

(2003).

Oceanic mesoscale eddies generated at the Canary Islands

The Canary archipelago is a zonal chain formed by seven islands situated off northwest Africa (Figure 3). All the islands except Fuerteventura and Lanzarote are mountainous with peaks exceeding 1000 m. The Canary Islands are located at the transition zone between the open ocean and the coastal upwelling off the northwest African coast, in the path of the Canary Current and the Trade winds (Barton et al., 1998; Barton and Arístegui, 2004; Pelegrí et al., 2005). The Canary Current is a

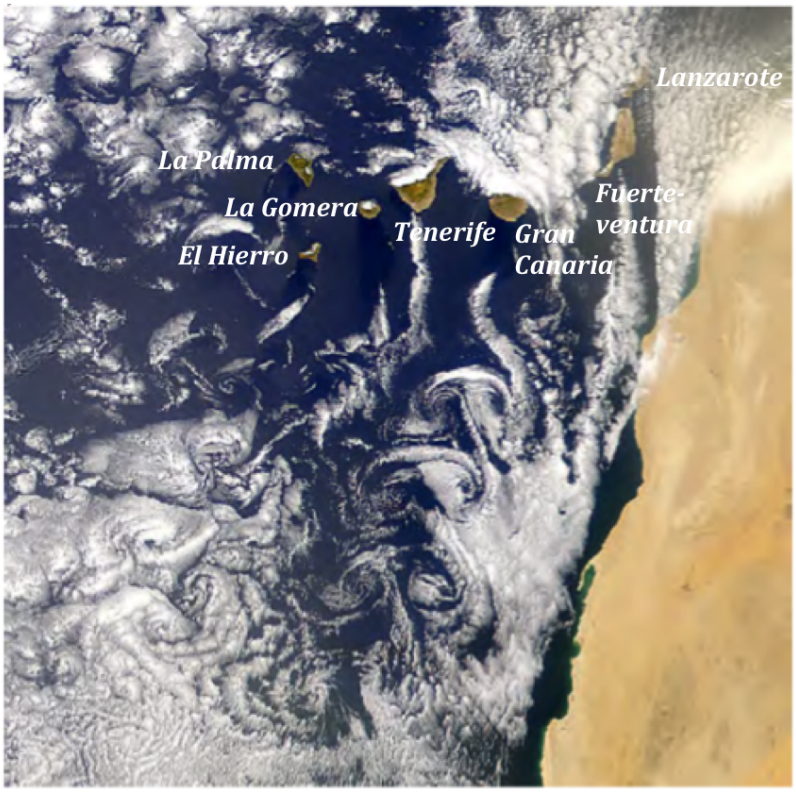

FIGURE 3: Canary Islands off northwest Africa. Atmospheric vortex street extending south from Gran Canaria observed from the MODIS sensor aboard the Terra satellite on 4 June 2000. The trail of atmospheric vortices is generated due to perturbation of Trade winds by the mountainous island. (Chopra, 1973; La Violette, 1974; Arístegui et al., 1994)

southward recirculation of the eastward Azores Current (Klein and Seidler, 1989; Mittelstaedt, 1991) whose strength, direction, and timing determine the complex mesoscale variability associated with the islands (Mason et al., 2011). The northeasterly alongshore Trade winds are originated by the steep pressure gradients between the high-pressure Azores system and the lower pressure over northwest African landmass. The Trades pass through the passages between islands resulting in the formation of intensified wind jets. The resulting curls induced by the wind jets are a source of oceanic eddies (Barton, 2001; Chavanne et al., 2002; Jiménez et al., 2008). Hence, the Canary archipelago acts as barrier to the prevailing Canary Current and Trade winds and is a continuous source of mesoscale eddy generation (Arístegui et al., 1994; Barton et al., 2000; Jiménez et al., 2008; Piedeleu et al., 2009; Sangrà et al., 2005, 2007, 2009).

Mesoscale eddies generated by the Canary Islands contribute to the Canary Eddy

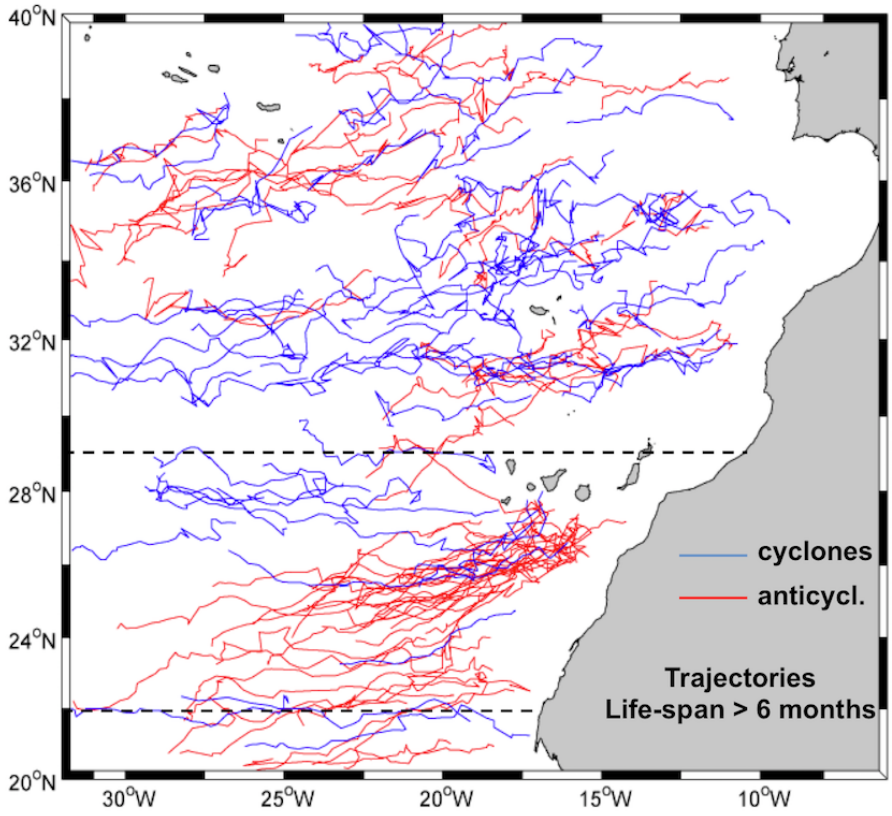

FIGURE 4: Canary Eddy Corridor extending from 22°N to 29°N with westward trajectories of the long-lived eddies tracked by the Okubo-Weiss technique using 14 years (1992-2006) of altimetry data. (Sangrà et al., 2009)

Corridor (CEC, Figure 4), a zonal mesoscale eddy corridor located between 22°N-29°N and from the Canaries to the west that constitutes the main pathway for long-lived ($>$ 3 months) eddies in the subtropical northeast Atlantic (Sangrà et al., 2009). It represents an important source of eddy kinetic energy in the northeastern Atlantic ocean. Moreover, the westward flux of mass associated with the CEC may be one-fourth of the southward mass transport of the Canary Current. It also has important implications on the offshore transport of biogeochemical properties from the Canaries/Northwest Africa upwelling systems.

Both types of eddies, cyclones and anticyclones, are generated by the Canary Islands: anticyclones are shed mainly from Tenerife and Gran Canaria, while cyclones are detached from La Palma, La Gomera, El Hierro, and Gran Canaria (Pacheco and Hernández-Guerra, 1999; Sangrà et al., 2005, 2009). One mechanism that induces island eddies is related to the perturbation of the oceanic flow by the island

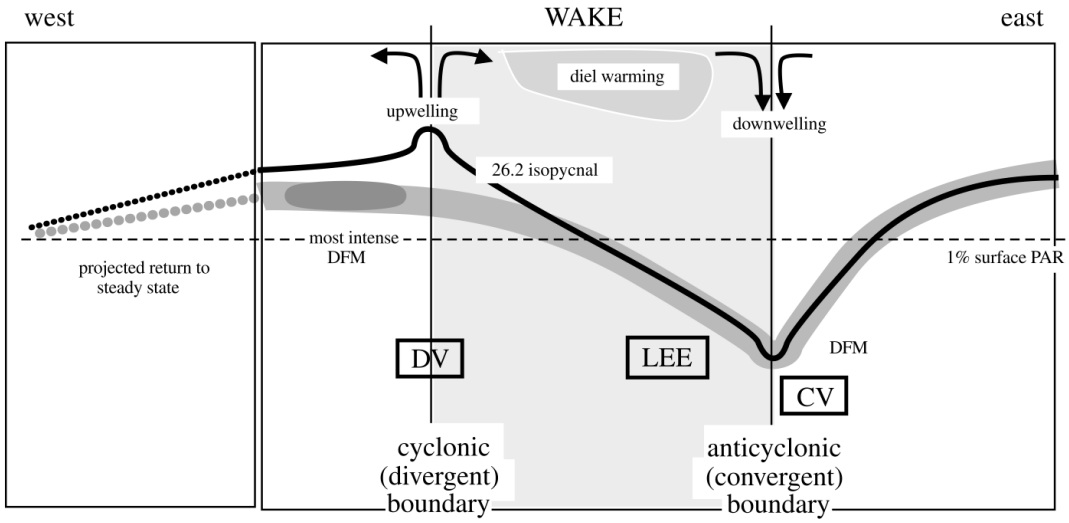

FIGURE 5: View from the south of the island wake of Gran Canaria showing the upwelling/downwelling generated by divergence/convergence of the Ekman transport induced by disturbance of Trade winds. The interaction of the mountainous island with the atmospheric flow induces wind shear fronts at both sides of the island. The wind shear fronts extend beyond the island with a sheltered area between them (the lee of the island wake). Ekman pumping generated beneath the shear zones induces opposite vertical displacements of the thermocline either side of the lee, being a mechanism for eddy production. On the lee boundaries, vertical velocities induced by an observed horizontal wind shear of 15 m s^{-1} in 2 km may be as strong as in the African coastal upwelling ($\sim$50 m d^{-1}). (Basterretxea et al., 2002)

topography (Sangrà et al., 2007; Jiménez et al., 2008; Piedeleu et al., 2009). If the impinging oceanic flow is sufficiently energetic, the boundary layer around the island detaches, alternating between flanks and giving rise to the sequential spin off of cyclonic and anticyclonic eddies. Another mechanism is related to Ekman transport convergence/divergence over the island wake and the corresponding Ekman pumping of downward/upward velocities related to strong anticyclonic/cyclonic wind curl cells (Figure 5). This mechanism is particularly important for low intensities of the Canary Current and strong intensities of the Trade winds (Barton et al., 2000; Basterretxea et al., 2002; Piedeleu et al., 2009; Caldeira et al., 2014).

The particular geographic and topographic characteristics of the Canary Islands, i.e., mountainous islands in the path of intense atmospheric and oceanic flows, and the presence of the Canary Eddy Corridor make the Canary region a natural laboratory for the study of mesoscale eddies. During the past decades several authors have investigated mesoscale oceanic eddies generated at the Canaries (e.g. Arístegui et al.,

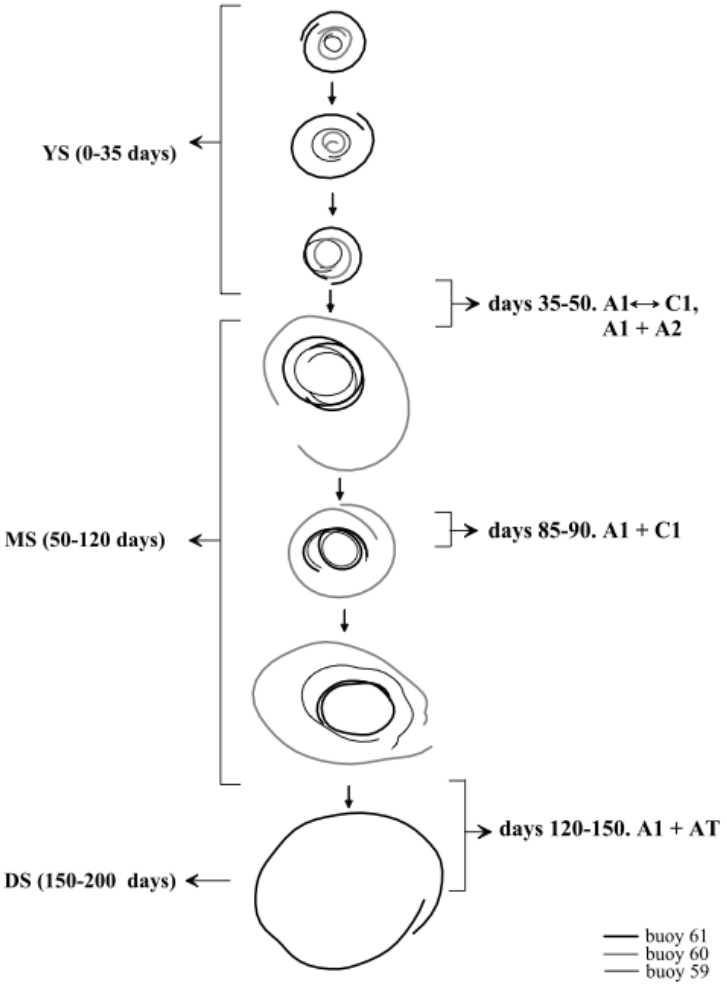

FIGURE 6: Scheme of the eddy life evolution derived from the trajectories of three buoys released within an anticyclonic eddy generated at Gran Canaria. The different stages are indicated: young (YS), mature (MS) and decay (DS) stages. (Sangrà et al., 2005)

1994; Sangrà et al., 2007). The first investigation revealing the presence of mesoscale oceanic structures in the Canary region was based on satellite and aircraft observations (La Violette, 1974). Afterwards, other studies have also taken advantage of remote sensing observations to analyze mesoscale eddies and the associated biological activity near La Palma, Tenerife, and Gran Canaria islands (e.g. Hernández-Guerra et al., 1993; Pacheco and Hernández-Guerra, 1999). Arístegui et al. (1994) performed the first hydrographic analysis of cyclonic and anticyclonic eddies associated with Gran Canaria from *in situ* observations (airborne expendable bathythermographs and Conductivity-Temperature-Depth (CTD)). After this characterization, several works have been focused on the analysis of the biological effects of mesoscale eddies

generated at the Gran Canaria island (e.g. Arístegui et al., 1997; Barton et al., 1998; Alonso-González et al., 2013; Lasternas et al., 2013). As previous field observations were carried out at the initial stages of the eddy life, other works have been focused on the dynamics, evolution, and regional implications of the eddies observed at the Canary region (Sangrà et al., 2005, 2007, 2009). Lastly, as previously mentioned, other authors have centered on the study of the eddy generation processes at the Canaries (Barton et al., 2000; Basterretxea et al., 2002; Jiménez et al., 2008; Piedeleu et al., 2009; Caldeira et al., 2014).

Canary eddies are commonly generated in spring and summer with a spin up time of 10 days (Piedeleu et al., 2009). These eddies have similar diameter to the island width and usually extends up to 300-700 m depth (e.g. Arístegui et al., 1994; Sangrà et al., 2007). The eddy life evolution (Figure 6) consists on an early stage in which the eddy core, that is in near solid body rotation following a Rankine profile, occupies all the eddy; a mature stage where the core is surrounded by a slowly revolving outer ring, and a decay stage in which the eddy dissipates (Sangrà et al., 2005, 2007). These eddies can maintain their coherent structures during several months (Sangrà et al., 2005, 2007). The analysis with buoys reveal that mature eddies may be characterized by elliptical shapes (Sangrà et al., 2005, 2007), however, both elliptical and circular eddies have been observed in the Canary region (Pacheco and Hernández-Guerra, 1999).

Objectives

The general objective of this dissertation is to shed some light on the thermohaline and dynamical structure, including ageostrophic secondary circulation, of mesoscale structures based on remote sensing observations and *in situ* data, paying special attention to mesoscale eddies and induced vertical motions. To achieve this we take advantage of an observation-based product, named ARMOR3D, which merges remote sensing observations (sea level anomaly and sea surface temperature) with the available *in situ* vertical profiles of temperature and salinity (mainly from ARGO) to provide a three-dimensional (3D) global ocean state estimate. Moreover, we analyze high-resolution data obtained from the interdisciplinary sampling of a subtropical intrathermocline eddy within the Canary Eddy Corridor in the northeastern Atlantic. Both datasets are used to solve different versions of the omega equation to diagnose the mesoscale vertical velocity and study its contribution on nutrient distribution, as well as to reveal for the first time with high-resolution *in situ* data the 3D structure of the secondary ageostrophic circulation within a mesoscale intrathermocline eddy.

The Canary Eddy Corridor has been demonstrated to be the main pathway for long-lived eddies in the subtropical northeast Atlantic (Sangrà et al., 2009). The high mesoscale activity characteristic of this region makes it suitable to locate and investigate mesoscale eddies. The interdisciplinary eddy sampling carried out in September 2014 had the main objective to study the oceanic vertical pump inside an anticyclonic eddy (Klein and Lapeyre, 2009). The anticyclonic intrathermocline eddy (named PUMP eddy) was identified using altimetry and intensively sampled using CTD, Acoustic Doppler Current Profiler (ADCP), microstructure turbulence profiler, water samples, and drifters. Here we aim to perform a detailed analysis of the hydrodynamic structure of the PUMP eddy. We provide the hydrographic background for the understanding of the dynamical processes that are at work within the PUMP eddy, namely, near-inertial wave trapping, ageostrophic secondary circulation (Barceló-Llull et al., 2017a), vertical mixing, and physical-biological interactions.

Although high-resolution *in situ* sampling of mesoscale structures is fundamental to describe in detail a particular hydrographic view and oceanic processes, it only covers a short period of time and reduced region of the global ocean. Because of this, other approaches are developed to analyze the temporal and spatial variability of mesoscale structures. Within these approaches we have used the ARMOR3D product, which provides global 3D datasets of temperature, salinity, and geostrophic velocities on a $1/4° \times 1/4°$ Mercator horizontal grid (the latest version; the older version used in Chapter 1 is $1/3° \times 1/3°$) with weekly temporal resolution. ARMOR3D product is validated here using the independent *in situ* data derived from the eddy sampling in order to prove the skills of the ARMOR3D product to detect mesoscale eddies and reproduce their hydrodynamic 3D structure.

Thesis outline

This thesis has been organized as a compilation of three published works and another in preparation. The structure of the thesis is as follows. In Part I we present a general introduction including the objectives and thematic unity of the research carried out within the framework of the thesis. The articles published are presented in Part II as self-contained chapters, together with the work currently in preparation. In Part III we summarize the main findings and results, as well as some comments on future work. Finally, in Part IV we present a summary written in Spanish as a requirement of the ULPGC regulation.

List of publications included in the thesis

- Chapter 1:

  Barceló-Llull, B., Mason, E., Capet, A., and Pascual, A. (2016). Impact of vertical and horizontal advection on nutrient distribution in the southeast Pacific. *Ocean Sci.* **12**, 1003-1011, doi: 10.5194/os-12-1003-2016

- Chapter 2:

  Barceló-Llull, B., Sangrà, P., Pallàs-Sanz, E., Barton, E. D., Estrada-Allis, S. N.,

Martínez-Marrero, A., Aguiar-González, B., Grisolía, D., Gordo, C., Rodríguez-Santana, A., Marrero-Díaz, A., and Arístegui, J. (2017). Anatomy of a subtropical intrathermocline eddy. *Deep-Sea Res. I*, doi: `http://dx.doi.org/10.1016/j.dsr.2017.03.012`, in press.

- Chapter 3:

  Barceló-Llull, B., Pallàs-Sanz, E., Sangrà, P., Martínez-Marrero, A., Estrada-Allis, S. N., and Arístegui, J. (2017). Ageostrophic secondary circulation in a subtropical intrathermocline eddy. *J. Phys. Oceanogr.* **47** (5), 1107-1123, doi: `10.1175/JPO-D-16-0235.1`

- Chapter 4:

  Barceló-Llull, B., Pascual, A., Mason, E., and Mulet, S. Validation of a multivariate global ocean state estimate with high-resolution *in situ* data. In prep.

Thematic unity of the thesis

The general topic of this thesis is the analysis of mesoscale dynamics using remote sensing observations and *in situ* data, paying special attention to mesoscale eddies and induced vertical motions. In the work *Impact of vertical and horizontal advection on nutrient distribution in the southeast Pacific* (Chapter 1) we aim to quantify the contribution of horizontal and vertical mesoscale motions on nutrient redistribution within mesoscale structures. In this chapter it is highlighted the importance of vertical motions associated with mesoscale dynamics (as meanders and eddies) on the injection of nutrients into the euphotic layer in the southeast Pacific, as an example of an oligotrophic region of the world ocean. We use the ARMOR3D dataset to infer the 3D vertical velocity field in this region through the integration of the QG omega equation, as only the density field is available and the Rossby number of mesoscale eddies in this regions is generally less than 0.1 (Chelton et al., 2011b). The Canary region constitutes a natural laboratory for the analysis of mesoscale eddies due to the presence of the Canary Eddy Corridor. Hence, it is a suitable region for the study of the hydrography and dynamics of these features, including the ageostrophic secondary circulation and its impact on marine ecosystems. With

this objective was carried out the PUMP eddy sampling. In Chapter 2, *Anatomy of a subtropical intrathermocline eddy*, we describe the sampling strategy conducted to intensively sample the PUMP eddy to obtain fine resolution two-dimensional (2D) data and coarser resolution 3D data. With these high-resolution data we analyze in detail the anatomy of the PUMP eddy. Then, the work *Ageostrophic secondary circulation in a subtropical intrathermocline eddy* presented in Chapter 3 uses the 3D density and horizontal velocity observed fields to infer the 3D vertical velocity field within the eddy through a generalized omega equation valid for the high Rossby regime, as the PUMP eddy is moderately ageostrophic. The horizontal ageostrophic velocity is inferred from momentum equations and, directly, by removing the geostrophic current to the horizontal ADCP velocity. This dissertation aims to understand the ageostrophic secondary circulation distribution and forcing mechanisms within the PUMP eddy. The currently in preparation work *Validation of a multivariate global ocean state estimate with high-resolution in situ data* presented in Chapter 4 closes this thesis with a comparison of the observation-based product used in Chapter 1 with the *in situ* data collected during the eddy sampling (Chapter 2). With this work we highlight the importance of validating the new products developed in operational oceanography with high-resolution *in situ* data to provide high-quality data management procedures. Ultimately we aim to evaluate the ability of the ARMOR3D product to detect mesoscale eddies and reproduce their hydrodynamic 3D structure.

Part II

Published works

Chapter 1

Impact of vertical and horizontal advection on nutrient distribution in the southeast Pacific

Barceló-Llull, B., Mason, E., Capet, A., and Pascual, A. (2016). Impact of vertical and horizontal advection on nutrient distribution in the southeast Pacific. *Ocean Sci.* **12**, 1003-1011, doi: 10.5194/os-12-1003-2016

Abstract

An innovative approach is used to analyse the impact of vertical velocities associated with quasi-geostrophic (QG) dynamics on the redistribution and uptake of nitrate in the southeast Pacific (SEP). Twelve years of vertical and horizontal currents are derived from an observation-based estimate of the ocean state. Horizontal velocities are obtained through application of thermal wind balance to weekly temperature and salinity fields. Vertical velocities are estimated by integration of the QG Omega equation. Seasonal variability of the synthetic vertical velocity and kinetic energy associated with the horizontal currents is coincident, with peaks in austral summer (November-December) in accord with published observations. The impact of vertical velocity on SEP nitrate uptake rates is assessed by using two Lagrangian particle tracking experiments that differ according to vertical forcing ($\omega = \omega_{QG}$ versus $\omega = 0$). From identical initial distributions of nitrate-tagged particles, the Lagrangian results show that vertical motions induce local increases in nitrate uptake reaching

up to 30%. Such increases occur in low uptake regions with high mesoscale activity. Despite being weaker than horizontal currents by a factor of up to 10^{-4}, vertical velocity associated with mesoscale activity is demonstrated to make an important contribution to nitrate uptake, hence productivity, in low uptake regions.

1.1 Introduction

Mesoscale dynamics make an important contribution to biogeochemical cycles through the redistribution of nutrients and passive marine organisms by both horizontal advection and vertical exchange. Vertical motion plays a key role in the exchange of heat, salt and biogeochemical tracers between the surface and deep ocean. In coastal upwellings, frontal areas and mesoscale eddies, the vertical velocity has fundamental importance and can significantly contribute to nutrient supply in the euphotic zone (Mahadevan, 2014).

Previous remote sensing studies (Chelton et al., 2011a) have revealed that chlorophyll-a distributions within mesoscale eddies are characterized by dipole-like patterns, with extreme values found at the eddy peripheries. Chelton et al. (2011a) proposed that eddy horizontal advection could explain these distributions. On the other hand, the importance of vertical exchange for phytoplankton growth and chlorophyll-a distributions in mesoscale oceanic eddies has been attributed to various mechanisms such as eddy pumping, eddy-induced Ekman pumping or vortex Rossby waves (McGillicuddy et al., 1998; Siegel et al., 1999; Mahadevan et al., 2012; Martin and Richards, 2001; McGillicuddy et al., 2007; Benítez-Barrios et al., 2011; Buongiorno Nardelli, 2013; Gaube et al., 2013, 2015).

In this context, we aim to estimate the importance of horizontal and vertical mesoscale motions on nutrient redistribution through the application of quasi-geostrophic (QG) theory to an observation-based product (Buongiorno Nardelli et al., 2012; Pascual et al., 2015). In particular, we aim to investigate the influence of derived horizontal and vertical velocities on ocean nitrate uptake in the southeast Pacific (SEP) through the use of a Lagrangian particle-tracking code.

The remote southeast Pacific is the least sampled oceanic region in the world ocean, in terms of both hydrography and biogeochemical structure (Ras et al., 2008).

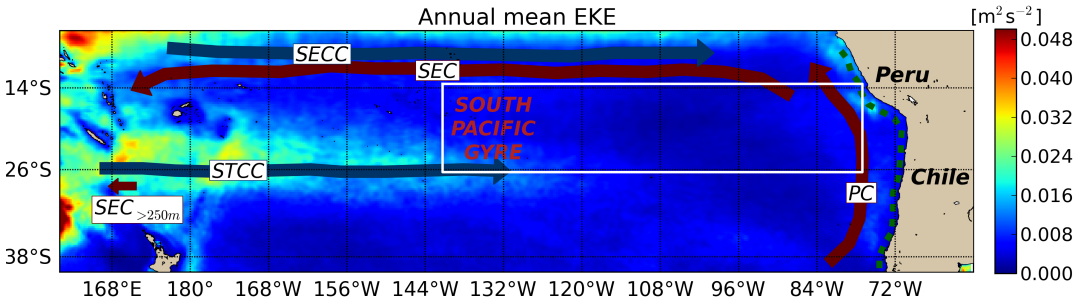

FIGURE 1.1: Map of the southeast Pacific. Colours show annual mean eddy kinetic energy (EKE) computed from daily AVISO (DT14, Capet et al. (2014a)) sea level anomaly data for the period 1993-2013. The white box shows the limits of the area of study. Key: SEC, South Equatorial Current; SECC, South Equatorial Countercurrent; STCC, Subtropical Countercurrent; PC, Peru Current. Green dashed line is the coastal upwelling. The small arrow indicates the poleward extent of the subsurface component of the SEC as observed by Qiu and Chen (2004) between 12-30°S at 170°E.

Synoptic observations from satellites provide crucial knowledge about such regions, despite their limitation to surface fields (Ducet et al., 2000; Dibarboure et al., 2011). The now mature Argo program is a source of supplementary subsurface hydrographic data (temperature and salinity) in the form of discrete vertical profiles over a global, but sparse, grid. The ARMOR3D estimate of the ocean state (Guinehut et al., 2012) is an innovative product where remote sensing observations (sea surface temperature and sea level anomalies) are merged with *in situ* Argo temperature and salinity profiles. The resulting multivariate observation-based dataset is freely available (see Section 1.3).

The southeast Pacific has a variety of different trophic regimes (Ras et al., 2008) such as the upwelling zone near the Peru-Chile coast that is rich in nutrients and has high chlorophyll-a concentrations, and the area associated with the central part of the South Pacific Gyre, which is the most oligotrophic area in the global ocean (Morel et al., 2010). Mesoscale effects on chlorophyll-a production can be considered to differ between regions with different dynamical characteristics. Lathuiliere et al. (2011) demonstrate that, while mesoscale activity in upwelling regions leads primarily to offshore export of phytoplankton, in the oligotrophic gyres mesoscale processes promote vertical advection of nutrients into the euphotic layer, thereby

stimulating primary production. The present work is focused on the same area analysed by Chelton et al. (2011a), the offshore southeast Pacific (white box in Fig. 1.1), where nutrient input by mesoscale vertical exchange is considered to play a lead role in primary production (Lathuiliere et al., 2011).

Fig. 1.1 shows the time averaged eddy kinetic energy (EKE) at the surface computed from daily AVISO (DT14, Capet et al. (2014a)) sea level anomalies. The EKE in the South Pacific Gyre has lower values in comparison with more active regions such as the Gulf Stream or Agulhas Current (Pascual et al., 2006; Imawaki et al., 2013). However, this gyre also includes a region with relatively high EKE values corresponding to the midwest South Pacific. Qiu and Chen (2004) and Qiu et al. (2008) attribute the high EKE values found in this region to baroclinic instability of the eastward-flowing surface Subtropical Countercurrent (STCC) and the westward-flowing South Equatorial Current (SEC). Although the SEC is a surface current near the equator, it has a subsurface component that Qiu and Chen (2004) observed to as far south as 30°S, where it underlies the STCC (see Fig. 3 of Qiu and Chen (2004)). Moreover, they also find that in this region seasonal EKE modulation is related to the seasonal intensification/decay of the STCC-SEC baroclinic instability, with a maximum in November-December. In the same way, the gyre has another region with relatively high EKE values at its northwest corner. In contrast to the STCC-SEC system, Qiu and Chen (2004) attribute these high values to barotropic instabilities between the eastward South Equatorial Countercurrent (SECC) and its bordering westward SEC. The SECC-SEC system also presents seasonal EKE modulation, but with maxima in April because the SECC-SEC horizontal shear seasonality is dominated by seasonal changes in the strength of the SECC. The two systems analysed by Qiu and Chen (2004) additionally show interannual EKE variability.

Figure 1.1 shows high EKE values off the Peru-Chile coast which is characterized by an important coastal upwelling and the consequent generation of mesoscale eddies and filaments (Brown et al., 2008; Brink and Robinson, 2005; Strub et al., 2013). The region of study (white box in Fig. 1.1) is characterized by relatively low EKE, with higher EKE values in the southwest corner that are related to the STCC-SEC system and, in the eastern section, to coastal upwelling eddy generation. However, the SEP has important eddy activity due, in part, to eddy formation in the Peru-Chile

coastal upwelling (Chelton et al., 2011a) .

A brief description of the synthetic temperature and salinity fields and biogeochemical data is given in Section 1.2. Section 1.3 describes the methodology used to diagnose the quasi-geostrophic vertical velocity, together with a description of the Lagrangian particle-tracking code utilised for the nitrate uptake simulation. In Section 1.4 the results of the vertical velocity and kinetic energy analysis as well as the results of the Lagrangian simulations are discussed. Section 1.5 summarizes and concludes the results.

1.2 Data

We use the ARMOR3D observation-based product which is based on the merging of gridded satellite sea level anomaly (SLA) and sea surface temperature (SST) remote sensing observations with *in situ* vertical profiles of temperature and salinity to provide a global 3D dataset of temperature and salinity (Guinehut et al., 2012). The data are computed on a $1/3^\circ$ Mercator horizontal grid with weekly temporal resolution covering the period 1998-2009, over 24 vertical levels from the surface to 1500 m depth. A validation of ARMOR3D is presented by Mulet et al. (2012) who use a consistent dataset from a model reanalysis.

Auxiliary data are used to evaluate the impact of vertical and horizontal velocities on SEP nitrate uptake rates. Here we use climatological nitrate data from WOAPISCES (Penven et al., 2008). Nitrate data are chosen because their large vertical gradient over the mixed layer (Figs. 1.2b and 1.2c) highlights the contribution of vertical velocity which is characterized by smaller values than horizontal currents, but is expected to play an important role in the introduction of nutrients into the euphotic layer. Figure 1.2a shows the horizontal nitrate distribution at 200 m depth from WOAPISCES. High nitrate values near the Peru-Chile coast are associated with the coastal upwelling. In the zonal section (Fig. 1.2b) the uplift of the nitracline due to the coastal upwelling off the Peru-Chile coast is evident. In the meridional section (Fig. 1.2c) nitrate concentrations increase northward.

Light conditions are used in Section 1.4.2 to assess the relevance of the Lagrangian nitrate transport estimates. Surface Photosynthetically Active Radiation

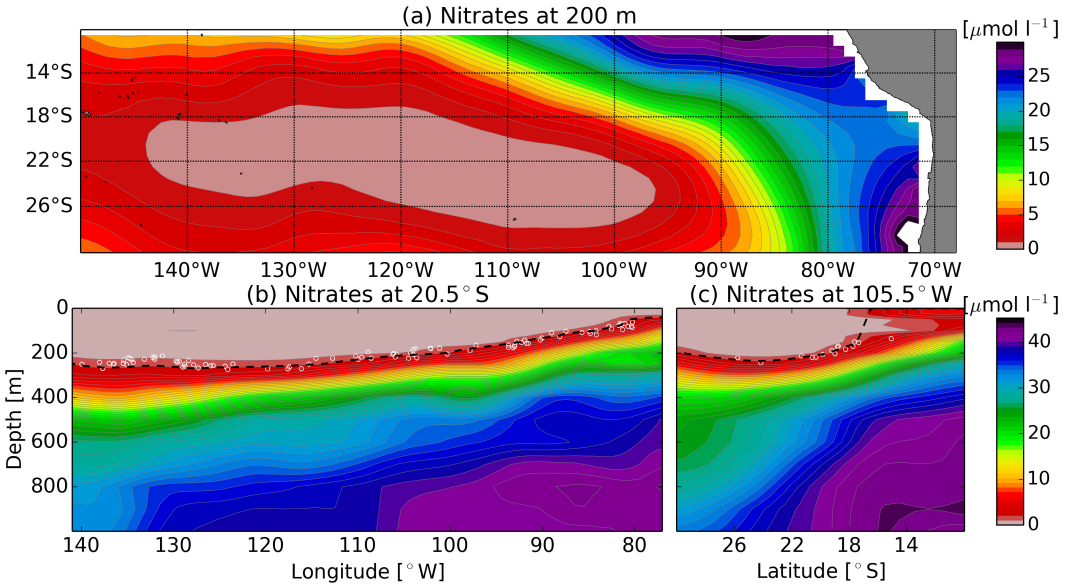

FIGURE 1.2: Climatological January nitrate from WOAPISCES in the southeast Pacific. (a) Horizontal section at 200 m depth, (b) vertical section at 20.5°S, and (c) vertical section at 105.5°W. Dashed black lines in (b) and (c) indicate the 2 μmol l^{-1} isoline. White dots are a random sample of the simulated water parcels at their initial positions.

(E_0) and attenuation coefficient at 490 nm (k) are obtained from the MERIS monthly climatology (`http://oceandata.sci.gsfc.nasa.gov/MERIS/Mapped/Monthly_Climatology/9km/par/`, `http://oceandata.sci.gsfc.nasa.gov/MERIS/Mapped/Monthly_Climatology/9km/Kd/`).

1.3 Methodology

1.3.1 Computation of 3D velocity

Horizontal geostrophic velocities are computed at all depths z_i through the thermal wind equations:

$$u_g(z_i) = u_g(0) - \frac{g}{\rho f}\int_{z_i}^{0} \frac{\partial \rho}{\partial y} dz \tag{1.1a}$$

$$v_g(z_i) = v_g(0) + \frac{g}{\rho f}\int_{z_i}^{0} \frac{\partial \rho}{\partial x} dz, \tag{1.1b}$$

with the density, ρ, calculated from ARMOR3D temperature and salinity profiles. f is the Coriolis parameter and g is gravity.

Vertical velocity is estimated using the quasi-geostrophic approximation by integrating the QG omega equation, presented here in its Q-vector formulation (Hoskins et al., 1978; Tintoré et al., 1991; Buongiorno Nardelli et al., 2012; Pascual et al., 2015):

$$N^2 \boldsymbol{\nabla}_h^2 w + f^2 \frac{\partial^2 w}{\partial z^2} = 2\boldsymbol{\nabla} \cdot \mathbf{Q}, \tag{1.2a}$$

where

$$\mathbf{Q} = \frac{g}{\rho_0} \left(\frac{\partial \mathbf{v}_g}{\partial x} \cdot \boldsymbol{\nabla} \rho', \frac{\partial \mathbf{v}_g}{\partial y} \cdot \boldsymbol{\nabla} \rho' \right), \tag{1.2b}$$

where $\mathbf{v}_g$ is the geostrophic velocity vector, ρ' is the departure from the mean density profile, N^2 the Brunt-Väisälä frequency and f the Coriolis parameter. In this implementation, N^2 only depends on depth. The Rossby number for mesoscale eddies in the SEP is generally less than 0.1 (Chelton et al., 2011b), hence we assume QG theory to be a good approximation for computing the vertical velocity in this region.

Following (1.2), vertical velocity is estimated from density stratification and the geostrophic velocity field. The computational code is derived following the QG vorticity and thermodynamic equations (Buongiorno Nardelli et al., 2012). Lateral boundaries are placed within the limits 68.4-141.3^{o}W and 13.4-26.4^{o}S. Boundary conditions are constructed by considering zero vertical velocity at the upper, lower and lateral boundaries.

A sensitivity analysis was carried out in order to evaluate the influence of reference level choice on the vertical velocity estimation. The choice of reference level is influential over the first hundred meters above the bottom due to the imposed boundary condition; away from the bottom the same patterns were seen for different choices of reference level (500 m and 1000 m). Testing the 500 m reference level, the vertical velocity patterns pointed to a maximum decrease in magnitude of 50%. Hence, a reference level of 1000 m depth was chosen. Dirichlet and Neumann conditions at the lateral boundaries were tested for which we found no significant impacts

on results a few points away from the boundaries.

1.3.2 Lagrangian simulations

In order to make an estimate of the potential biological impacts of the horizontal and vertical velocity components on the distribution of a limiting nutrient, in Section 1.4.2 a Lagrangian particle-tracking code is used to simulate water parcel trajectories forced by the derived ARMOR3D velocity fields. The tracking code is ROMS Offline (Roff, e.g. Capet et al., 2008; Carr et al., 2008; Mason et al., 2012). Two sets of year-long simulations were carried out for the year 2009: the first set was forced with geostrophic horizontal velocities and QG vertical velocity (UVW); for the second set the same geostrophic horizontal velocity was applied but vertical velocity was set to zero (UV). 1000 passive floats were released each week over a period of 364 days (initial date 31/12/2008) at random positions within a release area determined by the nitrate depletion depth (Fig. 1.2). This depth was estimated for each week following Omand and Mahadevan (2015), by selecting the depth at which nitrate content is 2 μmol l^{-1} from temporally and vertically interpolated climatological nitrate fields (WOAPISCES). Boundaries to the north, south and west are open; the eastern boundary is closed (see white box in Fig. 1.1). Float positions were stored every day as output of the Lagrangian simulation.

The initial nitrate concentrations for each float, $N(\mathbf{r}(t_0), t_0)$ with $\mathbf{r}(t) = (x(t), y(t), z(t))$, are interpolated in time and space from the monthly WOAPISCES climatology. In this way, the particles in each weekly release are initialized with local nutrient concentrations. The evolution of the nitrate content is then estimated along the Lagrangian tracks by considering an uptake term, U, and a remineralisation term, R:

$$\frac{\partial N}{\partial t} = -U + R \tag{1.3}$$

$$U = U_0 \cdot \frac{N}{N + K_N} \cdot \frac{E}{E + K_E} \tag{1.4}$$

$$R = max(0, \frac{N_C - N}{r}). \tag{1.5}$$

The maximum uptake rate, U_0 (μmol l^{-1} d^{-1}), is modulated by two Michaelis-Menten functions representing nitrate and light limitations, respectively (MacIsaac and Dugdale, 1972). The light conditions $E(\mathbf{r}(t),t) = E_0((x(t),y(t),0),t) \cdot e^{-k \cdot z(t)}$ are derived along each track by interpolation in time and space from the MERIS monthly climatology of surface Photosynthetically Active Radiation (E_0) and attenuation coefficient at 490 nm (k) (Marra et al., 2014). The values tested for the light half saturation parameter, K_E = 0.5, 1 and 5 μE m^{-2} s^{-1}, are taken in the range 1-10% of the typical surface PAR intensity (MacIsaac and Dugdale, 1972). The half saturation constant for nitrate limitation is taken as K_N = 0.2 μmol l^{-1} which is characteristic for oligotrophic marine regions (Eppley et al., 1969).

Remineralization is represented by a relaxation toward climatological nitrate values whenever the actual float N content falls below N_C, the climatological nitrate field (WOAPISCES). r is a characteristic relaxation time scale (days). We considered the values r= 5 and 10 days.

1.4 Results

1.4.1 QG vertical velocity and kinetic energy from observation-based product

A comparison between vertical velocity (w) and kinetic energy (KE) computed from the ARMOR3D derived geostrophic velocities is carried out in order to evaluate their relationship. An energetic region with high vertical velocities and mesoscale eddy activity is located in the southwest of the SEP, in both the vertical velocity (Fig. 1.3a) and kinetic energy (Fig. 1.3c) maps. This high eddy energy is related to baroclinic instabilities associated with the eastward surface Subtropical Countercurrent (STCC) and the westward underlying South Equatorial Current (SEC) system (Qiu and Chen, 2004; Qiu et al., 2008). Figure 1.3c shows other regions with elevated mesoscale activity that are associated with less intense vertical velocity values. These regions are the coastal upwelling and the SECC-SEC system explained in Section 1.1.

Vertical velocity in the energetic region in the southwest is highlighted in the zoom in Fig. 1.3b. Intense vertical motions of order 2-3 m d^{-1} with alternating signs

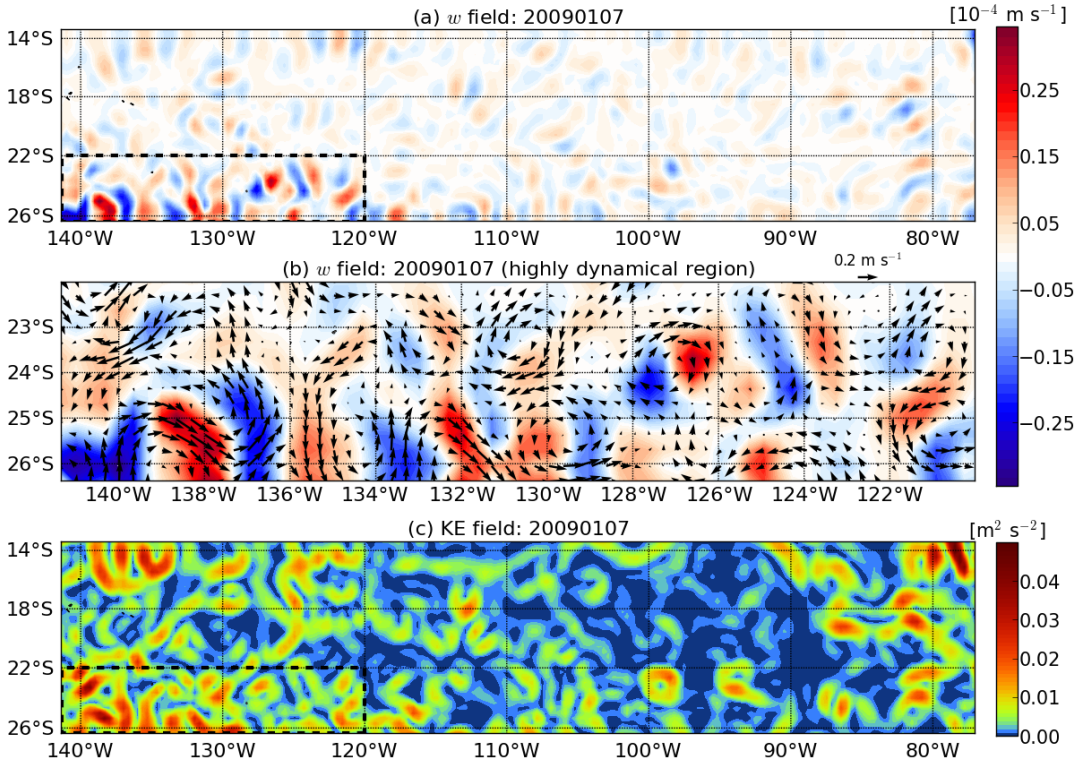

FIGURE 1.3: (a) Vertical velocity on 7 January 2009 at 200 m depth. Black box delimits the region of high mesoscale eddy activity. (b) Zoom of vertical velocity and horizontal geostrophic currents over the high mesoscale eddy activity region in (a). (c) Kinetic energy on 7 January 2009 at 200 m depth.

are located along meanders and inside eddies. The mesoscale eddies are characterized by dipole-like patterns with upwelling and downwelling cells at the eddy peripheries (e.g., 126-128°W and 23-25°S). Vertical velocity around anticyclonic meanders (e.g., 136-139°W and 24-26°S or 120-122°W and 24-26°S) shows the expected upwellings in the upstream and downwellings in the downstream portions of the meander crests (Woods, 1988; Bower, 1991; Pollard and Regier, 1992; Pascual et al., 2015). Similarly, downwellings and upwellings in cyclonic meanders (e.g., 137-140°W and 24.5-26°S) are located upstream and downstream of the crest, respectively.

In order to analyse the variability of w, the standard deviation over the period 7 January 1998 to 30 December 2009 is computed and shown in Fig. 1.4a; Fig. 1.4b shows the standard deviation of the KE. The active region in the southwest of the SEP presents high temporal variability in both fields. The correlation coefficient between both fields in this region reaches 0.85. Considering the whole area of study,

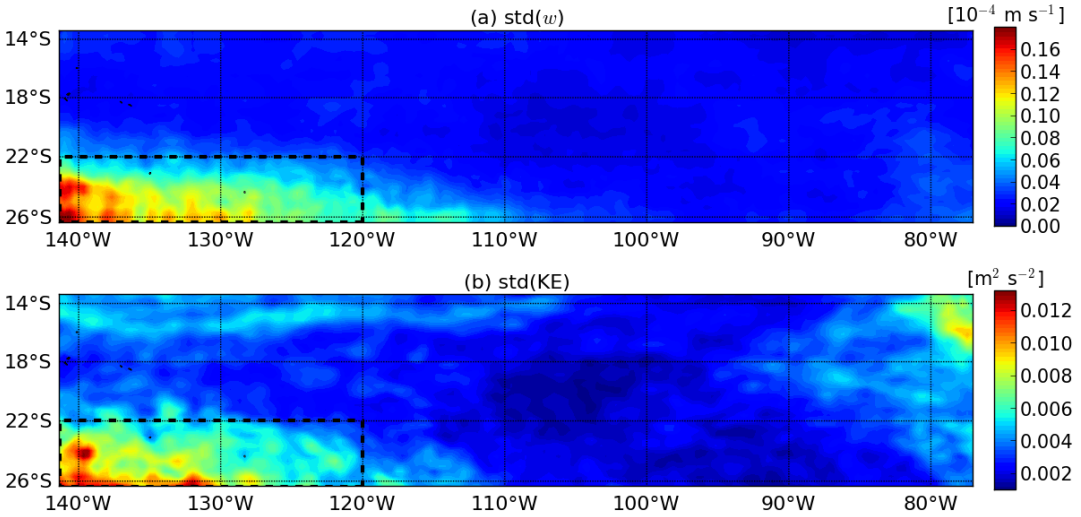

FIGURE 1.4: (a) Standard deviation of vertical velocity and (b) kinetic energy over the period 7 January 1998 to 30 December 2009 at 200 m depth. The discontinuous line delimits the region of high mesoscale variability.

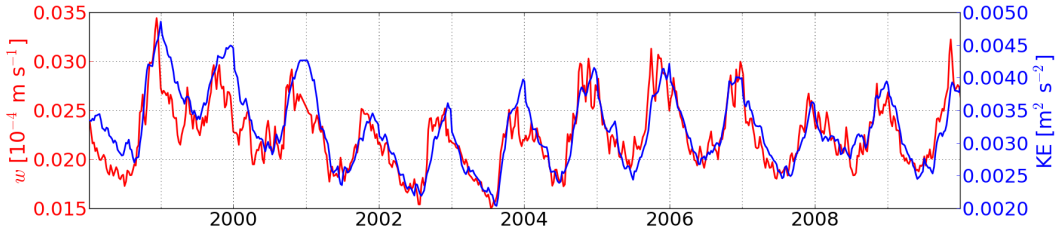

FIGURE 1.5: Time series of vertical velocity magnitude (red line) and kinetic energy (blue line) averaged over the area of study. The correlation coefficient between vertical velocity and kinetic energy is 0.84.

the correlation coefficient is 0.79. It should be noted that this high correlation between the two variables could not be anticipated *a priori* as the relationship is not linear (see equations 1.2).

Time series of spatial averages of vertical velocity magnitude and kinetic energy are shown in Fig. 1.5. There is clear seasonal variability in both variables, with maximums in austral summer and minimums in austral winter related to the seasonal intensification/decay of the STCC-SEC vertical shear and, in consequence, with the increase/decrease of baroclinic instability (Qiu et al., 2008). Interannual variability and weak variability of high frequency are also shown in these figures. When averaging over only the highly energetic region in the southwest (not shown) the tendency is similar but the magnitude is double.

1.4.2 Lagrangian simulations

In order to evaluate the potential biological impacts of the vertical velocities, we analysed the nitrate uptake rates along the Lagrangian tracks resulting from successive weekly particle releases within the nitrate depletion depth (see Section 1.3.2). To compare nitrate uptake rates in the simulations with (UVW) and without (UV) vertical motions, we computed the median of the nitrate uptake terms in bins of $0.5^\circ \times 0.5^\circ$ over the full annual simulations. The deeper particle tracks, for which uptake terms were lower than 0.001 (μmol l^{-1} d^{-1}), were disregarded in these computations. As expected, nitrate uptake rates (Fig. 1.6) are higher in the northeastern upwelling region. Intermediate uptake values can also be seen in the region of high mesoscale activity (ca. 120-140°W and 22-26°S). While the restricted resolved vertical velocities leave the overall pattern of nitrate uptake unchanged, local nitrate uptake increases reach up to 30% in the region characterized by low uptake rates and high mesoscale activity (Fig. 1.6c).

The simplified nutrient model considered here is not suitable for a detailed study of the dynamics of nitrate, in particular as it does not consider planktonic biomass and diversity. However, we tested the sensitivity of the results to the U_0, r and K_E parameters. In Fig. 1.7 we show that spatially-averaged increases in uptake rates over the region of high mesoscale activity vary between 0.4 and 11.6%, with an average of 6.5% for the considered range of parameter values. Larger increases are observed in the cases with high maximum uptake rates and strong light limitation.

1.5 Discussion and Conclusions

This paper analyses vertical velocities associated with QG dynamics as derived through an innovative approach that uses the ARMOR3D global observation-based product. Weekly horizontal geostrophic velocity and QG vertical velocity are computed from ARMOR3D temperature and salinity in the southeast Pacific. We analyse the QG vertical velocity in order to understand its distribution. The southwest of the SEP has relatively high mesoscale activity with vertical velocities exceeding 2 m d^{-1}, which is on the order of 10^{-4} times the horizontal velocity. Vertical velocity and kinetic energy in the SEP have similar and intense seasonal variability with maximums

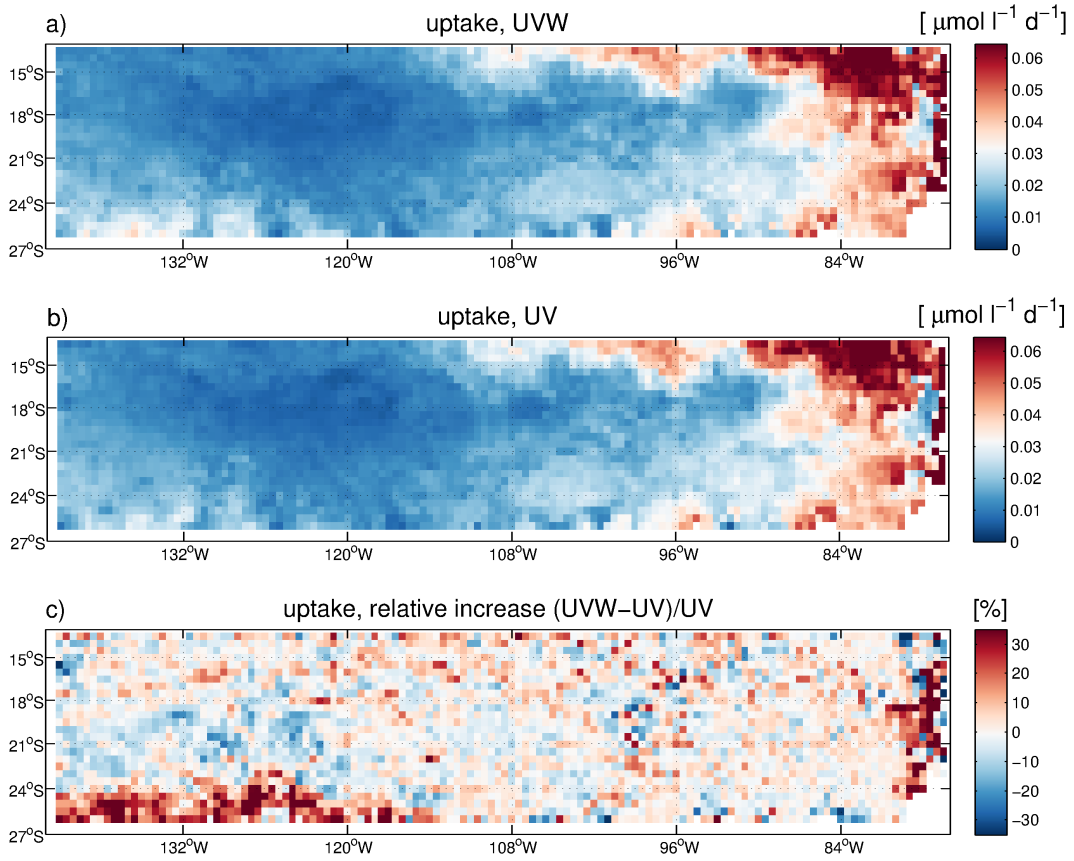

FIGURE 1.6: Nitrate uptake rates considering (a) both QG vertical velocity and geostrophic horizontal velocity (UVW); (b) only geostrophic horizontal velocity (UV); (c) Relative increase of nitrate uptake rates when including vertical velocity. These fields were obtained for r = 10 d, U_0 = 0.1 μmol l^{-1} d^{-1}, K_E = 1 μE m^{-2} s^{-1} and K_N = 0.2 μmol l^{-1}.

in austral summer (November-December), which suggests that these quantities are mostly influenced by the seasonal modulation of STCC-SEC vertical shear (Qiu and Chen, 2004; Qiu et al., 2008).

Despite their relatively small magnitudes, vertical motions may have an important impact on the introduction of nutrients into the euphotic layer in areas with pre-existing vertical gradients of nutrients and, hence, can be considered influential on marine ecosystem variability. Two year-long Lagrangian simulations are forced with 3D velocity fields. The first is forced by 3D geostrophic velocities and QG vertical velocity in order to evaluate their combined contribution to rates of nitrate uptake along the tracks. The second is forced with the same 3D geostrophic velocities and zero vertical velocity in order to evaluate the horizontal velocity contribution to the nitrate uptake. The Lagrangian experiments enable an examination of nitrate uptake

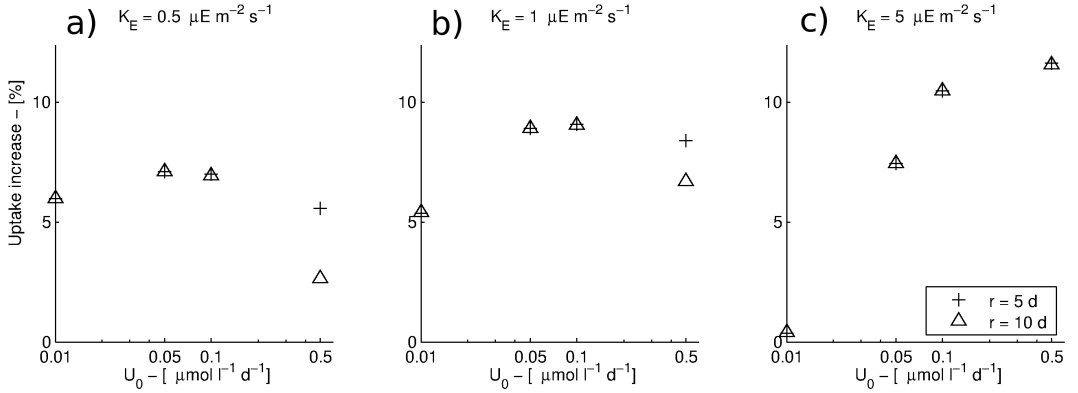

FIGURE 1.7: Average increase of nitrate uptake rates in the region of high mesoscale eddy activity (ca. 120-140°W and 22-26°S) for different values of the uptake coefficient U_0, and relaxation time scale r.

rates under varying light conditions within the euphotic layer. This analysis reveals that, in regions with low rates of nitrate uptake, vertical motions associated with high mesoscale activity may be responsible for local increases in these uptake rates of up to 30%. We caution that the nitrate model used is simple and that the outcomes are sensitive to the chosen values of maximum nitrogen uptake rate (U_0) and light half-saturation parameter (K_E). Nevertheless, these results are indicative of the importance that mesoscale vertical motions have on sustaining primary productivity in the oligotrophic regions of ocean interiors.

Although we only analyse the (large) mesoscale vertical velocity, the importance of submesoscale features on vertical tracer dispersion has been shown by Klein and Lapeyre (2009). Accordingly, the vertical velocity contribution estimated here can be considered an underestimation of the real vertical velocity contribution. Fine resolution satellite observations can help to better evaluate the impact of vertical motions on nutrient redistribution. The wide-swath SWOT altimeter will allow unique observations in the 15-100 km range of wavelength scales when it comes online in the next decade (Fu and Ferrari, 2008).

Chapter 2

Anatomy of a subtropical intrathermocline eddy

Barceló-Llull, B., Sangrà, P., Pallàs-Sanz, E., Barton, E. D., Estrada-Allis, S. N., Martínez-Marrero, A., Aguiar-González, B., Grisolía, D., Gordo, C., Rodríguez-Santana, A., Marrero-Díaz, A., and Arístegui, J. (2017). Anatomy of a subtropical intrathermocline eddy. *Deep-Sea Res. I*, doi: http://dx.doi.org/10.1016/j.dsr.2017.03.012, in press.

Abstract

An interdisciplinary survey of a subtropical intrathermocline eddy was conducted within the Canary Eddy Corridor in September 2014. The anatomy of the eddy is investigated using near submesoscale fine resolution two-dimensional data and coarser resolution three-dimensional data. The eddy was four months old, with a vertical extension of 500 m and 46 km radius. It may be viewed as a propagating negative anomaly of potential vorticity (PV), 95% below ambient PV. We observed two cores of low PV, one in the upper layers centered at 85 m, and another broader anomaly located between 175 m and the maximum sampled depth in the three-dimensional dataset (325 m). The upper core was where the maximum absolute values of normalized relative vorticity (or Rossby number), $|\mathrm{Ro}| = 0.6$, and azimuthal velocity, $\mathrm{U} = 0.5\ \mathrm{m\ s^{-1}}$, were reached and was defined as the eddy dynamical core. The typical biconvex isopleth shape for intrathermocline eddies induces a decrease of static stability, which causes the low PV of the upper core. The deeper

low PV core was related to the occurrence of a pycnostad layer of subtropical mode water that was embedded within the eddy. The eddy core, of 30 km radius, was in near solid body rotation with period of $\sim$4 days. It was encircled by a thin outer ring that was rotating more slowly. The kinetic energy (KE) content exceeded that of available potential energy (APE), KE/APE = 1.58; this was associated with a low aspect ratio and a relatively intense rate of spin as indicated by the relatively high value of Ro. Inferred available heat and salt content anomalies were AHA = 2.9 $\times$ 10^{18} J and ASA = 14.3 $\times$ 10^{10} kg, respectively. The eddy AHA and ASA contents per unit volume largely exceed those corresponding to Pacific Ocean intrathermocline eddies. This suggests that intrathermocline eddies may play a significant role in the zonal conduit of heat and salt along the Canary Eddy Corridor.

2.1 Introduction

Intrathermocline eddies are a particular type of subsurface intensified anticyclonic eddy (Dugan et al., 1982; McWilliams, 1985; Kloosterziel and van Heijst, 1991). Their imprint in hydrographic fields is characterized by dome-shaped isopleths in the upper layers and a bowl-shape in the lower layers, sometimes with a homogeneous pycnostad layer embedded within. As a consequence of the decrease of static stability at the eddy core, a large negative anomaly of potential vorticity develops (Gordon et al., 2002; Pidcock et al., 2013). Intrathermocline eddies are relatively frequent and, in some regions such as in the eastern boundary upwelling systems (EBUS), they may represent 30-55% of the anticyclonic eddy population (Pegliasco et al., 2015).

There is a great variety of intrathermocline eddies with different origins. Those generated by the poleward undercurrents in the EBUS (Hormazabal et al., 2013; Pelland et al., 2013; Pegliasco et al., 2015) have a typical radius between 20 km (California EBUS) and 60 km (Peru-Chile EBUS) and a vertical extent of ca. 500 m. They generally do not contain a homogeneous core (or pycnostad layer) but they are characterized by a minimum in oxygen (Hormazabal et al., 2013; Stramma et al., 2013). A particular type of these eddies are swoddies, or Slope Water Oceanic eddies, generated by destabilization of the highly baroclinic poleward slope current

off the Iberian Peninsula, also known as Iberian Poleward Current, in winter (Pingree and Le Cann, 1992b,a; Garcia-Soto et al., 2002; Sánchez and Gil, 2004; Carton et al., 2013). In summer, the seasonal thermocline is restored capping the feature (Sánchez and Gil, 2004). They usually have radius of 40-60 km, contain a homogeneous core of slope water ($\sim$20-30 km radius and $\sim$200 m thickness) with maximum azimuthal velocities at 100 m depth, and drift mostly westwards at 2 cm s^{-1}. On the other hand, Mediterranean water eddies, or meddies, generated from instabilities of the Mediterranean Undercurrent, have also been observed in the Iberian and Canary Basins (Hebert et al., 1990; Schultz Tokos and Rossby, 1991; Shapiro et al., 1995; Carton et al., 2010; L'Hégaret et al., 2014; Bashmachnikov et al., 2015). They are salty and warm deep lenses usually centered at 1000 m depth that may drift, mainly southwestwards, during 1-3 years. They usually have 20-75 km radius, 500-1000 m thickness and maximum azimuthal velocities of 0.2-0.5 m s^{-1}. In the Subarctic region large intrathermocline eddies of 60 km radius and ca. 1300 m vertical extent have been observed that have deep cores (600 m) of homogeneous water (Martin and Richards, 2001; Pidcock et al., 2013). In contrast, those described for the Japan Sea or for the Southern Indian Ocean regions are shallow flat homogeneous water lenses with 50 km radius, vertical extents of only 100 m to 150 m, and oxygen-rich cores (Gordon et al., 2002; Hogan and Hurlburt, 2006; Nauw et al., 2006). In the subtropical northeast Atlantic Ocean, Pingree (1996) gave the first description of an intrathermocline eddy inside the Canary Eddy Corridor (Sangrà et al., 2009). The eddy had a radius of 60 km and a vertical extent of 600 m. It was 18 months old at the time of the eddy sampling and was located ca. 1800 km west of the Canary Islands. Recently, Caldeira et al. (2014) sampled an intrathermocline eddy generated in the lee of Madeira Island as an ocean response to wind-forcing. The sampled eddy had a radius of 26 km and it was surveyed at the generation region.

Amongst the population of intrathermocline eddies there is a particular type whose core is composed of homogeneous oxygen-rich mode water (Oka, 2009; Caldeira et al., 2014). Mode water is the name given to a layer of nearly vertically homogeneous water found over a relatively large geographical area, and which is identifiable through the contrast in stratification with the pycnocline waters (Hanawa and Talley, 2001). Mode waters have their origins in the deep mixed layers formed

by winter convection. It has been observed recently that intrathermocline eddies originated in western boundary systems play a crucial role in mode water transport and subduction into the main thermocline (Xu et al., 2016).

Apart from those eddies that are locally generated by poleward undercurrents (e.g. Pelland et al., 2013; Pegliasco et al., 2015), or in the Subarctic region (e.g. Pidcock et al., 2013), the origin of intrathermocline eddies is still under discussion. Thomas (2008) proposed that a source for intrathermocline eddies is the reduction of potential vorticity in frontal regions with winds blowing in the direction of the frontal jet. As indicated above, intrathermocline eddy cores contain negative anomalies of potential vorticity. Wind-front interactions subduct low potential vorticity waters that are the source for intrathermocline eddies. Hogan and Hurlburt (2006) investigated numerically the origin of intrathermocline eddies in the Japan Sea. They conclude that there are three different mechanisms that affect the formation of intrathermocline eddies: 1) advection of stratified water that caps a pre-existing anticyclone; 2) restratification of the upper layers in a pre-existing anticyclone due to solar heating and; 3) frontal convergence and subduction of winter surface mixed layer water. This latter mechanism has also been proposed for Southern Indian Ocean intrathermocline eddies (Nauw et al., 2006). Recently McGillicuddy (2015) proposed eddy-wind interaction (Martin and Richards, 2001; McGillicuddy et al., 2007) as a new generation mechanism of intrathermocline eddies, which would drive an upwelling strong enough to induce the doming of the near surface isopycnals of an anticyclonic eddy.

A distinctive feature of the Canary EBUS is the presence of the Canary Island archipelago that acts as barrier to the prevailing currents and winds and is thus a continuous source for mesoscale eddy generation (Arístegui et al., 1994; Barton et al., 2000; Jiménez et al., 2008; Piedeleu et al., 2009; Sangrà et al., 2009, 2007, 2005). These eddies contribute to the Canary Eddy Corridor which is the main pathway for long-lived eddies in the subtropical northeast Atlantic, making it a suitable region for the observation of mesoscale eddies (Sangrà et al., 2009). Long-lived anticyclonic eddies are much more frequent than cyclones. With the aim to study the oceanic vertical pump (Klein and Lapeyre, 2009) inside an anticyclonic eddy, we conducted an

interdisciplinary survey of an intrathermocline eddy inside the Canary Eddy Corridor in September 2014. As detailed in Section 2.2, we intensively sampled the eddy obtaining fine resolution two-dimensional (2D) data and coarser resolution three-dimensional (3D) data. To the best of our knowledge, such intensive sampling has not been performed in previous studies of intrathermocline eddies. In this study we describe in detail the anatomy of an intrathermocline eddy. This paper provides the hydrographic background to a series of other studies based on the survey data set, such as those dealing with inference of ageostrophic secondary circulation (Barceló-Llull et al., 2017a) or with the impacts of the eddy on biogeochemical fluxes and plankton community structure and activity (in preparation).

2.2 The PUMP survey

For the five months before the eddy survey, conducted aboard the R/V Hespérides, we monitored on a daily basis the signature of anticyclonic eddies generated by the Canary Islands in the sea level anomaly (SLA) field. Daily SLA maps (Capet et al., 2014b) were obtained from gridded data provided by AVISO (`http://www.aviso.altimetry.fr`). In May 2014 an anticyclone was shed by the island of Tenerife. The eddy was tracked until September 2014, when it was 550 km to the southwest (Fig. 2.1). As we knew its origin and its signature in the SLA field was robust, we selected this 4 months old eddy to be the target for our study. We named the eddy "PUMP" as it was surveyed in the framework of the PUMP (Study of the Vertical Oceanic Pump in mesoscale eddies) project.

The eddy survey was organized into 3 phases (Fig. 2.1). Guided by the eddy signal in the SLA field, we first crossed the eddy with two transects (Fig. 2.1, green and cyan lines) sampled with continuous tows of a conductivity-temperature-depth (CTD) probe on an undulating vehicle (SeaSoar) during the days 3-5 September 2014. The objective was to locate the eddy center and to make a first estimate of its radius and depth. Next, in order to obtain 3D fields of hydrographic and dynamical variables, we sampled a grid centered on the eddy center. The grid consisted of 6 SeaSoar (Fig. 2.1, black lines) and 3 rosette (the SeaSoar CTD was attached to a rosette system after failure of the SeaSoar; Fig. 2.1, black dots) zonal transects of length

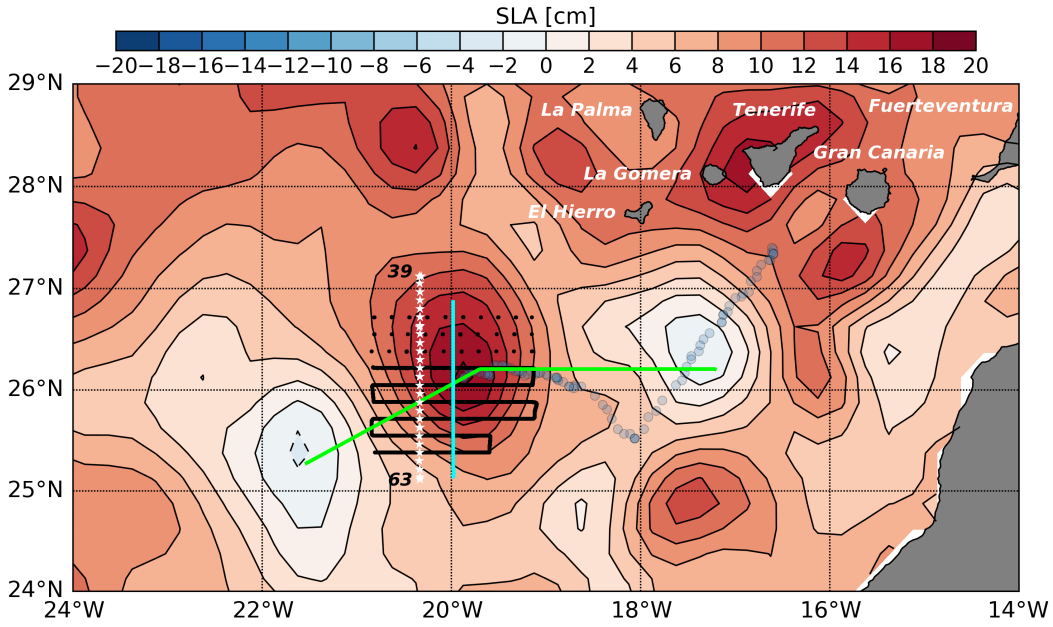

FIGURE 2.1: Map of the Canary Eddy Corridor. Colors show sea level anomaly (SLA) from AVISO on 3 September 2014. Green and cyan lines represent Phase 1 of the PUMP cruise, taken to locate the eddy center. Black lines and dots mark the grid of the 3D eddy sample with SeaSoar continuous tows and rosette system discrete casts, respectively (Phase 2). White stars indicate high-resolution CTD stations in Le Tourmalet section (Phase 3). The trajectory of the eddy center from its formation to the beginning of the cruise is depicted by blue dots (the time interval between dots is 1 day). The eddy translated westwards with a speed of 4 km d^{-1} (0.046 m s^{-1}) during the eddy sampling.

166.68 km. Transects were 18.52 km apart, as were the rosette stations. The resulting 3D grid, combining rosette casts at discrete stations with SeaSoar tows, had a size of 166.68×166.68 km with 18.52×18.52 km resolution. In most profiles, the SeaSoar measurements extend from 10 m down to 325 m. Rosette casts were made to a nominal depth of 400 m. The 3D survey was accomplished in five days (6-11 September 2014). In the third and final phase, we crossed the eddy center meridionally with a 222.24 km transect (that we named Le Tourmalet) consisted of 24 CTD stations spaced approximately 9.26 km apart (Fig. 2.1, white stars). In addition, microstructure measurements and water samples for biogeochemical studies were taken along this transect. CTD casts were made to a nominal depth of 1000 m and the transect was sampled over 3 days (12-15 September).

The undulating vehicle we used was a SeaSoar Mk II with an onboard CTD SB911+ additionally equipped with a Seapoint Chlorophyll Fluorometer, dual SBE43

oxygen sensors, and a Seapoint Turbidity Meter. On average, the profiles were separated by 4 km with an effective vertical resolution of 72 cm. Rosette casts were also made using the CTD SB911+ instrument additionally equipped with a Seapoint Chlorophyll Fluorometer, dual SBE43 oxygen sensors, Wetlabs C-Star Transmissometer (25 cm 660 nm), Seapoint Turbidity Meter, and Biospherical Remote Photoradiometer sensors attached to the rosette system of 24 oceanographic 12 l Niskin bottles. Raw data files were processed with Sea-Bird SEASOFT software (`http://www.seabird.com/software/softrev.htm`) and vertically averaged into 1 m bins. We use the TEOS-10 algorithms to calculate absolute salinity, S_A, and conservative temperature, Θ, and all derived variables (Feistel, 2003, 2008).

Current velocities were measured continuously in all three phases using a hull-mounted 75 kHz RDI acoustic Doppler current profiler (ADCP). The ADCP provided raw data with 5-min ensembles from the surface to ~800 m and a bin size of 8 m. The raw data were quality controlled, corrected for heading misalignment and edited with the Common Oceanographic Data Access (CODAS, Firing et al., 1995). On average, the processed profiles provide good quality data from 30 to 700 m depth.

2.3 PUMP eddy signature

The purpose of the SeaSoar transects on Phase 1 (Fig. 2.1, green and cyan lines) was to sample the *in situ* signal of the SLA tracked eddy seen in Fig. 2.1, in the context of its immediate environment. Figure 2.2 shows a vertical section of the potential density anomaly, σ_Θ, along the east-west transect sampled on Phase 1 (Fig. 2.1, green line) superposed on the cross-transect velocity as obtained from the ship-mounted ADCP. At 280 km distance the upper seasonal pycnocline is dome-shaped, whereas the permanent pycnocline located below is bowl-shaped leading to a biconvex shape of the isopycnals. Furthermore, between the depths of the 26.5 kg m^{-3} and 26.6 kg m^{-3} isopycnals a layer of almost uniform potential density anomaly typical of Madeira Mode Water is evident (Käse et al., 1985; Siedler et al., 1987; Weller et al., 2004). The eddy shows a deep intensified anticyclonic circulation with maximum

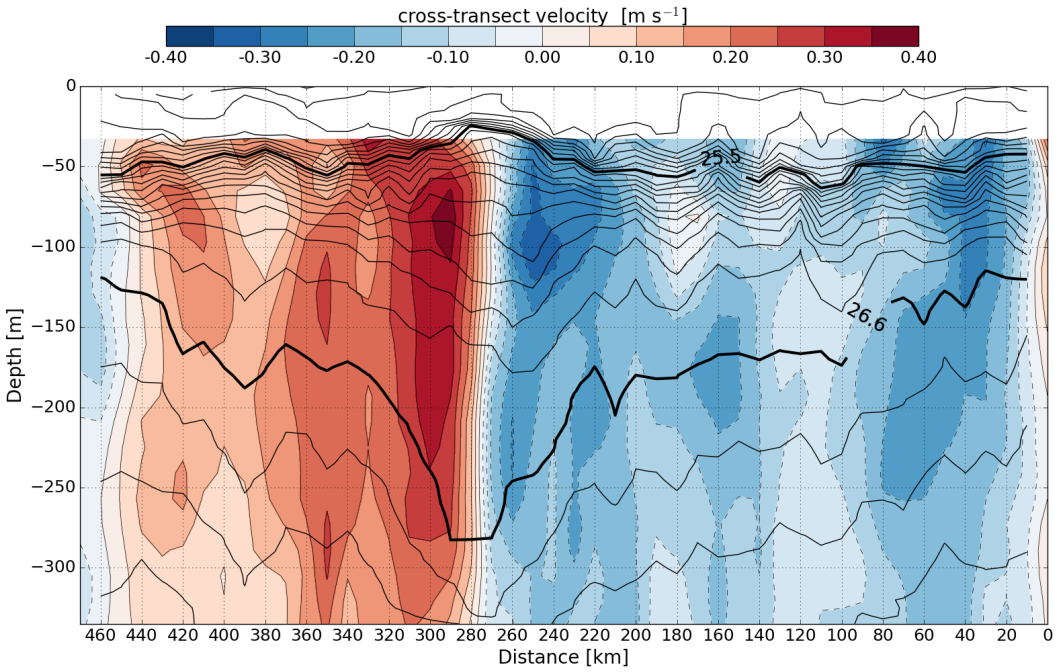

FIGURE 2.2: Vertical section along the east-west transect in Phase 1 (3-5 September 2014; Fig. 2.1, green line) of the cross-transect ADCP velocity with superimposed contours of potential density anomaly, σ_Θ. Thick contours are σ_Θ = 25.5 kg m^{-3} and σ_Θ = 26.6 kg m^{-3} (contour interval is 0.1 kg m^{-3}).

(minimum) velocity values of 0.38 (-0.35) m s^{-1} at 81 (97) m. This subsurface intensified anticyclonic flow implies a vertical shear that is consistent with the biconvex isopycnal shape through thermal wind balance. Above (below) this subsurface speed maximum a negative (positive) vertical shear of the horizontal velocity will adjust with a negative (positive) radial gradient of density leading to shoaling (deepening) of the isopycnals. Hereinafter we will sometimes refer to the domed upper layers as the eddy cap. As evident in Fig. 2.1, this transect also partially crossed two cyclonic eddies located one at each end of the transect. The combined vertical section of σ_Θ and cross-transect ADCP velocity clearly shows the signal of these eddies through the shoaling of the isopycnals and a cyclonic circulation (Fig. 2.2). Notice, however, that both structures are well separated from the PUMP eddy, so that the intrathermocline PUMP eddy may be considered as an isolated structure.

To describe the vertical structure of the PUMP eddy we have selected the Le Tourmalet transect (Fig. 2.1, white stars) as it crossed the eddy center and reached 1000 m depth. Figure 2.3 shows a combined vertical section of σ_Θ and cross-transect

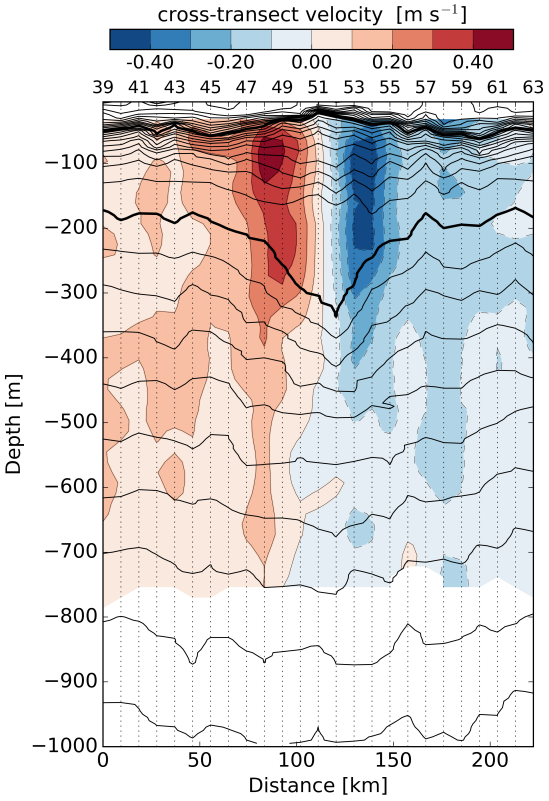

FIGURE 2.3: Vertical section of the cross-transect (zonal) ADCP velocity (positive values indicate eastward velocity and negative values indicate westward velocity) along the Le Tourmalet meridional transect (12-15 September 2014; Fig. 2.1, white stars) with superimposed contours of potential density anomaly, σ_Θ. Thick contours indicate σ_Θ = 25.5 kg m^{-3} and σ_Θ = 26.6 kg m^{-3} (contour interval is 0.1 kg m^{-3}). Vertical dotted lines show the CTD station positions, only odd station numbers are included for clarity.

(zonal) ADCP velocity along Le Tourmalet transect. The PUMP eddy is centered at station 51, and its signal is noticeable in both fields to at least ca. 500 m depth. Property anomalies (Figs. 2.4a-c) were calculated by subtracting at each depth the corresponding average of the reference stations (39, 40 and 62, 63) located at both ends of the transect. A vertical section of the σ_Θ anomaly (Fig. 2.4a) indicates that the eddy extends between stations 46 and 56, thus having a 92 km diameter. The corresponding eddy radius, 46 km, is of the order of the climatological first baroclinic Rossby radius of deformation for the region (Chelton et al., 1998).

In order to detail the vertical structure of the PUMP eddy, in Figs. 2.4d-f we zoom in on the upper 500 m of the water column. Vertical sections of conservative temperature and its anomaly (Figs. 2.4e, b) show that the eddy is characterized by a narrow

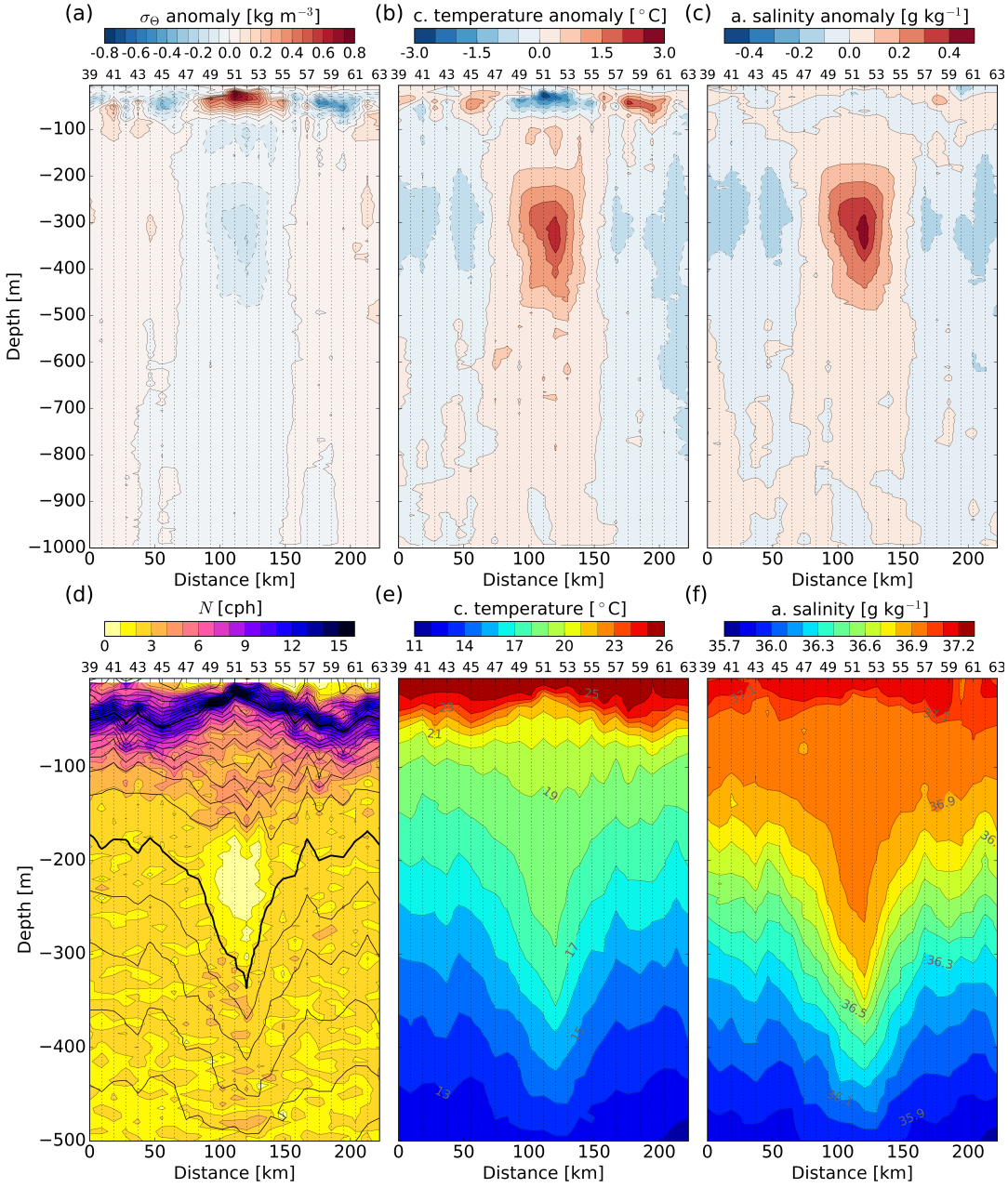

FIGURE 2.4: Vertical sections along the Le Tourmalet transect (Fig. 2.1, white stars) of the anomalies of (a) potential density anomaly, σ_Θ, (b) conservative temperature and (c) absolute salinity, computed with respect to the averaged value of the external casts (39, 40, 62 and 63) at each depth. Vertical sections of the (d) Brunt-Väisälä frequency, N, (e) conservative temperature and (f) absolute salinity. Black contours in (d) represent σ_Θ. Thick black contours indicate σ_Θ = 25.5 kg m^{-3} and σ_Θ= 26.6 kg m^{-3} (contour interval is 0.1 kg m^{-3}). Vertical dotted lines show the CTD station positions, only odd station numbers are included for clarity.

cold cap located at 30 m depth between stations 48 and 55 that is associated with seasonal thermocline shoaling, and by a deep warm core associated with deepening

of the main thermocline which introduces a conservative temperature anomaly of ca. +2.4°C. This warm core region is clearly recognizable in the conservative temperature anomaly section as the maximum anomaly located between stations 48 and 54; this region is 55 km wide and ranges from 200 to 500 m depth (Fig. 2.4b). The signature of the deep eddy core is also evident in the vertical sections of σ_Θ and absolute salinity anomalies (Figs. 2.4a, c) indicating that it is warmer, lighter and saltier than the surrounding waters. Therefore the vertical structure of the PUMP eddy shows a central deep core with sharp gradients of properties embraced by a peripheral region where the property gradients vary smoothly. We will refer to this deep region as the eddy hydrographic core.

A thermostad layer is also evident in the conservative temperature vertical section, trapped between the 18°C and 19°C isotherms (Fig. 2.4e). This nearly homogeneous interior layer is also evident in the vertical distributions of σ_Θ and absolute salinity as the pycnostad and halostad, respectively (Figs. 2.4d, f). In Fig. 2.4d the Brunt-Väisälä frequency N (defined as $N^2 = -(g/\rho_0)\partial_z\sigma_\Theta$, where g is gravity and ρ_0=1026 kg m^{-3} is the mean density) section shows the minimum in static stability introduced by this nearly homogeneous layer. The anomaly maxima introduced by the eddy reach the lower limit of the eddy hydrographic core region located at 500 m, which may be considered as the eddy base or eddy depth (Figs. 2.4a-c). Therefore, we may state that although the PUMP eddy has a vertical extension of 500 m depth, it perturbs the water column to at least the maximum sampled depth (1000 m).

The PUMP eddy also has a particular signature in the dissolved oxygen (DO) field. A vertical section of DO across the eddy center (Fig. 2.5a) shows the eddy has maximum values at the seasonal pycnocline. In particular, at the eddy hydrographic core, where the deeper part of the pycnostad is located, there is a well oxygenated column stretching from the seasonal pycnocline to the deeper layers accompanying the isopycnal deepening. We also derive the apparent oxygen utilization (AOU), which is the difference between saturated and observed DO concentrations (Fig. 2.5b). Therefore, a negative AOU indicates a DO excess in the water column, while a positive AOU indicates deficiency. According with the DO maximum at the seasonal pycnocline, there is a band of negative AOU which may be explained by *in situ*

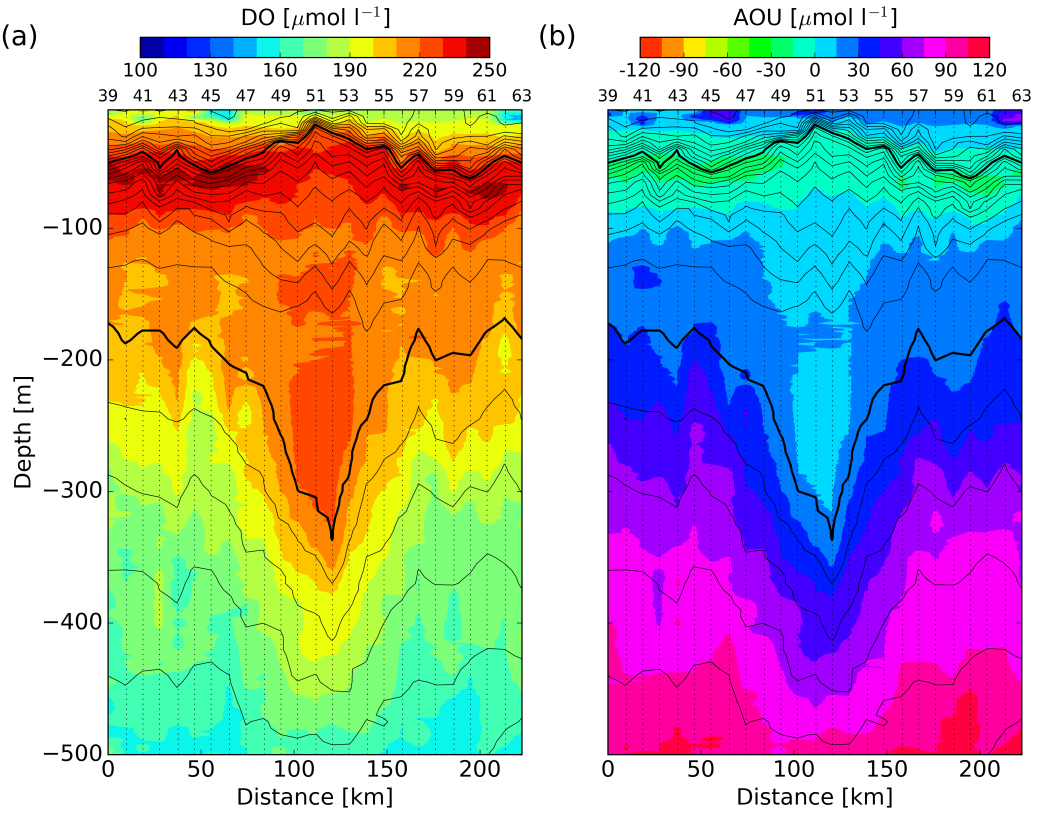

FIGURE 2.5: Vertical sections of (a) Dissolved oxygen (DO) and (b) apparent oxygen utilization (AOU) along the Le Tourmalet transect (Fig. 2.1, white stars). Contours represent potential density anomaly, σ_Θ. Thick contours are the 25.5 kg m^{-3} and 26.6 kg m^{-3} isopycnals (contour interval is 0.1 kg m^{-3}).

phytoplankton production. At the pycnostad there is a column of low AOU with respect to the surrounding waters. These low local values are well below the euphotic layer, thus being suggestive of subduction of rich DO negative AOU waters from the upper layers at the eddy center.

2.4 3D fields and dynamical variables

As explained in Section 2.2, after sampling the eddy with two SeaSoar transects (Phase 1), from where the eddy center was located and the radius estimated, a 166.68×166.68 km grid of 18.52×18.52 km resolution was sampled combining rosette casts at discrete stations with SeaSoar tows (Phase 2). 3D fields were obtained by objectively interpolating the CTD and ADCP data onto a regular grid of 11×11 km horizontal resolution and with a vertical resolution of 8 m (Bretherton et al., 1976;

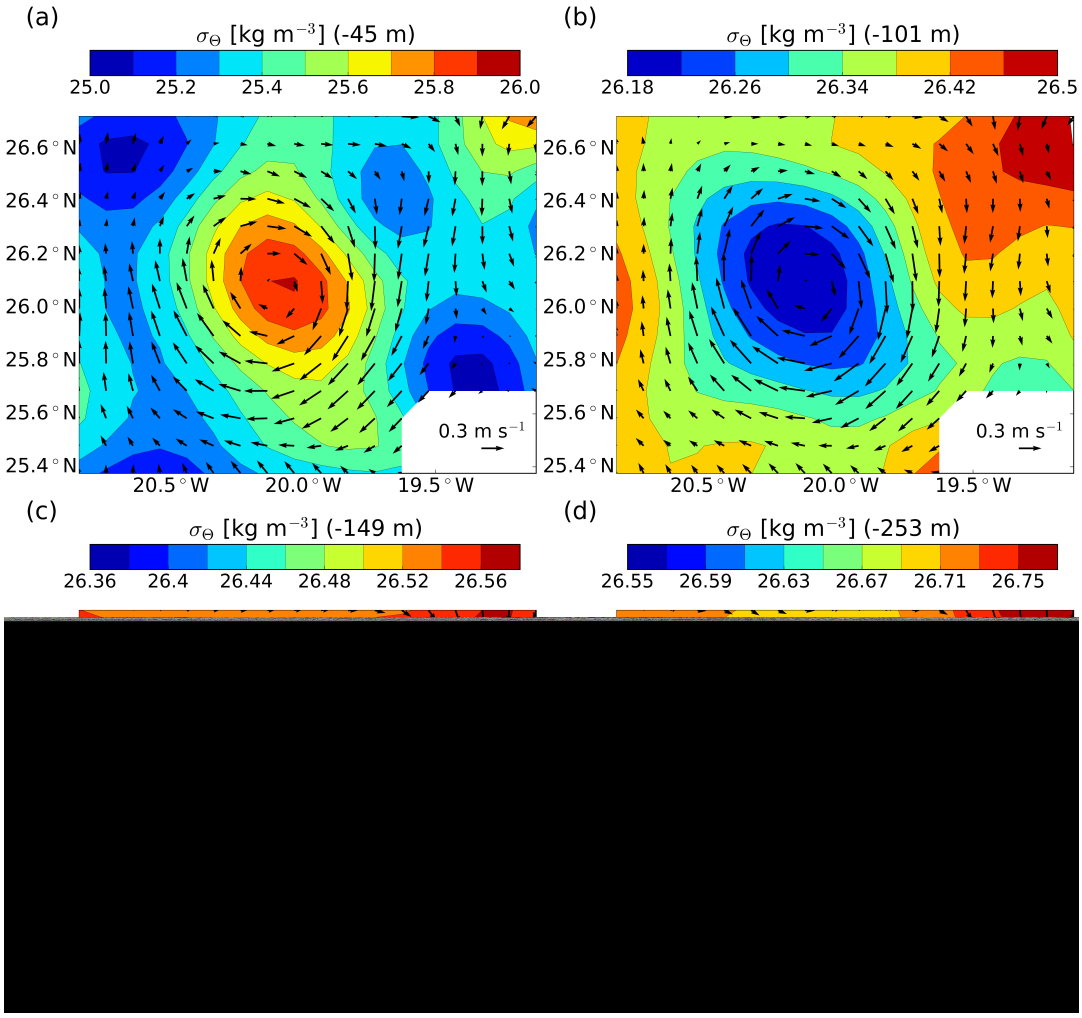

FIGURE 2.6: Objectively mapped ADCP velocity vectors with σ_Θ contours at different depths. Correlation scales used in the objectively interpolation are Lx = Ly = 40 km and the uncorrelated noise applied is 3%.

Le Traon, 1990). The data covariance was fitted with a 2D Gaussian function with semimajor and semiminor axes of Lx = Ly = 40 km (∼eddy radius). The mean fields were assumed to be planar for density and constant for ADCP velocity (Rudnick, 1996). The uncorrelated noise applied for the computation is 3% of the signal energy. The resulting interpolated fields provide a smoothed picture of the eddy when compared to the Le Tourmalet near submesoscale resolution transect. Figure 2.6 shows horizontal maps of σ_Θ at selected depths with the ADCP velocity vectors superposed. A horizontal map at the depth of the cold cap (Fig. 2.6a) shows the eddy signature at the center of the grid, with a density maximum at its center corresponding to the doming of the seasonal pycnocline. The eddy is delimited by the 25.5 kg

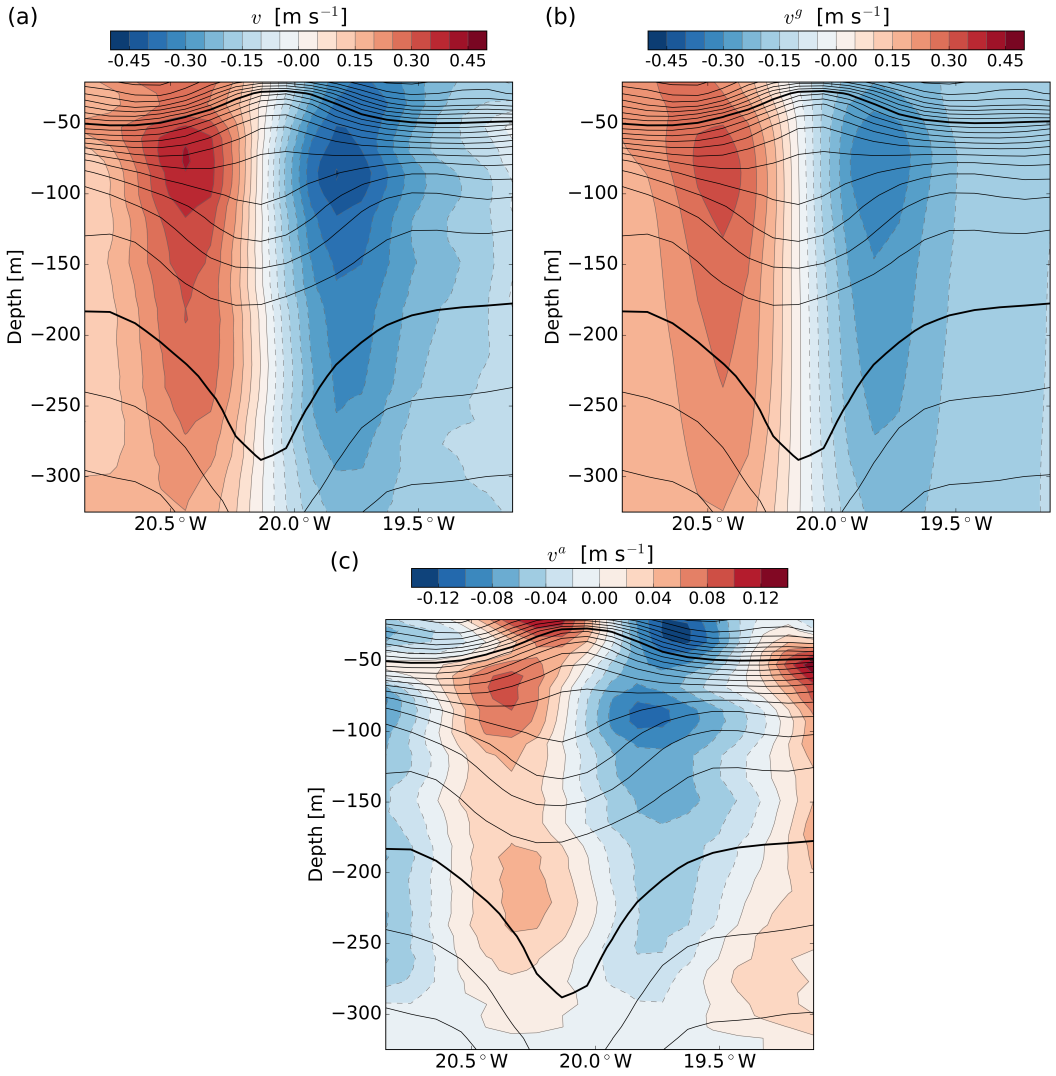

FIGURE 2.7: Vertical distributions of the meridional components of the (a) objectively mapped ADCP velocity, v, (b) geostrophic velocity, v^g, and (c) ageostrophic velocity, $v^a = v - v^g$, along 26.1°N. Black contours correspond to the objectively mapped potential density anomaly (σ_Θ, with a contour interval of 0.1 kg m^{-3}). Thick contours are the 25.5 kg m^{-3} and 26.6 kg m^{-3} isopycnals. Note different color scale in (c).

m^{-3} isopycnal and has an elliptical shape with its major axis oriented NW-SE and an aspect ratio (ar) of ar =155 km / 89 km=1.7. This density distribution resembles Fig. 6 of Viúdez and Dritschel (2003) that shows a filamented numerical eddy. In this regard, both vertices of the elliptic PUMP eddy show elongated structures which may be the roots of corresponding filaments. The corresponding velocity field for the cap section clearly shows asymmetry, with minimum speeds in the northern part of the eddy.

As shown in Fig. 2.6 the eccentricity of the eddy decreases with depth. Its center is displaced first westward (Fig. 2.6c) and then southward (Fig. 2.6d) with increasing depth, indicating that the eddy is vertically tilted. This tilting is clearly recognizable in the zonal section of σ_Θ (Fig. 2.7a), where the main pycnocline is displaced westward from the surface cap. Figure 2.7b shows the meridional component of the geostrophic flow computed through the thermal wind balance relations applying the ADCP data at the reference level (325 m depth). This smoothed section with respect to the Le Tourmalet section allows us to clearly see that the geostrophic velocity subsurface maximum coincides with the limiting region between the seasonal pycnocline doming and the permanent pycnocline deepening. Figure 2.7a also shows the meridional component of the ADCP velocity. The departure from geostrophy depicted in Fig. 2.7c is greater in the upper 100 m depth where the eddy-wind interaction is intensified. The dominance of an overall anticyclonic circulation indicates that $|\mathbf{u}| > |\mathbf{u}^g|$.

Figure 2.8a shows the horizontal distribution of the ADCP velocity magnitude at 85 m depth. Maximum values higher than 0.3 m s^{-1} are located around the eddy center except at the northern edge of the eddy where the ADCP velocity diminishes. As the ADCP velocity is anticyclonic in all the sampled domain we can refer the ADCP velocity magnitude as speed under the influence of the eddy, or eddy speed. A vertical profile of the horizontally averaged ADCP velocity magnitude is shown in Fig. 2.8b. A subsurface maximum is located between 80 and 100 m depth, from this depth the speed decreases to the maximum available ADCP depth (625 m). This subsurface maximum region will be referred to as the eddy dynamical core. Recall that the eddy base depth as derived from the anomaly fields is 500 m, below which the horizontally averaged eddy speed is still significant indicating that the eddy influences the water column well below its base. If the eddy swirl velocity is faster than the translation speed, the eddy is nonlinear (Flierl, 1981; Chelton et al., 2007). This is an important property because, in this case, water parcels will remain trapped inside the eddy and the surrounding water will be prevented from entering the eddy. Therefore, in a nonlinear eddy the transported property anomalies will be maintained inside the eddy. In the case of the PUMP eddy the horizontally averaged eddy speed exceeds the translation speed over the full depth range, thus suggesting

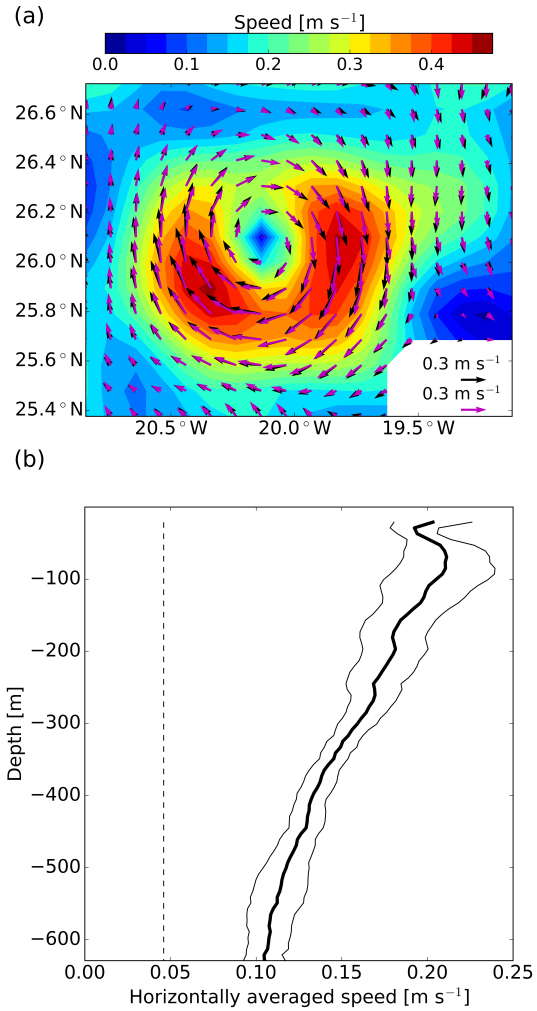

FIGURE 2.8: (a) ADCP velocity magnitude at 85 m depth. Black arrows represent ADCP velocity vectors whereas magenta arrows correspond to geostrophic velocity vectors. (b) Vertical profile of the horizontally averaged ADCP velocity magnitude (thick black line) with the standard deviation represented by thin black lines. Dashed line indicates the mean translation speed (0.046 m s^{-1}).

strong nonlinearity. The eddy translation speed of 4 km d^{-1} westwards (0.046 m s^{-1}, dashed line in Fig. 2.8b) was derived from the eddy center displacement between the north-south SeaSoar transect in Phase 1 (Fig. 2.1, cyan line) and the Le Tourmalet transect (Fig. 2.1, white stars).

The vertical relative vorticity field, ζ, scaled by the planetary vorticity, f, (or Rossby number, Ro = ζ/f) is presented in Fig. 2.9 and clearly shows the signature of the eddy as a well defined region of negative relative vorticity. A minimum relative vorticity value of -0.6f is attained at the eddy dynamical core, increasing rapidly towards its periphery. The zonal vertical section crossing the eddy center (Fig. 2.9b)

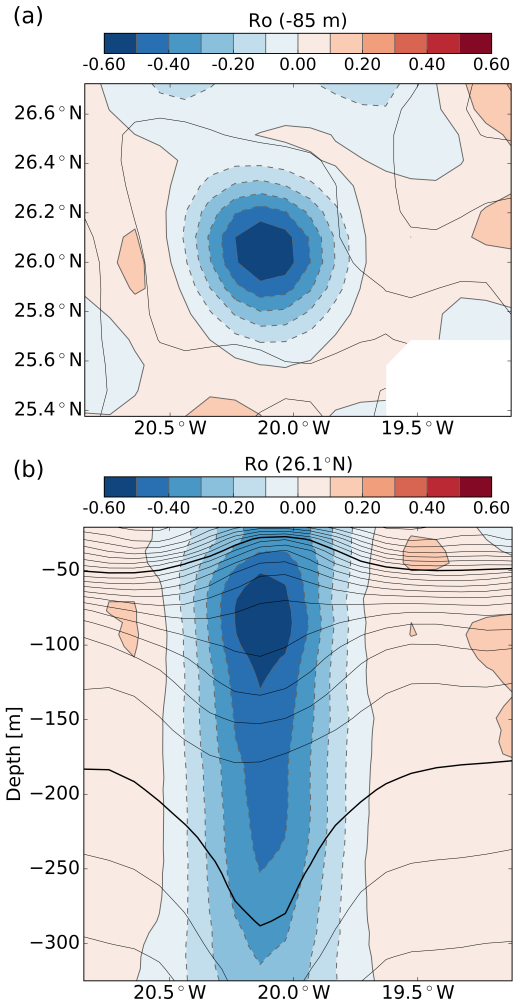

FIGURE 2.9: (a) Rossby number, Ro, horizontal distribution at 85 m depth. (b) Ro zonal section along 26.1°N. Black contours indicate the objectively mapped σ_Θ, with a contour interval of 0.1 kg m^{-3}. Thick contours are the 25.5 kg m^{-3} and 26.6 kg m^{-3} isopycnals.

shows, as for the velocity field, that the relative vorticity minimum values are just below the eddy cap (at the eddy dynamical core) with increasing values both above and below.

Details of the radial variability of the relative vorticity or related eddy rotation rate may be inferred from the high-resolution Le Tourmalet transect. With this purpose we have plotted in Fig. 2.10 the corresponding radial profiles of the absolute azimuthal velocity and the period at the depth of maximum horizontal velocity, which is attained at the eddy dynamical core. The period is derived from the angular velocity, which is approximated by the azimuthal velocity divided by the radial distance. Azimuthal velocity shows a rapid linear increase from minimum values at the eddy

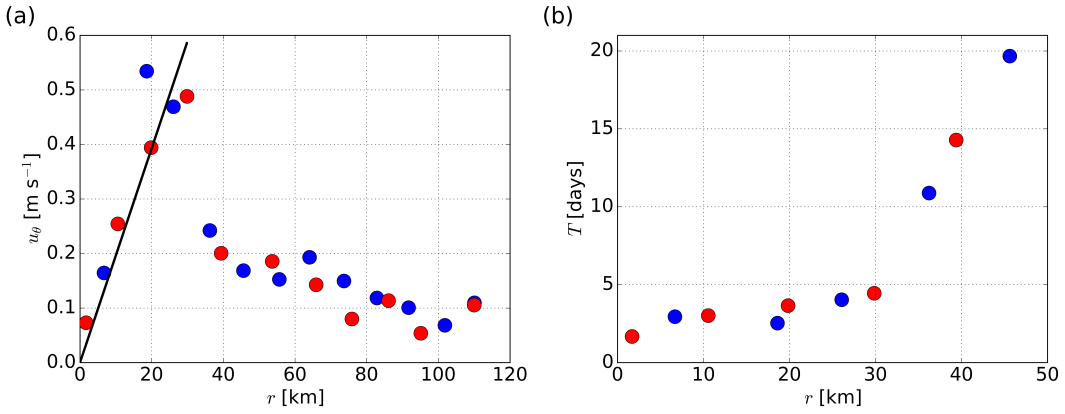

FIGURE 2.10: Radial sections of absolute azimuthal velocity, u_θ, (a) and orbital period (b) for the Le Tourmalet transect (Fig. 2.1, white stars). Sections are taken at the depth of maximum azimuthal velocity (97 m for the Le Tourmalet transect). Solid line in (a) shows the linear fit $u_\theta = \omega_0 r$, with ω_0 = 1.96×10^{-5} s^{-1} (angular velocity). (b) Represents the radial distribution of the orbital period computed as $2\pi r/u_\theta$. Red and blue dots represent u_θ and T positions north and south of the eddy center, respectively.

center to maximum value at 30 km. From this radial limit, the velocity drops rapidly at first then more slowly. Our approximation of the radial period indicates that the inner region is in near solid body rotation, with an approximate rotation period of 4 days. We will refer to this inner region as the eddy core. Beyond the eddy core edge (eddy core radius R_c = 30 km) the rotation rate rapidly decreases. Therefore the PUMP eddy is composed of an inner core region in fast solid body rotation and a thin outer ring that rotates much more slowly. We may also derive the rotation rate and scaled relative vorticity (Rossby number) at the eddy center from the local slope of the azimuthal velocity profile at the origin, as done by Caldeira et al. (2014) (solid line Fig. 2.10a). The rotation period at the eddy center is 3.7 days, and the absolute value of the scaled relative vorticity $|\mathrm{Ro}|$=0.61 which agrees with the value computed from the coarser resolution 3D data.

A mesoscale eddy can be described as a potential vorticity anomaly relative to its surrounding waters (Allen et al., 2012). Ertel's potential vorticity (PV) can be expressed as:

$$PV = -\frac{(-\partial_z v, \partial_z u)\cdot\nabla_h \sigma_\Theta}{\rho_0} - \frac{(\zeta + f)\partial_z \sigma_\Theta}{\rho_0}, \tag{2.1}$$

where ρ_0=1026 kg m^{-3} is the mean density. The first term on the right-hand side is named the tilting term while the second is the stretching term, which involves the

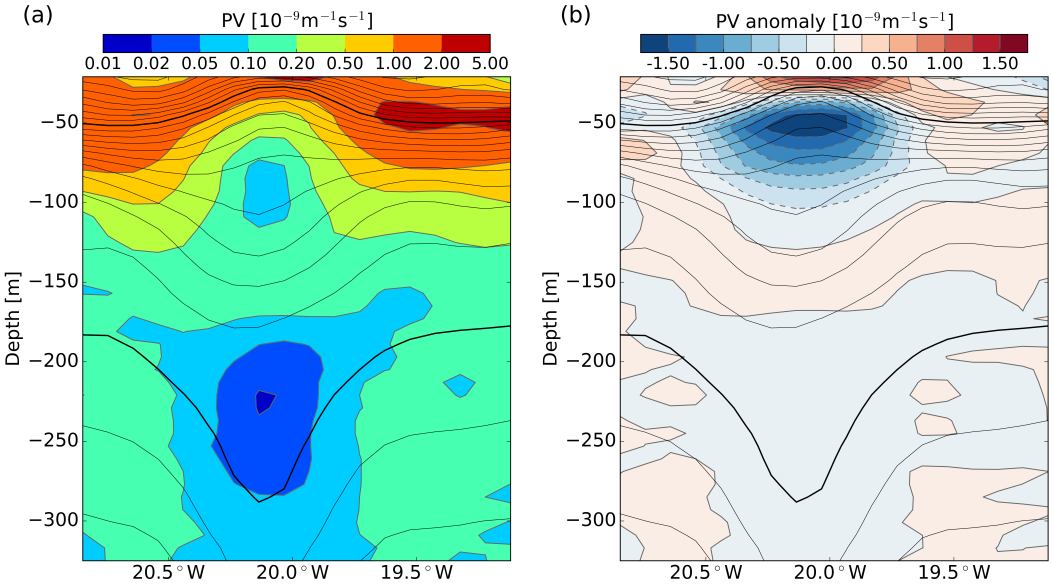

FIGURE 2.11: (a) Potential vorticity and (b) potential vorticity anomaly zonal sections along 26.1°N. The potential vorticity anomaly is computed with respect to the averaged external grid values for each depth layer. Black contours indicate the objectively mapped σ_Θ, with a contour interval of 0.1 kg m^{-3}. Thick contours are the 25.5 kg m^{-3} and 26.6 kg m^{-3} isopycnals.

vertical gradient of the potential density anomaly, σ_Θ. For the PUMP eddy the tilting term is two orders of magnitude smaller than the stretching term (not shown). Hence, the stretching term, and, in consequence, the vertical gradient of density (stratification or static stability), dominates the PV distribution. Therefore, it is expected that intrathermocline eddies will contain negative anomalies of PV as they lower the background static stability. A PV zonal section crossing the eddy center (Fig. 2.11) indicates that, overall, the eddy signal lowers the PV, introducing a negative anomaly, and also there is some vertical variability that merits examination. In the near surface layer, between the surface and ca. 30 m, the strong stratification introduced by the isopycnal doming increases PV, introducing a positive anomaly (Fig. 2.11b). Then, the PV decreases reaching a first local minimum between 75 and 110 m, where the bending of the isopycnals generates a local minimum of the static stability (Fig. 2.11a). This minimum PV region coincides with the location of the eddy dynamical core and, in consequence, with the location of the maximum subsurface ADCP velocity and relative vorticity. This first layer of low PV is reflected in the vertical section of the PV anomaly as a region of strong negative PV anomaly

and ranges from 30 to 110 m (Fig. 2.11b). Below, in the pycnostad layer between 175 and 325 m, we observe a second much broader region of minimum PV (Fig. 2.11a) which introduces lower negative anomalies in comparison with the upper minimum (Fig. 2.10b). Between both the dynamical and hydrographical core regions of minimum PV there is a relatively narrow layer of PV that is higher than the surrounding waters, ranging from 110 to 175 m (Fig. 2.11a).

2.5 Energetics

To infer the eddy content of available potential energy (APE) and kinetic energy (KE), we selected CTD and ADCP data from the Le Tourmalet meridional transect and followed the methodology proposed by Schultz Tokos and Rossby (1991). From Hebert (1988) and assuming that the eddy has a circular shape, APE is estimated using the integral:

$$APE = 0.5\rho_r \int_{-500}^{0} \int_{0}^{R} N_r^2 \delta^2 (2\pi r) dr dz, \tag{2.2}$$

where ρ_r and N_r are the density and the Brunt-Väisälä frequency of the reference state, and δ is the vertical displacement of the isopycnals within the eddy from the reference state. The reference state is the mean field as estimated from all CTD stations located at least 70 km from the eddy center. The integration is performed from the surface to the base of the eddy, located at 500 m, and from the eddy center to its radius, R = 46 km.

The total KE contained by the eddy is estimated using the integral:

$$KE = 0.5\rho_r \int_{-500}^{0} \int_{0}^{R} \mathbf{u}^2 (2\pi r) dr dz, \tag{2.3}$$

where $\mathbf{u}$ is the horizontal velocity as obtained from the ADCP. The resulting APE and KE for the PUMP eddy are APE = 5.64×10^{13} J and KE = 8.88×10^{13} J. These quantities are two orders of magnitude smaller than those corresponding to large eddies such as Gulf Stream or Aghulas rings (Olson et al., 1985; Clement and Gordon, 1995). However, if they are compared with corresponding eddies of similar size they are of the same order of magnitude (Table 2.1).

Author, description, location	PUMP	Schmid et al. (1995), Anticyclone Vitória eddy, Brazil Current	Hebert et al. (1990); Schultz Tokos and Rossby (1991), Meddy, NE Atlantic
KE ($\times 10^{13}$J)	8.88	9.6	7.9
APE ($\times 10^{13}$J)	5.64	19	7.5
KE/APE	1.58	0.51	1.1
Eddy radius, R (km)	46	50	65
Eddy thickness, H (m)	500	400	900
H/L ($\times 10^{-2}$)	0.5	0.4	0.7
Ro	0.6	0.20 - 0.28	0.3

TABLE 2.1: Energetics. Kinetic energy (KE) and available potential energy (APE) contents. R is the eddy radius, H is the eddy thickness and L is the eddy diameter.

The PUMP eddy contains more KE than APE, with the energy Burger number (D'Asaro, 1988) greater than unity, B_E = KE/APE = 1.58. As shown in Table 2.1 this higher content of KE than APE is a particularity of the PUMP eddy when compared with other eddies of similar size. The obtained B_E value is intermediate between those reported for large eddies, where the APE content exceeds the KE content leading to values of B_E<1 (Schmid et al., 1995; Clement and Gordon, 1995), and those reported for small submesoscale vortices where B_E >1 (D'Asaro, 1988). Prater and Sanford (1994) derived a relationship between B_E and the length-scale Burger number ($B_L = N^2H^2/f^2L^2$) and Rossby number, Ro:

$$B_E = \frac{KE}{APE} \approx \frac{B_L}{(1+Ro)^2}. \tag{2.4}$$

Using the background N^2, the eddy diameter L = 92$\times 10^3$ m and the eddy depth H = 500 m, the eddy length-scale Burger number is B_L= 0.20. With the eddy Rossby number based on the 3D data (Fig. 2.9) as Ro = -0.6, B_E is 1.25, which is very close to the value calculated above from the ratio KE/APE = 1.58. This scaling analysis of B_E suggests that B_E>1 is due both to a small aspect ratio, indicated by small B_L, and a relatively intense spin rate as indicated by a relatively large Ro. In this regard, notice that the eddies compared in Table 2.1 have similar aspect ratios but smaller

Ro than the PUMP eddy, which has a consistently smaller B_E.

2.6 Available heat and salt content anomalies

Available heat and salt content anomalies, AHA and ASA respectively, for the PUMP eddy were derived following the methodology of Chaigneau et al. (2011),

$$AHA = \int_{-500}^{0} \int_{0}^{R_c} \rho C_p \Theta'(2\pi r) dr dz \tag{2.5}$$

$$ASA = 0.001 \int_{-500}^{0} \int_{0}^{R_c} \rho S'(2\pi r) dr dz, \tag{2.6}$$

where C_p is the specific heat capacity (4000 J kg^{-1} K^{-1}), ρ the density, and the conservative temperature and absolute salinity anomalies (Θ' and S') are integrated over the area of the eddy core (assuming a circular shape) and then vertically integrated over the vertical extension of the eddy. To estimate these quantities we use the Le Tourmalet transect data as they reach the eddy base at 500 m depth. Temperature and salinity anomalies are computed with respect to the averaged value of the external casts (39, 40, 62 and 63) at each depth. We integrate radially from the eddy center to the eddy core radius (R_c = 30 km, Section 2.4). Vertical profiles of available heat and salt anomalies integrated only over the eddy core area (Fig. 2.12) show maximum (minimum) available contents of 0.014$\times$10^{18} J m^{-1} (-0.018$\times$10^{18} J m^{-1}) and 0.065$\times$10^{10} kg m^{-1} (-0.020$\times$10^{10} kg m^{-1}) at 300 m (35 m) depth, respectively. Although these available anomalies have opposite signs in the vertical, positive anomalies are broader and the vertically integrated AHA and ASA contents of the PUMP eddy are 2.9$\times$10^{18} J and 14.3$\times$10^{10} kg, respectively. The AHA and ASA contents are characteristics of the changing background along the eddy path, as well as of variation of eddy core properties with time due to exchange through eddy boundaries (e.g. Hebert et al., 1990).

Comparing the above values with those corresponding to intrathermocline eddies in other EBUS (Table 2.2), we notice that AHA and ASA contents are closely associated with the sizes of the eddies. The volume of trapped water transported by the PUMP eddy is 1.4$\times$10^{12} m^3, while intrathermocline eddies generated in the

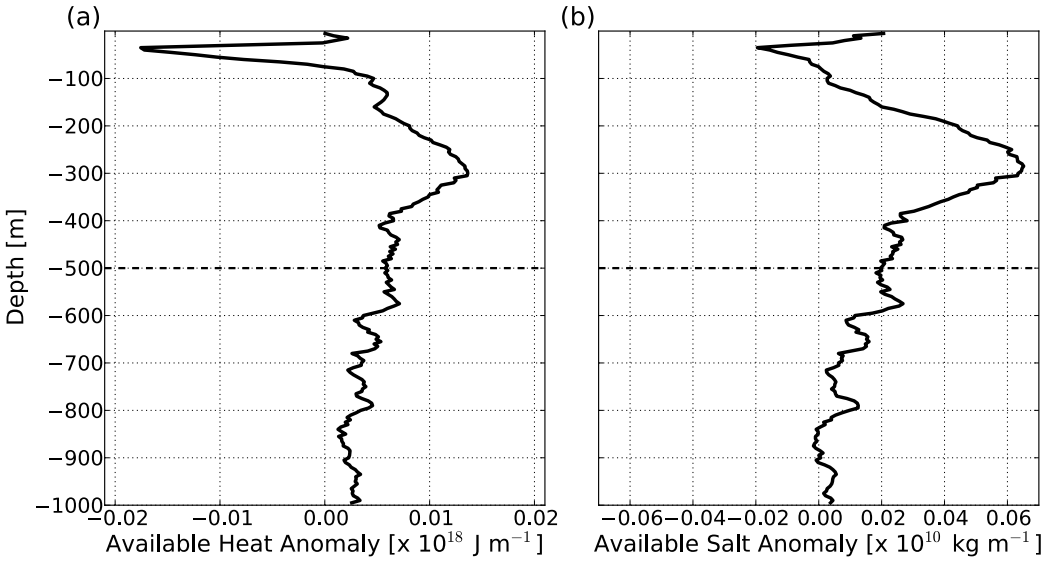

FIGURE 2.12: Vertical profiles of the available heat (a) and salt (b) content anomalies transported by the eddy core. Horizontal dashed lines represent the eddy base.

	PUMP	PCCS (Chaigneau et al., 2011)	Cuddies (Pelland et al., 2013)
Radius (km)	30	57.6	20.4
Vertical extent (m)	500	540	429
Volume ($\times 10^{12}$ m^3)	1.4	5.5	0.56
AHA ($\times 10^{18}$ J)/AHA*($\times 10^{6}$ J m^{-3})	2.9/2.1	8.7/1.6	0.36/0.6
ASA ($\times 10^{10}$ kg)/ASA*($\times 10^{-1}$ kg m^{-3})	14.3/10	23.8/4	1.58/2

TABLE 2.2: Radius and vertical extent of the eddy core defined as the inner eddy region that is in near solid body rotation. Volume, available heat anomaly (AHA), and available salt anomaly (ASA) trapped and transported by the eddy core. PCCS refers to Peru-Chile Current System while Cuddies are generated in the California EBUS. AHA* and ASA* are available heat and salt anomalies per unit volume, respectively.

Peru-Chile Current System (PCCS) have a mean volume of 5.5×10^{12} m^3 (Chaigneau et al., 2011). Hence, these eddies contain higher available heat and salt anomalies than the PUMP eddy. On the other hand, intrathermocline eddies generated by the California Undercurrent (Cuddies; Pelland et al., 2013) are smaller with an estimated volume of 0.56×10^{12} m^3. Furthermore, if we compare the relative contents of available heat and salt anomalies per unit volume it turns out that the PUMP eddy

transports warmer and saltier water than intrathermocline eddies of the PCCS and California EBUS. The PUMP eddy has an AHA per unit of volume almost double that of PCCS intrathermocline eddies, and more than three times that of Cuddies. On the other hand, ASA per unit volume in the PUMP eddy is more than two times higher than in PCCS eddies, and more than four times that of Cuddies. Therefore, in terms of units per volume the PUMP eddy ASA and AHA contents exceed those corresponding to the eddies analyzed here.

2.7 Discussion

2.7.1 Negative potential vorticity anomaly and eddy structure

The PUMP eddy is characterized by a biconvex isopycnal shape with an embedded pycnostad layer. The biconvex shape, which occurs in the near surface layers, is associated with the vertical shear induced by the subsurface maximum of ADCP velocity in accordance with thermal wind balance. This vertical structure of the density field introduces a decrease of the static stability which induces a subsurface PV minimum and, hence, a negative PV anomaly (Fig. 2.11). This subsurface region of negative PV anomaly, maximum absolute relative vorticity, and maximum ADCP velocity may be thought of as the eddy dynamical core. It is limited radially by the maximum azimuthal velocity and is in near solid body rotation (Fig. 2.10). Negative PV anomaly within the eddy and a central core rotating in near solid body rotation surrounded by a more slowly rotating outer ring are defining properties of intrathermocline eddies (Schultz Tokos and Rossby, 1991; Gordon et al., 2002; Hansen et al., 2010).

Another common feature of intrathermocline eddies is the occurrence of a pycnostad, which is a homogenous density layer embedded within the eddy. In the case of the PUMP eddy the pycnostad is trapped between the 26.5 kg m^{-3} and 26.6 kg m^{-3} isopycnals and the corresponding thermostad between the 18°C and 19°C isotherms (Fig. 2.4). As shown in Fig. 6 of Arístegui et al. (1994) in May, the month of the PUMP eddy generation, the upper part of the water column in the eddy generation area (Canary Islands) shows a nearly vertically homogeneous subsurface water layer trapped between the 18°C and 19°C isotherms and capped by the seasonal

thermocline. This layer has characteristics of subtropical mode water and is formed by winter convection that sets up a deep mixed layer which is subsequently capped by the seasonal thermocline (Arístegui et al., 1994; Hanawa and Talley, 2001). Therefore, the pycnostad embedded within the PUMP eddy contains mode water that may have been trapped inside the eddy during the eddy generation process. As already mentioned, Caldeira et al. (2014) describe an intrathermocline eddy generated by Madeira, which is located north of the Canaries. They also observed, at its early stage of formation, a pycnostad within the eddy core composed of Madeira Mode Water trapped within the 17°C-18°C isotherms, thus being slightly cooler than the mode water trapped by the PUMP eddy at the Canaries, 200 nautical miles to the south. This adds evidence to the hypothesis that the pycnostad embedded within the PUMP eddy is generated early in the eddy birth process as a consequence of trapping of subtropical mode water. Indeed, the trapping of well-mixed water during the eddy generation process is already observed in swoddies, generated in the northwestern coast of the Iberian Peninsula. Swoddies, although generated 1000 nautical miles to the north of the Canaries, usually have similar sizes as the PUMP eddy (see Section 2.1). Moreover, they usually have a similar $|Ro|$ of 0.4-0.5, a rotation rate of the eddy center of 3-3.5 days and a saltier, warmer and lighter core than the surrounding waters (Pingree and Le Cann, 1992a,b; Sánchez and Gil, 2004).

Mode waters have clear signatures in PV fields as negative anomalies due to the local decrease of static stability which is conserved, and thus constitute reservoirs of low PV (Hanawa and Talley, 2001; Sato and Polito, 2014). This is reflected in our vertical section of PV where low static stability values at the pycnostad are associated with a second region of minimum PV (centered between 175 and 325 m depth). This deeper PV minimum is much broader than the upper PV minimum located at the dynamical core (Fig. 2.11a). The negative PV anomaly that is introduced is, however, smaller than the upper layer PV anomaly (Fig. 2.11b).

2.7.2 Intrathermocline eddies in the Canary Eddy Corridor

Pingree (1996) gave the first description of an intrathermocline eddy inside the Canary Eddy Corridor. The eddy was first detected by the trajectory of a drogued Argos buoy near 23°W and 26°N in February 1993, close to the location of the PUMP eddy (20°W, 26°N). The similar location of both eddies in the Canary Eddy Corridor suggests that the eddy analyzed by Pingree (1996) was also generated by the Canary Islands. The drogued buoy tracked the westward movement of the eddy for at least 20 months and the eddy was sampled in December 1993 at 33°W, 1000 km west of the location of the first observation. In the intervening period the seasonal thermocline had been replaced by a deep, 100 m, mixed layer due to winter convection. The eddy was formed by a subsurface warm water lens located just below the mixed layer. Pingree (1996) named this structure the "shallow subtropical subducting westward propagating eddy" or Swesty.

In Table 2.3 we compare the characteristics of PUMP and Swesty eddies. At the time of the survey the ca. 18 months old Swesty was located ca. 1800 km from the Canary Islands and migrating westward displacement at ca. 100 km month^{-1}. The PUMP eddy was younger, 4 months old, which may explain its shorter rotation period, greater central vorticity and stronger azimuthal current maximum when compared with Swesty values (Table 2.3). The PUMP eddy dynamical core was at 85 m depth whereas the Swesty dynamical core was at 190 m. As they have probably the same origin, the deeper Swesty core may support the suggestion of Pingree (1996) on core subduction as Swesties self-propagate westward along inclined isopycnals. Pingree estimated a subduction velocity of ca. 40 m y^{-1}, while the difference in the eddy core depths and their age provides an estimate of twice that figure. Like the PUMP eddy, the Swesty showed biconvex shape of the isopycnals associated with an anomaly of potential vorticity 91% below ambient potential vorticity (Table 2.3). It is expected that due to winter convection, subduction and lateral mixing the PUMP eddy may evolve towards Swesty characteristics as it propagates westwards.

Pegliasco et al. (2015) recently investigated and compared the vertical structure of the eddy field in the four eastern boundary upwelling system (EBUS) from altimetry and Argo buoy data. They observed that 40% of anticyclonic eddies in

Property (units)	PUMP	Swesty
Distance from the Canaries (km)	550	1887
Age (month)	4	18
Radius (km)	46	60
Vertical extent (m)	500	600
Mixed layer above the core (m)	10	100
Westward self propagation (km d^{-1})	4	3.3
Dynamical core depth (m)	85	190
Temperature anomaly (°C)	+3	+1.5
Core rotation period (d)	4	8
Central vorticity, ζ/f	-0.6	-0.3
Anomaly of potential vorticity below ambient (%)	95	92
Maximum azimuthal current velocity (m s^{-1})	0.5	0.16
Radius of maximum azimuthal current velocity (km)	30	30

TABLE 2.3: Swesty (Pingree, 1996) and PUMP eddy characteristics

the Canary EBUS are intrathermocline eddies. Most of those eddies are generated inside the Canary Eddy Corridor south of the Canary Islands, as was the PUMP eddy. The composite vertical structure of those eddies shows subsurface intensified temperature and salinity anomalies similar to the PUMP and Swesty eddies. When comparing the composite vertical structures of subsurface eddies in other EBUS systems, one striking feature is that the Canary Eddy Corridor subsurface eddies have weaker anomalies and are shallower. This may be a response to their different origins. Cuddies of the California EBUS and subsurface eddies of the Peru-Chile EBUS have their origins in the poleward undercurrents of their respective upwelling systems (e.g., Pelland et al., 2013; Hormazabal et al., 2013). These are deeper structures than the PUMP eddy with maximum current velocity at depths of several hundred meters and minimum oxygen anomalies instead of maximum oxygen anomalies. Shallower anomalies in the Canary EBUS and the observations of the PUMP and the Swesty eddies are consistent with the Canary Islands being the main source of intrathermocline eddies for the Canary Eddy Corridor, and with the domination of this shallower eddy type over deeper, low oxygen intrathermocline type eddies

originating in the poleward undercurrent at the African coastal margin. South of the Canary Eddy Corridor the percentage of subsurface eddies decreases dramatically to 9% and are deeper subsurface intensified type (Schütte et al., 2015).

2.8 Summary and conclusions

The Canary Eddy Corridor is the main pathway of long-lived eddies for the north-eastern subtropical Atlantic (Sangrà et al., 2009). As most of these long-lived eddies are anticyclones, it is a suitable region for their study. Our survey of an anticyclonic eddy inside the Canary Eddy Corridor provided for the first time an intensive sampling of one of these long-lived intrathermocline anticyclones. During the interdisciplinary cruise, we carried out near submesoscale 2D sampling as well as mesoscale 3D sampling of the eddy structure. With the data set obtained in the cruise, several works will be published in order to detail the eddy submesoscale structure, ageostrophic secondary circulation (Barceló-Llull et al., 2017a), near-inertial wave trapping and physical-biological interactions. The analysis presented here will serve as hydrographic background to the other PUMP studies.

In this study we examined in detail the anatomy of an intrathermocline eddy whose structure is characterized by a biconvex shape of the isopycnals and by a homogeneous layer of subtropical mode water embedded within. Our observations highlight that this structure of an intrathermocline eddy is associated with both a shallow and a deep minimum of PV. The decrease in static stability induced by the biconvex shape of the isopycnals gives rise to the shallower PV minimum located at 85 m depth. We call this region the eddy dynamical core as it is associated with a subsurface maximum in horizontal velocity and also a maximum of absolute relative vorticity. Below this, centered at 225 m depth, there is a second broad PV minimum generated by the presence of the pycnostad layer composed of subtropical mode water. The occurrence of a subsurface maximum of the velocity field and vertical shear is associated with the biconvex shape of the isopycnals through thermal wind balance.

The eddy studied was 92 km in diameter and 500 m in depth, although it was

found to influence the hydrographic field down to at least 1000 m. Above the dynamical core, the doming of the seasonal thermocline and pycnocline leads to a narrow cold region in the surface layers introducing a conservative temperature anomaly of -3°C. Below the dynamical core, the deepening of the permanent thermocline, halocline and pycnocline leads to a broad, warmer, saltier and lighter region located between 200 and 500 m, where the conservative temperature anomaly attains ca. +2.4°C. We call this region the eddy hydrographic core. We also observe a relative maximum of DO in this region and a negative AOU, that may be interpreted as a sign of subduction during the eddy generation process due to the initial deepening of the isopycnals. The eddy has an elliptical shape with signs of shallow filaments at the vertices of the ellipse. It has a central core of 30 km radius in near solid body rotation with a period of ca. 4 days surrounded by a narrow outer ring of 16 km width that rotates much more slowly. The corresponding Rossby number at the eddy center (Ro = -0.6) is quite high when compared to other subsurface eddies and is reflected in a larger content of KE than APE. The eddy introduces available heat and salt content anomalies of 2.9×10^{18} J and 14.3×10^{10} kg, respectively. These values are larger than those associated with intrathermocline eddies of the California EBUS, and on the same order of magnitude as intrathermocline eddies of the Peru-Chile EBUS.

Chapter 3

Ageostrophic secondary circulation in a subtropical intrathermocline eddy

Barceló-Llull, B., Pallàs-Sanz, E., Sangrà, P., Martínez-Marrero, A., Estrada-Allis, S. N., and Arístegui, J. (2017). Ageostrophic secondary circulation in a subtropical intrathermocline eddy. *J. Phys. Oceanogr.* **47** (5), 1107-1123, doi: 10.1175/JPO-D-16-0235.1

Abstract

Vertical motions play a key role in the enhancement of primary production within mesoscale eddies through the introduction of nutrients into the euphotic layer. However, the details of the vertical velocity field (w) driving these enhancements remain under discussion. For the first time the mesoscale w associated with an intrathermocline eddy is computed and analyzed using *in situ* high-resolution three-dimensional (3D) fields of density and horizontal velocity by resolving a generalized omega equation valid for high Rossby numbers. In the seasonal pycnocline the diagnosed w reveals a multipolar structure with upwelling and downwelling cells located at the eddy periphery. In the main pycnocline w is characterized by a dipolar structure

with downwelling velocities upstream of the propagation path and upwelling velocities downstream. Maximum values of w reach 6.4 m d^{-1}. An observed enhancement of chlorophyll-a at the eddy periphery coincides with the location of the upwelling and downwelling cells. Analysis of the forcing terms of the generalized omega equation indicates that the mechanisms behind the dipolar structure of the w field are a combination of horizontal deformation and advection of vertical relative vorticity by ageostrophic vertical shear. The wind during the eddy sampling was rather constant and uniform with a speed of 5 m s^{-1}. Diagnosed nonlinear Ekman pumping leads to a dipolar pattern that mirrors the inferred w. Horizontal ageostrophic secondary circulation is dominated by centripetal acceleration and closes the dipole w structure. Vertical fluxes act to maintain the intrathermocline eddy structure.

3.1 Introduction

Mesoscale eddies are ubiquitous features of the world ocean and are associated with important biogeochemical activity due to both their horizontal and vertical motions (McGillicuddy, 2016). There are two types of eddies depending on their sense of rotation: anticyclonic eddies, which have negative (positive) vertical relative vorticity, and cyclonic eddies, which are characterized by positive (negative) vertical relative vorticity in the north (south) hemisphere. A particular type of anticyclones are intrathermocline eddies which are subsurface intensified eddies also rotating anticyclonically but with dome-shaped (bowl-shaped) isopycnals in the upper (lower) layers (McGillicuddy et al., 2007).

Ageostrophic secondary circulation (ASC), which includes the ageostrophic horizontal velocity and the vertical velocity, has an important role within mesoscale structures through the restoring of thermal wind balance. The vertical velocities associated with ASC play an important role in the oceanic vertical pump (Klein and Lapeyre, 2009), which has been defined as those physical processes, mainly at the submesoscale range [spatial scales below the first baroclinic Rossby deformation radius, 0.1-10 km (Shcherbina et al., 2015)], that drive intense nutrient fluxes into the euphotic layer, changing plankton community structure and enhancing primary

production and, hence, having a major impact on the marine carbon cycle. Measuring vertical velocities in the ocean is challenging because of their small order of magnitude when compared with horizontal velocities, W$\sim$(10^{-3}, 10^{-4})U$\sim$10 m d^{-1} for the mesoscale, and W$\sim$(10^{-2})U$\sim$100 m d^{-1} for the submesoscale (Mahadevan and Tandon, 2006). Attempts to measure vertical velocities in the ocean include tracer release experiments and Lagrangian isopycnal drifter measurements (Hansen and Paul, 1987; Schultz Tokos et al., 1994; Lindstrom and Watts, 1994; McGillicuddy et al., 2007; Harcourt et al., 2002; D'Asaro et al., 2011). Although these attempts have provided an estimate of vertical velocities, they have not been able to give details of the corresponding fields and, thus, details of the forcing mechanisms. As detailed next, with this purpose different approaches were envisaged through the inference of the vertical velocity field from the sampled density and horizontal velocity fields using distinct forms of the so-called omega equation or inverse methods (Viúdez et al., 1996; Thomas et al., 2010).

Methods to infer vertical velocity from diagnostic equations in geophysical flows were first derived for the atmosphere. Hoskins et al. (1978) used quasi-geostrophic theory (QG) to diagnose vertical motion in the atmosphere by implementing the Q vector form of the omega equation that is valid for the low Rossby number (Ro) regime. In their formulation, QG vertical velocity results from the adjustment process that takes place when thermal wind balance is destroyed by the geostrophic deformation field (Durran and Snellman, 1987). Tintoré et al. (1991) and Pollard and Regier (1992) reformulated the QG omega equation for the ocean in order to estimate vertical velocities in oceanic mesoscale frontal regions. Since these earlier studies, the QG omega equation has been widely applied to infer vertical velocities in oceanic mesoscale features, taking advantage of the fact that only the measured density field and related variables are needed (Shearman et al., 2000; Martin and Richards, 2001; Rodríguez et al., 2001; Benítez-Barrios et al., 2011; Pascual et al., 2015; Barceló-Llull et al., 2016). Further developments of the omega equation in order to provide more accuracy in the diagnosis of vertical velocity include the ageostrophic advection of geostrophic velocity leading to the so-called semigeostrophic (SG) omega equation (Hoskins and Draghici, 1977). This ageostrophic advection becomes relevant where there are significant horizontal variations in static stability and potential vorticity,

such as in sharp fronts, leading to high Ro and thus invalidating the QG form (Pedder and Thorpe, 1999; Badin, 2012). As for the QG form, the SG form allows, in practice, the computation of vertical velocity from geostrophic flow as obtained from density measurements only (Pinot et al., 1996).

Prior to the reformulation by Hoskins et al. (1978) into the Q vector form, the first formulation of the omega equation presented an undesirable cancellation of the forcing terms that made determination of their relative strengths extremely difficult (Trenberth, 1978). To solve this difficulty, Viúdez et al. (1996) proposed a generalized form of the omega equation for the ocean in terms of the material rate of change of the differential ageostrophic vertical relative vorticity, instead of the local rate of change of the differential geostrophic vertical relative vorticity. Using primitive equation numerical experiments, Viúdez and Dritschel (2004) tested the accuracy of the three cited forms of the omega equation, concluding that the generalized form was the most accurate in the diagnosis of vertical velocities. Therefore, the generalized omega equation of Viúdez et al. (1996) is both less restrictive and more accurate than the Q vector based QG and SG forms and, in addition, it allows vertical velocity diagnoses in highly ageostrophic environments. However, as it is primitive equation based, one disadvantage of this form is that it requires measurements of both the density and horizontal velocity fields. As in this study we have accurately measured both these fields, we will apply the generalized omega equation form derived by Viúdez et al. (1996) for the diagnosis of vertical velocities and the related ASC in our sampled subtropical intrathermocline eddy.

As the along-front flow may be considered linear, vertical velocity in mesoscale frontal regions can only be diagnosed from cross-front vertical sections of density (QG and SG omega equation forms) or from both cross-front vertical sections of density and horizontal velocity (generalized omega equation form). Two-dimensional and three-dimensional diagnoses have contributed to a better understanding of ASCs and the associated processes in these regions (Pollard and Regier, 1992; Allen and Smeed, 1996; Naveira Garabato et al., 2001; Pallàs-Sanz et al., 2010a,b). However, in the case of mesoscale eddies, as the flow is nonlinear, a three-dimensional (3D) quasi-synoptic grid of the above fields is needed to diagnose vertical velocity with a generalized omega equation. For this reason, studies of ASCs in mesoscale

eddies are notable more scarce than they are in frontal regions. Allen and Smeed (1996) diagnose the vertical velocity at the Iceland-Færœs Front and the related eddy field using the QG omega equation from density data obtained from SeaSoar tracks. Their Fig. 11 shows a dipolar structure for the vertical velocity related with a cyclonic eddy, with an upwelling cell on one side and a downwelling cell on the other. However, due to the low resolution between SeaSoar tracks (50 km), it is difficult to well establish the details of such variability. They relate this dipolar pattern to vortex stretching. Martin and Richards (2001) also diagnose the vertical velocity field in an intrathermocline eddy using the QG omega equation, obtaining a multipolar vertical velocity distribution that may be consistent with an azimuthal perturbation of the eddy shape. However, the inferred vertical velocity field shows significant errors that arise from the necessary compromise between the spatial resolution and the synopticity of the eddy sampling (Klein and Lapeyre, 2009). Benítez-Barrios et al. (2011) estimate the QG vertical velocity in an intrathermocline eddy in the NW African coastal transition zone. Their low resolution data also suggest a dipolar structure for the QG vertical velocity field with a downwelling (upwelling) cell in the western (eastern) side. Buongiorno Nardelli et al. (2001) infer the QG vertical velocity in a cyclonic eddy in the Atlantic-Ionian stream, finding also a dipolar distribution of QG vertical velocity. More recently, Buongiorno Nardelli (2013) estimated the vertical velocity in a cyclonic Aghulas ring using the SG omega equation from combined satellite-*in situ* synthetic reconstructed data. His results show that the vertical velocity field is organized in a dipolar pattern within the eddy core and in an octopolar pattern along the eddy periphery consisting of alternating upwelling and downwelling cells. He suggests that these patterns could be related with vortex Rossby waves (McWilliams et al., 2003). Barceló-Llull et al. (2016) also diagnose the QG vertical velocity field in the southeast Pacific from a similar synthetic observation-based product combining satellite and *in situ* data. With this low resolution data ($1/3^o$) they find dipolar distributions of vertical velocity within mesoscale eddies.

Related with the difficulty of obtaining 3D quasi-synoptic fields with enough resolution, most of the studies of ASC in mesoscale eddies have been oriented toward

the particular process of the self-induced Ekman pumping, paying particular attention to its effects on chlorophyll-a distribution (Gaube et al., 2014, 2015). Three mechanisms have been identified that are linked with this process (Gaube et al., 2015). The first mechanism results from the wind stress curl induced by the differences between surface winds and ocean velocities that give rise to an Ekman upwelling (downwelling) at the cores of anticyclones (cyclones) (Martin and Richards, 2001; McGillicuddy et al., 2007; Gaube et al., 2015). As formulated by Stern (1965), the second mechanism arises from the interaction of the surface wind stress with the surface geostrophic vertical vorticity gradient, and results in mesoscale dipoles of Ekman upwelling and downwelling (McGillicuddy et al., 2008; Gaube et al., 2015). When the eddy periphery contains a submesoscale frontal region, it has been proposed that this second mechanism also leads to Ekman dipoles, but only at the periphery and at the submesoscale range (Mahadevan et al., 2008). The third mechanism is secondary and it is associated with the wind stress curl induced by sea surface temperature gradients (Chelton and Xie, 2010; Gaube et al., 2015). The first mechanism is named linear Ekman pumping and the second nonlinear Ekman pumping (McGillicuddy et al., 2008; Gaube et al., 2015).

There is growing evidence to indicate that anticyclonic eddies may be as productive as cyclonic ones in the enhancement of primary production [see recent review of McGillicuddy (2016)]. However, the details and mechanisms responsible for such enhancement are still under discussion. McGillicuddy et al. (2007) observed an extraordinary phytoplankton bloom at the core of a subtropical intrathermocline eddy and proposed that linear Ekmam pumping was the mechanism responsible. Alternatively Mahadevan et al. (2008), using numerical modelling, proposed that phytoplankton enhancement occurs at the eddy periphery at the submesoscale range due to the nonlinear Ekman mechanism and is then advected toward its core. Composite averages of chlorophyll-a and linear Ekman pumping as obtained from satellite data support the enhancement of chlorophyll-a at anticyclonic eddy cores due to linear Ekman pumping (Gaube et al., 2013, 2014). However, as shown in Fig. 3 of Calil and Richards (2010), instantaneous fields of altimetry and chlorophyll-a indicate that this enhancement occurs at the eddy periphery instead of at the eddy core, nonlinear Ekman pumping being a plausible candidate for such enhancement.

As already mentioned, there are few studies of ASC in mesoscale eddies due to the difficulty in obtaining quasi-synoptic 3D fields with high resolution. On the other hand, most of the attempts to investigate the influence of mesoscale eddies on chlorophyll-a distributions are based on remote sensing observations, due also to the difficulty in obtaining 3D *in situ* fields. Furthermore, these studies focused only on the self-induced Ekman pumping process without diagnosing the vertical velocity field as a result of all processes causing vertical motions as formulated by the generalized omega equation. To fill this gap, in September 2014 we conducted an interdisciplinary survey of a subtropical intrathermocline eddy in the framework of the Study of the Vertical Oceanic Pump in mesoscale eddies (PUMP) project. A detailed description of the eddy structure and dynamics may be found in Barceló-Llull et al. (2017b). Here we describe and discuss the eddy ASC and its role in chlorophyll-a enhancement using high-resolution quasi-synoptic 3D *in situ* fields.

3.2 Data and methods

3.2.1 Dataset and optimal interpolation

The PUMP interdisciplinary survey of a subtropical intrathermocline eddy was carried out from 3 to 20 September 2014 aboard the R/V BIO Hespérides. The PUMP eddy was generated 4 months earlier at the island of Tenerife in the Canary Islands. The Canary Islands continuously spin off mesoscale eddies that form the so-called Canary Eddy Corridor which is the main pathway for long-lived eddies in the subtropical northeast Atlantic (Sangrà et al., 2009). Guided by its signal in altimetric Sea Level Anomaly (SLA) fields, we first crossed the eddy with two transects sampled with continuous tows of a conductivity-temperature-depth (CTD) probe on an undulating vehicle (SeaSoar MK II) during the days 3-5 September 2014 (Fig. 3.1, black dashed lines) to locate the eddy center and determine its size. Then, in order to obtain the 3D fields for the diagnosis of vertical velocities, we sampled a grid centered on the eddy center. The grid consisted of six SeaSoar (Fig. 3.1, grey lines) and three discrete CTD (the SeaSoar CTD was attached to a CTD-rosette system after a failure of the SeaSoar; Fig. 3.1, grey dots) zonal transects of length 90 nautical miles; the distance between the transects was 10 nautical miles. The rosette stations were also

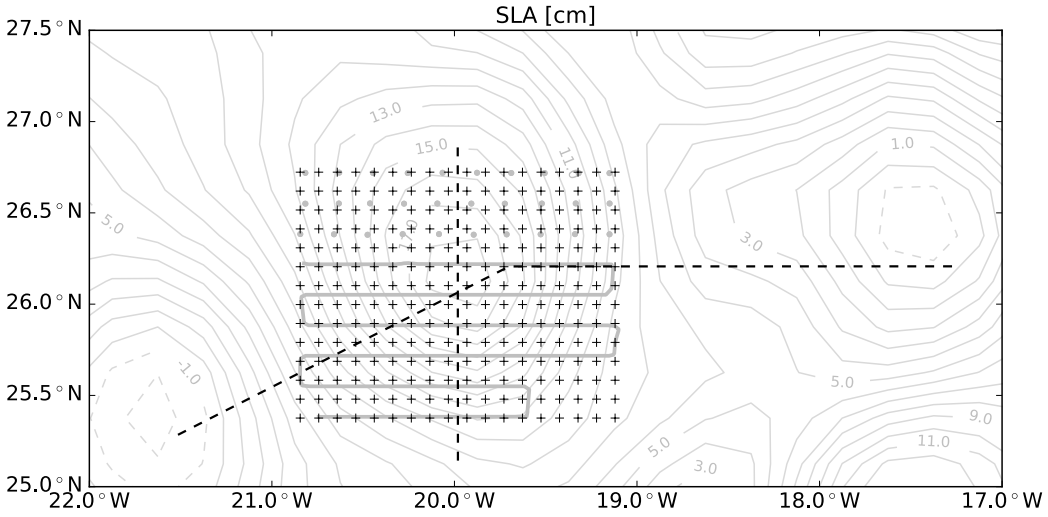

FIGURE 3.1: Map of the PUMP eddy sea level anomaly, SLA (cm), signal from AVISO on 6 September 2014 (grey thin contours). Black dashed lines represent the SeaSoar transects to detect the eddy center. Thick grey lines and dots show the grid for the 3D eddy sampling with SeaSoar continuous tows and CTD casts, respectively. Black crosses represent the interpolation grid.

10 nautical miles apart, while the SeaSoar undulating vehicle provided profiles separated by 4 km with an effective vertical resolution of 72 cm. The rosette transects were completed in ∼16 h, while the long (short) SeaSoar transects were completed in ∼12 h (9 h) with a ship speed of 8 knots. The time of navigation between transect was ∼1.5 h. The 3D survey was accomplished in 5 days (6-11 September 2014). With this sampling strategy we tried to reach a compromise between the spatial resolution and the synopticity of the eddy sampling (Martin and Richards, 2001). Allen et al. (2001) study the implications on vertical velocity estimations of the errors associated with the sampling strategy. They analyze a sampling strategy similar to the PUMP survey to sample mesoscale structures consisting of transects separated by ∼23 km and with an along-track resolution of ∼5 km, considering a ship speed of ∼8 knots, and with a total sampling duration of ∼4.5 days. They find that the vertical velocity distribution remains unaltered, while its magnitude is reduced because of the smoothing introduced by the sampling resolution, without alterations due to the lack of synopticity. Hence, we may conclude that the PUMP survey followed a sampling strategy well compromised to estimate vertical motions.

The SeaSoar MK II measurements extended from 10 m down to 325 m, while

discrete CTD casts were made to a nominal depth of 400 m. Both the SeaSoar MK II and CTD-rosette systems were equipped with CTD SB911+ probes, additionally equipped with a Seapoint Chlorophyll Fluorometer sensor which provided fluorescence measurements. Raw data files were processed with Sea-Bird SEASOFT software (http://www.seabird.com/software/softrev.htm) and vertically averaged into 8-m bins. TEOS-10 algorithms to calculate absolute salinity, S_A, and conservative temperature, Θ, and all derived variables were used (Feistel, 2003, 2008). Chlorophyll-a concentrations were estimated from the *in situ* fluorescence provided by the fluorometer sensor previously calibrated with 256 samples of extracted chlorophyll-a according to Holm-Hansen et al. (1965). The relationship between the readings of the fluorometer (F) and the chlorophyll-a concentration extracted from seawater samples (CHL) is CHL (mg m^{-3}) = 0.5078F - 0.005; R^2 = 0.5773; this was used to transform *in situ* fluorescence to actual chlorophyll-a.

In addition, current velocities were observed continuously through a hull-mounted RDI acoustic Doppler current profiler (ADCP) Ocean Surveyor, working at 75 kHz. The ADCP gave raw data with 5-min ensembles from the surface to 800 m depth and a bin size of 8 m. The raw data were quality controlled with the Common Oceanographic Data Access System (CODAS; Firing et al., 1995). On average, the controlled profiles provide good data from 21 to 625 m depth. The velocities were calibrated for transducer misalignment, adjusted from ship relative currents to absolute currents using GPS position measurements and spatially averaged each 0.09^o.

The density and horizontal velocity data were objectively interpolated onto a regular grid (Fig. 3.1, crosses) with a horizontal resolution of $0.1^\circ \times 0.1^\circ$ ($\sim$ half the original resolution of 10 nm) and a vertical resolution of 8 m (Bretherton et al., 1976). The data covariance was fitted with a 2D Gaussian function with semimajor and semiminor axes of Lx = Ly = 40 km. These correlation scales (Lx and Ly) were selected by analyzing the autocorrelation matrix of the observed fields and are of the order of the eddy radius. With this interpolation, wavelengths smaller than the correlation lengths of the covariance function are filtered (Le Traon, 1990). This smoothing is important for solving the omega equation as it requires computing second-order spatial derivatives of the interpolated fields (Pallàs-Sanz et al., 2010a).

The mean fields were assumed to be planar for density and constant for horizontal velocity (Rudnick, 1996). The uncorrelated noise is set to 3% of the signal energy (Rudnick, 1996; Pallàs-Sanz et al., 2010a). From chlorophyll-a data we estimated the deep chlorophyll-a maximum (DCM) which was objectively interpolated onto a horizontal grid of $0.1^\circ \times 0.1^\circ$ with the above Gaussian function and considering planar mean field.

3.2.2 Inference of the geostrophic flow and the generalized omega equation

The geostrophic flow is estimated from the observed density field through thermal wind balance, imposing the ADCP velocity at the deeper depth of the density dataset (325 m). Then, we estimate the ageostrophic horizontal velocity as the difference between the total (ADCP) horizontal velocity and the geostrophic velocity, $\mathbf{u}_h^a = \mathbf{u}_h - \mathbf{u}^g$, where the superscript g denotes geostrophy, a denotes ageostrophy, and $\mathbf{u}_h$ is the total horizontal velocity (Thomas et al., 2010).

The adiabatic generalized omega equation used in this study is the **Q** vector form (Pallàs-Sanz and Viúdez, 2005)

$$N^2 \boldsymbol{\nabla}_h^2 w + f(f+\zeta) w_{zz} = \underbrace{2\boldsymbol{\nabla}_h \cdot \mathbf{Q}_h}_{S_{DEF}} + \underbrace{f\zeta_{ph}^a \cdot \boldsymbol{\nabla}_h^2 \mathbf{u}_h}_{S_{ADV}}, \tag{3.1}$$

where $f = 2\Omega \sin\varphi$ is the Coriolis parameter (considered constant and computed at the mean latitude φ), with Ω representing the Earth's angular velocity (f = 6.4 $\times$ 10^{-5} s^{-1}); $N^2 = -g\alpha_0\rho_z$ is the Brunt-Väisälä frequency where $\alpha_0 = \rho_0^{-1}$ is the mean specific volume, g is gravity, ρ is the density, and subscript z indicates a vertical derivative. Vertical relative vorticity is estimated as $\zeta = v_x - u_y$, where u and v are the zonal and meridional currents and x and y subscripts represent partial derivatives in the eastward and northward directions. The horizontal pseudovorticity vector is an anticlockwise rotation of the vertical shear, $\zeta_{ph} = (-v_z, u_z)$, while $\zeta_{ph}^a = (-v_z^a, u_z^a)$ is the ageostrophic horizontal pseudovorticity vector. ζ_{ph}^a can be viewed as the anticlockwise rotation of the thermal wind imbalance as $\mathbf{TWI} = (fu_z^a, fv_z^a)$ and, hence, $f\zeta_{ph}^a = \mathbf{k} \times \mathbf{TWI}$ (Giordani et al., 2006). The **Q** vector represents the deformation of

the horizontal density gradient by the total horizontal velocity field, $\mathbf{Q} = \boldsymbol{\nabla}_h \mathbf{u}_h \cdot \boldsymbol{\nabla}_h b$, where $b = \rho g \alpha_0$ is the buoyancy.

The forcing terms of the generalized omega equation are on the right-hand side (rhs) of (3.1). S_{DEF} is related to the total deformation field and can be decomposed into its geostrophic and ageostrophic components ($S_{DEF} = S_{DEFG} + S_{DEFA}$). S_{ADV} is related to the vertical shear of the ageostrophic horizontal current through ζ^a_{ph}. Giordani et al. (2006) relate S_{ADV} with the stretching and reorientation of the pre-existing ζ^a_{ph} by the total horizontal current field. On the left hand side (lhs) of (3.1) an elliptic operator (if $f + \zeta \geq 0$) is applied to the vertical velocity (w). The resulting elliptic equation is solved with an iterative relaxation method and constrained by Dirichlet boundary conditions, that is, w=0.

In order to analyze the accuracy of the derived geostrophic field including the ADCP velocity at the reference level (325 m depth), we alternatively estimated the geostrophic field by using the method proposed by Rudnick (1996) based on the imposition of constraints such as the horizontally nondivergence of the velocity field. The derived ageostrophic horizontal velocity obtained subtracting the constrained geostrophic velocity to the ADCP velocity showed the same vertical shear as the field estimated through the thermal wind balance, being the magnitude smaller. The slight difference in magnitude between the estimated fields with each methodology only affects the S_{DEFG} and S_{DEFA} forcing terms.

3.2.3 Wind-induced vertical velocities

Wind-induced vertical motions arise from the force of the surface wind stress, $\boldsymbol{\tau} = (\tau^x, \tau^y, 0)$ (superscripts x and y denote eastward and northward components), through Ekman pumping. The wind speed field during the PUMP cruise is obtained from the Weather Research and Forecasting (WRF) Model (Skamarock et al., 2008). The surface wind stress, considering eddy-wind interaction, is estimated from the bulk formula:

$$\boldsymbol{\tau} = \rho_a C_D \mathbf{u}_{rel} |\mathbf{u}_{rel}|, \tag{3.2}$$

where ρ_a=1.3 kg m^{-3} is the air density, and C_D = 1.14 $\times$ 10^{-3} is a drag coefficient considered constant with wind velocities between 4 and 10 m s^{-1} (Large, 1979). The

relative wind speed is represented by $\mathbf{u}_{rel} = \mathbf{u}_a - \mathbf{u}_0$, where $\mathbf{u}_a$ is the surface wind at 10 m above the mean sea level, and $\mathbf{u}_0$ is the surface ocean velocity. Ekman transport due to eddy-wind interaction can be written as (Stern, 1965):

$$\mathbf{T}_E \simeq -\frac{\mathbf{k} \times \boldsymbol{\tau}}{\rho_0 (f + \zeta_0)}, \tag{3.3}$$

and the associated Ekman pumping is:

$$w_{Ep} = \boldsymbol{\nabla}_h \cdot \mathbf{T}_E = \frac{\mathbf{k}}{\rho_0 (f + \zeta_0)} \cdot \boldsymbol{\nabla}_h \times \boldsymbol{\tau} + \frac{\mathbf{k} \times \boldsymbol{\tau}}{\rho_0 (f + \zeta_0)^2} \cdot \boldsymbol{\nabla}_h (f + \zeta_0), \tag{3.4}$$

where ρ_0 is the mean density (1026.4 kg m^{-3}) and ζ_0 is the geostrophic vertical relative vorticity at the sea surface. The first term on the rhs of (3.4) is the linear Ekman pumping and it is related to the wind stress curl. The second term on the rhs of (3.4) is the nonlinear Ekman pumping which is proportional to the advection of absolute vorticity by the Ekman transport.

3.3 Results

3.3.1 Intrathermocline eddy structure

The PUMP eddy is an anticyclonic intrathermocline eddy characterized by a biconvex shape of the isopycnals with a doming (depression) of the upper (deeper) layers corresponding to the seasonal (main) pycnocline. At the time of the survey, the PUMP eddy was 4 months old with a vertical extension of 500 m and 46 km radius. The eddy had a subsurface dynamical core embedded between the seasonal and main pycnoclines (centered at 85 m depth) with maximum horizontal velocities of 0.5 m s^{-1}. The subsurface horizontal velocity maximum is consistent with the typical biconvex intrathermocline eddy shape through thermal wind balance. Within the dynamical core the extreme Rossby number, Ro=ζ/f, reaches -0.6. Hence, the PUMP eddy is moderately ageostrophic and the application of the QG approximation would neglect an important contribution of the ageostrophic horizontal motions, otherwise considered in the generalized omega equation used in this study. On the other hand, the eddy hydrographic core was located between 200 and 500 m

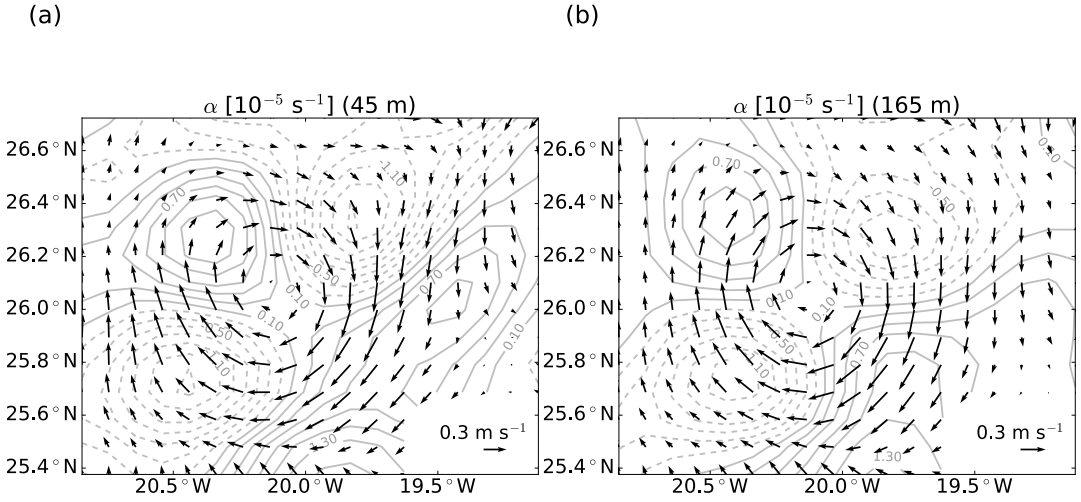

FIGURE 3.2: Horizontal distribution of the deformation field, α (10^{-5} s^{-1}), in grey contours at (a) 45 m and (b) 165 m depth. Solid contours represent diffluent flow ($\alpha > 0$) and dashed contours confluent flow ($\alpha < 0$). Vectors indicate the ADCP velocity.

depth and was characterized by warmer, saltier and lighter anomalies of temperature, salinity and density, respectively. A detailed description of the PUMP eddy is given by Barceló-Llull et al. (2017b).

Figure 3.2 shows the horizontal distribution of the deformation field ($\alpha = u_x - v_y$) at 45 m (domed seasonal pycnocline) and 165 m (depressed main pycnocline) with the ADCP velocity vectors superimposed. Alternating cells with confluent ($\alpha < 0$) and diffluent flows ($\alpha > 0$) are localized at the eddy periphery with maximum absolute values of $\sim 0.26f$. Confluent/diffluent flow creates propitious conditions for thermal wind imbalance (TWI) and, in consequence, ASC (Hoskins and Bretherton, 1972; Hoskins et al., 1978; Spall, 1997). From the horizontal distribution of α we expect ASC to arise at the eddy periphery.

3.3.2 Vertical velocity distribution and chlorophyll-a signature

Horizontal sections at different depths of the estimated vertical velocity within the PUMP eddy are shown in Fig. 3.3. In the upper layers, the vertical velocity distribution is characterized by small and weak upwelling ($w > 0$) and downwelling ($w < 0$) cells localized at the eddy periphery (Fig. 3.3a). Below 85 m depth, the horizontal

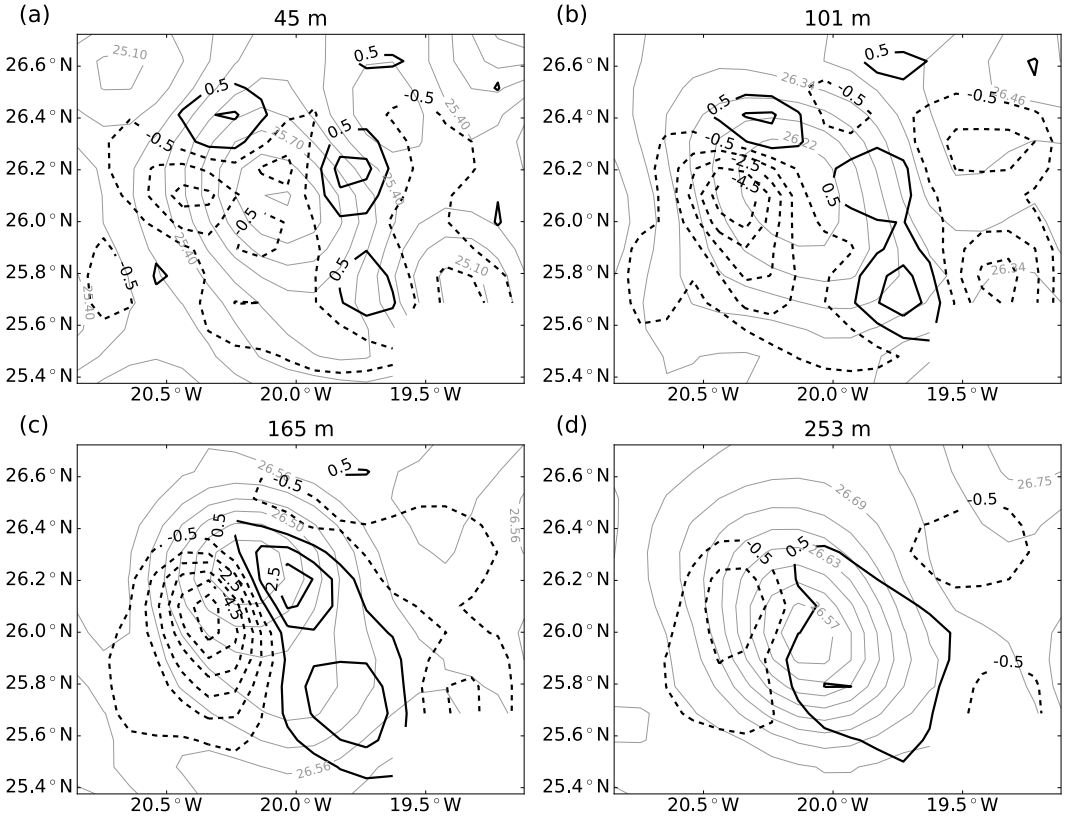

FIGURE 3.3: Mesoscale vertical velocity, w (m d^{-1}), in thick black contours (with a contour interval of 1 m d^{-1}) estimated from the generalized omega equation at different depths: (a) 45 m, (b) 101 m, (c) 165 m and (d) 253 m. Thin grey contours represent the potential density anomaly, σ_θ (kg m^{-3}), for reference.

distribution of w changes gradually to a dipolar pattern (Figs. 3.3b-d) with a downwelling (upwelling) cell on the western (eastern) edge of the anticyclonic eddy. At 165 m depth (Fig. 3.3c) the dipolar distribution of w reaches maxima of -6.3 m d^{-1} and 3.3 m d^{-1}. Figure 3.4 shows a vertical section of the vertical velocity along 26.1°N. At this zonal section the dipolar distribution of w extends from the surface to the deepest available data depth (325 m). The downwelling cell is broader and it is approximately two times larger than the upwelling cell. Maxima of w are located between 160 and 185 m depth .

Within the PUMP eddy, the vertical velocity extrema are located along the eddy periphery over the whole water column, while in the eddy center the vertical motions are negligible. In order to validate this result, Fig. 3.5 shows the DCM distribution. Along the eddy periphery the DCM has maximum values ranging from 0.36 to 0.41 mg m^{-3}, while at the eddy center the minima reach 0.30 mg m^{-3} and are

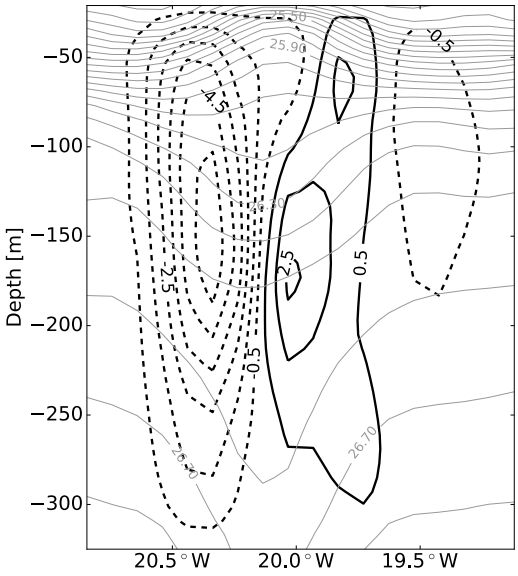

FIGURE 3.4: (a) Vertical section along 26.1°N of the mesoscale vertical velocity, w (m d^{-1}), in thick black contours (with a contour interval of 1 m d^{-1}) estimated from the generalized omega equation. Thin grey contours represent the potential density anomaly, σ_θ, with a contour interval of 0.1 kg m^{-3} for reference.

similar to the minima of the outer region. Hence, the DCM distribution is annular with relative minima at the eddy center and outside the eddy.

3.3.3 Sources of vertical velocity

A detailed analysis of the sources of vertical velocity within the PUMP eddy is performed through the integration of equation (3.1) with each individual forcing term (Pallàs-Sanz et al., 2010b). With this procedure we obtain the contribution of the deformation field, w_{DEF}, the contribution of the pseudovorticity term, w_{ADV} and, with the decomposition of the deformation $\mathbf{Q}$ vector in its geostrophic and ageostrophic counterparts, we obtain w_{DEFG} and w_{DEFA}, respectively. Consequently, $w = w_{DEF} + w_{ADV}$ and $w_{DEF} = w_{DEFG} + w_{DEFA}$.

Figure 3.6 shows the horizontal average of the absolute value of the total vertical velocity, $\langle|w|\rangle_H$ (thick black line), $\langle|w_{DEF}|\rangle_H$ and $\langle|w_{ADV}|\rangle_H$ (thin black lines), and $\langle|w_{DEFG}|\rangle_H$ and $\langle|w_{DEFA}|\rangle_H$ (thin grey lines). $\langle|w|\rangle_H$ has a subsurface maximum located at 85 m depth corresponding to the eddy dynamical core, and a deeper maximum located at 150 m depth corresponding to the upper boundary of the eddy

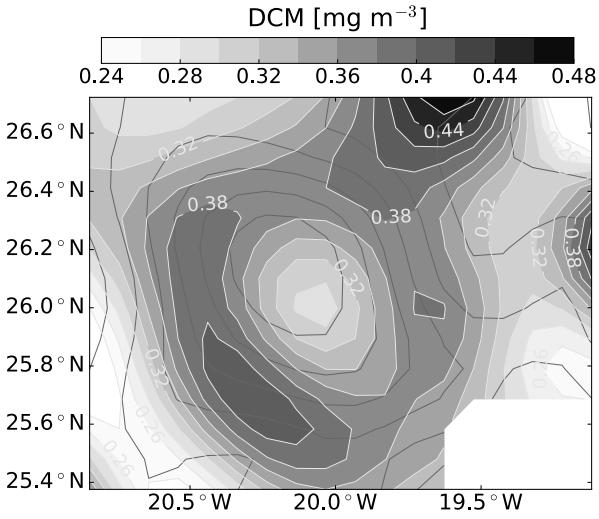

FIGURE 3.5: Deep chlorophyll maximum (DCM) objectively interpolated with a correlation scale of 40 km. Black contours represent the potential density anomaly, σ_θ, at 101 m depth for reference.

hydrographic core. These local maxima are related to maxima in the vertical shear of the ageostrophic horizontal velocity (Barceló-Llull et al., 2017b) and, in consequence, they are related to the S_{ADV} forcing term through the ageostrophic horizontal pseudovorticity vector. The deformation and pseudovorticity contributions are, however, similarly important throughout the water column, with a slight dominance of w_{ADV} (w_{DEF}) in the upper (below) 200 m depth. On the other hand, w_{DEF} is mainly driven by its geostrophic component w_{DEFG}, while the ageostrophic component w_{DEFA} has its maximum at the base of the Ekman layer (δ_E = 32 m, see Section 3.3d) and is almost constant throughout the water column.

Horizontal sections of the contributions of vertical velocity are shown in Figs. 3.7 and 3.8. The contributions w_{DEF} and w_{ADV} at 45 m depth (seasonal pycnocline) have similar magnitudes but different horizontal distributions (Figs. 3.6, 3.7a and b). While w_{DEF} is characterized by small alternating upwelling and downwelling cells located at the eddy periphery, w_{ADV} has a dipolar distribution with a downwelling (upwelling) cell at the northwestern (eastern) edge of the PUMP eddy. Both w_{DEF} and w_{ADV} contributions give rise to the total vertical velocity distribution at 45 m depth (Fig. 3.3a). At 165 m depth (main pycnocline), w_{DEF} and w_{ADV} have slightly different orders of magnitude (Figs. 3.6, 3.8a and b). Maxima w_{DEF} of -2.2 m d^{-1}

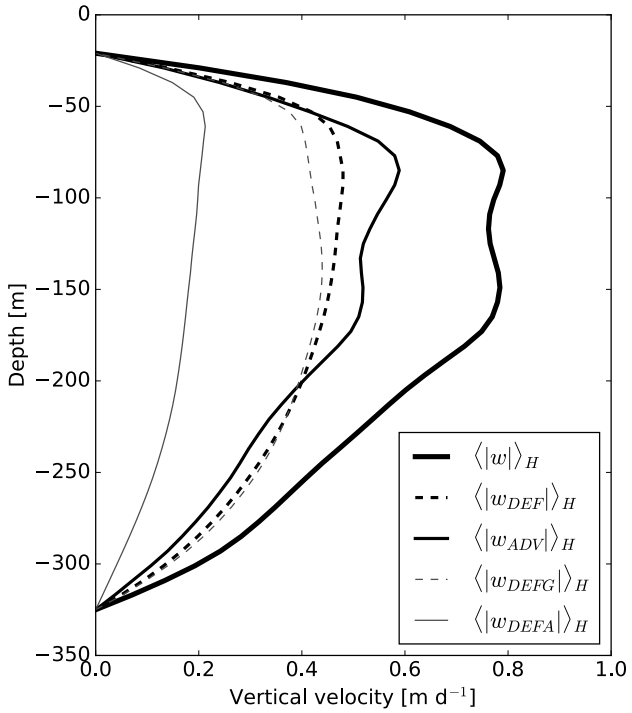

FIGURE 3.6: Horizontal average of the absolute value of the vertical velocity estimated with each individual forcing term in equation (3.1), with the sum S_{DEF} + S_{ADV}, and with S_{DEFG} and S_{DEFA}.

and 2.5 m d^{-1} occur at the downwelling/upwelling cells located along the eddy periphery, while w_{ADV} extremum of -4.1 m d^{-1} is located at the western downwelling cell; the weaker eastern upwelling cell has maximum of 2.1 m d^{-1}. The w_{DEF} contribution is characterized by a quadripolar distribution, while w_{ADV} is characterized by an asymmetric dipolar pattern. Both vertical velocities contribute to the total vertical velocity distribution (Fig. 3.3c) characterized by a dipolar pattern with an intensified western downwelling cell and a broader eastern upwelling cell.

Although w_{DEF} and w_{ADV} have similar magnitudes over the whole water column and make similar contributions to the w distribution, w_{DEF} is mainly forced by its geostrophic component, w_{DEFG}, as can be seen in Figs. 3.6, 3.7, and 3.8. The w_{DEFG} contribution estimated with the constrained geostrophic velocity obtained using the Rudnick (1996) method shows the same multipolar and quadripolar distributions with a negligible difference in shape and the same magnitude (not shown). Hence, the w distribution within the PUMP eddy is mainly driven by both w_{DEFG} and w_{ADV}.

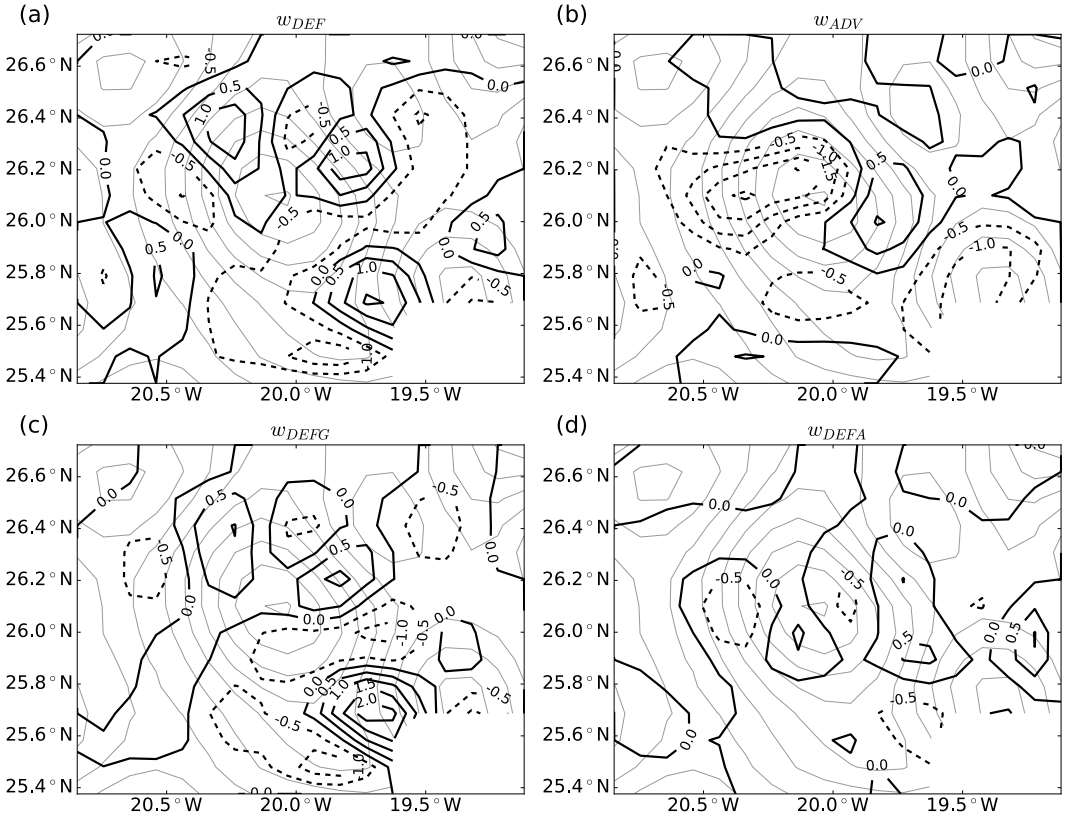

FIGURE 3.7: Mesoscale vertical velocity, w (m d^{-1}), in thick black contours (with a contour interval of 0.5 m d^{-1}) estimated with each individual forcing term in equation (3.1) at 45 m depth. Grey contours represent the potential density anomaly, σ_θ, for reference.

3.3.4 Ekman pumping

Eddy-wind induced Ekman pumping is derived following Stern (1965), and the wind stress is parameterized considering the eddy surface currents (Section 3.2.3). The wind stress computed from the bulk formula (3.2) has a spatially averaged value of 2.8 $\times$ 10^{-2} N m^{-2}. Using this value, the Ekman layer depth is $\delta_E \simeq 0.4u^*/f$ = 32 m, where the frictional velocity is obtained from $u^* = \sqrt{|\boldsymbol{\tau}|/\rho_0}$ = 5 $\times$ 10^{-3} m s^{-1} (Pallàs-Sanz et al., 2010a). Figure 3.9a shows the spatial distribution of the (scaled) geostrophic vertical relative vorticity at 21 m depth (ζ_0/f), which is the shallowest depth available, with the wind stress superimposed. ζ_0 has minimum values at the eddy center of -0.34f and a positive vorticity ($\zeta_0 > 0$) belt surrounding it. The direction of the wind stress is defined by the direction of the Trade winds. The resulting Ekman transport is directed 90° clockwise to the wind stress direction.

The total Ekman pumping (w_{Ep}) and its linear and nonlinear components are

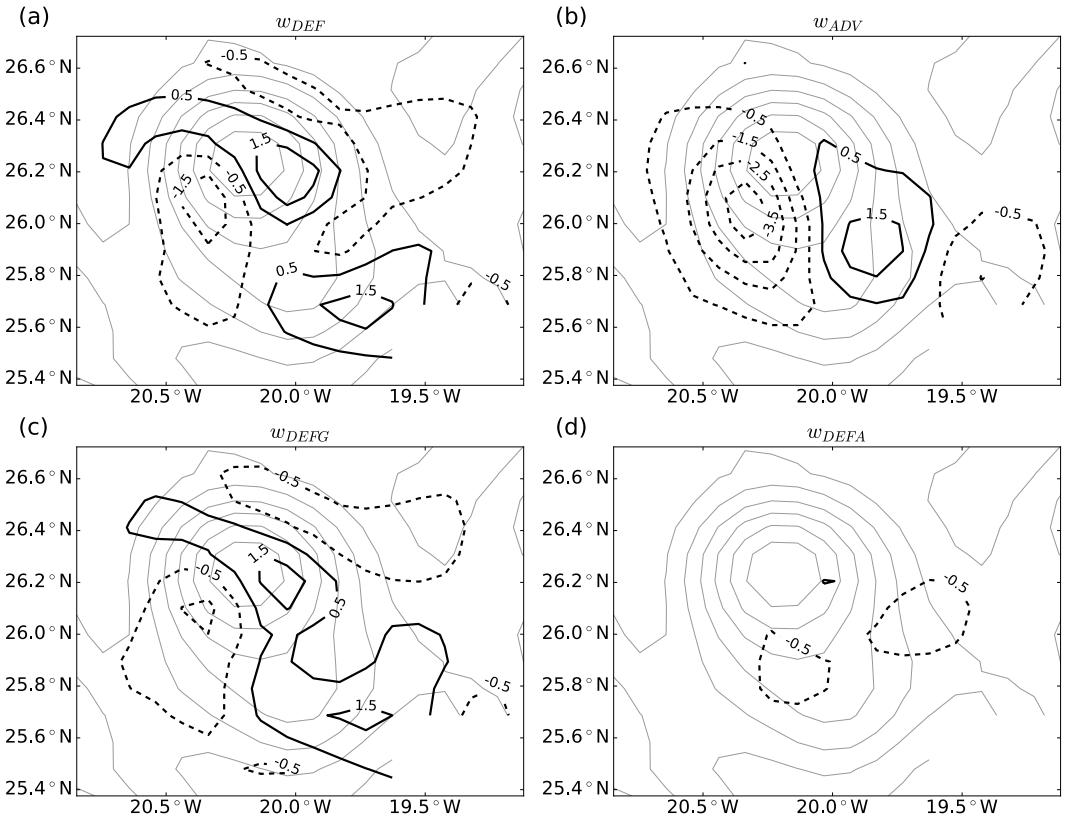

FIGURE 3.8: Mesoscale vertical velocity, w (m d^{-1}), in thick black contours (with a contour interval of 1 m d^{-1}) estimated with each individual forcing term in equation (3.1) at 165 m depth. Grey contours represent the potential density anomaly, σ_θ, for reference.

shown in Fig. 3.9. The wind stress curl was small during the sampling of the PUMP eddy. As a consequence, the linear Ekman pumping in the PUMP eddy (Fig. 3.9c) has small values of 0.1 m d^{-1} at the eddy center, a magnitude smaller than the inferred vertical velocity using the omega equation. On the other hand, nonlinear Ekman pumping (Fig. 3.9d) has higher maximum values of 0.5 m d^{-1} and a dipolar distribution centered at the eddy core and oriented along the direction of the Ekman transport, that is, $w < 0$ ($w > 0$) at the western (eastern) edge of the eddy. The resulting (total) Ekman pumping (Fig. 3.9b) has a dipolar distribution driven by the nonlinear component and reaches values of -0.7 m d^{-1} and 0.5 m d^{-1} at the eddy periphery.

Ekman model provides an estimate of the vertical velocity at the base of the Ekman layer driven by the interaction between wind and ocean surface currents. This interaction is a diabatic process driven by turbulent momentum fluxes. To compare

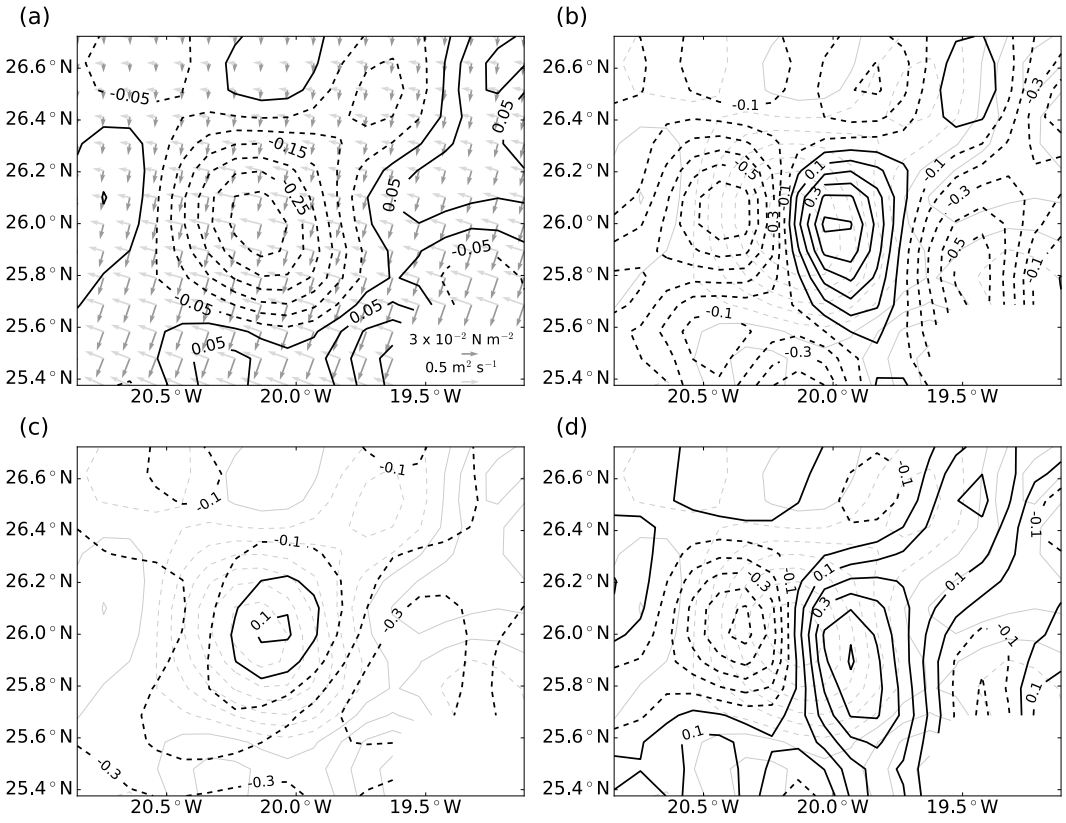

FIGURE 3.9: (a) Scaled geostrophic relative vorticity at the sea surface (21 m), ζ_0/f, in black contours. Wind stress assuming eddy-wind interaction, $\boldsymbol{\tau}$, is represented by dark grey arrows while light grey arrows indicate Ekman transport, $\mathbf{T}_E$. (b) Vertical motion (m d^{-1}) due to Ekman pumping, w_{Ep}, and due to its linear (c) and nonlinear (d) components. In (b), (c) and (d) scaled geostrophic relative vorticity contours are plotted in light grey for reference.

the estimated Ekman pumping with the vertical velocity field derived by resolving equation (3.1), we have also integrated the diabatic version of the generalized omega equation proposed by Pallàs-Sanz et al. (2010b), in which an additional forcing term related with the parameterized transfer of momentum is included. The vertical eddy viscosity is parameterized with a mixed layer depth (MLD) profile (Nagai et al., 2006). The vertical velocity field inferred through the diabatic version of the generalized omega equation has the same distribution inside the eddy region than the adiabatically derived vertical velocity, while an enhancement of w is found outside the eddy periphery where the MLD is deeper (not shown). On the other hand, the wind effects may also contribute significantly to the ageostrophic vertical shear used to construct S_{ADV}. Hence, a comparison of the Ekman pumping with the

vertical velocity induced by the S_{ADV} forcing term is justified. Indeed, if we compare the total Ekman pumping distribution (Fig. 3.9b) with the w_{ADV} distribution at 45 m depth (Fig. 3.7b) we observe a similar dipolar pattern that is slightly rotated but with similar magnitude.

3.3.5 Horizontal ageostrophic secondary circulation

Figure 3.10a shows a vertical section along 26.1°N of the ASC zonal and vertical components (u^a, w). In the seasonal pycnocline, u^a is mainly directed westward and has maximum values of the order of 0.1 m s^{-1} located at the eddy periphery where the horizontal gradients of σ_θ are larger. In the deeper layers (between 175 and 265 m depth), u^a is directed to the east and advects flow from the downwelling cell to the upwelling cell to conserve mass in incompressible flow. Therefore, a cyclonic cell of ASC develops within the anticyclonic eddy.

The horizontal flow in the PUMP eddy is, on average, supergeostrophic as $|\mathbf{u}_h| > |\mathbf{u}^g|$ (Barceló-Llull et al., 2017b). Figure 3.10b shows the horizontal distribution of the horizontal ASC, $\mathbf{u}_h^a$, at 165 m depth, which is characterized by an anticyclonic circulation reaching maximum values of ∼0.07 m s^{-1} at the eddy periphery. Horizontal ASC can be written using the inviscid horizontal momentum equation,

$$\frac{D\mathbf{u}_h}{Dt} + f\mathbf{k} \times \mathbf{u}_h^a = 0 \tag{3.5}$$

as (e.g. Pallàs-Sanz and Viúdez, 2007):

$$\mathbf{u}_h^a = \frac{1}{f}\mathbf{k} \times \frac{D\mathbf{u}_h}{Dt} = \frac{1}{f}\mathbf{k} \times (\frac{\partial \mathbf{u}_h}{\partial t} + \mathbf{u}_h \cdot \boldsymbol{\nabla}_h \mathbf{u}_h + w\frac{\partial \mathbf{u}_h}{\partial z}). \tag{3.6}$$

Hence, in accordance with equation (3.6), the horizontal ASC can be interpreted as an anticlockwise rotation of the material rate of change of the (total) horizontal velocity. With the PUMP eddy dataset, that is, only one realization, we are not able to estimate the local temporal rate of change of the horizontal velocity. On the other hand, within the PUMP eddy the horizontal advective acceleration is two orders of magnitude higher than the vertical advective acceleration (not shown). Figure 3.10c shows the horizontal distribution of this term scaled by the planetary vorticity, f, at

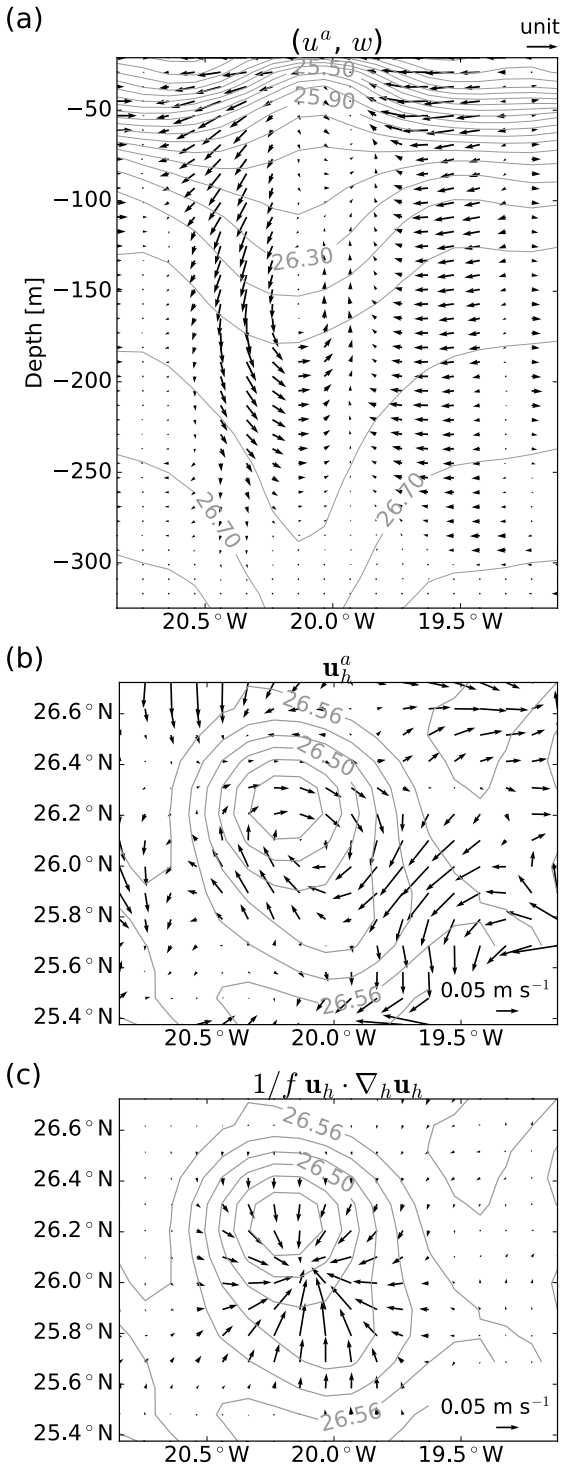

FIGURE 3.10: (a) Vertical section along 26.1°N of the ageostrophic zonal velocity, u^a, and w. An arrow unit on the map corresponds with 0.1 m s^{-1} for the zonal component u^a and 1×10^{-4} m s^{-1} for the vertical component w. (b) Horizontal map of the horizontal ASC at 165 m depth. (c) Horizontal distribution of $\frac{1}{f}\ \mathbf{u}_h \cdot \boldsymbol{\nabla}_h \mathbf{u}_h$ at 165 m depth. Grey contours represent the potential density anomaly, σ_θ, with a contour interval of 0.1 kg m^{-3} in (a).

165 m depth. It points to the eddy center and has orders of magnitude of 0.05 m s^{-1}. Hence, its anticlockwise rotation agrees with the direction and magnitude of the horizontal ASC (Fig. 3.10b) within the eddy core. Therefore, the horizontal advective acceleration within the PUMP eddy, $\mathbf{u}_h \cdot \boldsymbol{\nabla}_h \mathbf{u}_h$, is the most important contribution to the horizontal ASC.

The horizontal advective acceleration in the ($\mathbf{s} = \mathbf{u}_h/|\mathbf{u}_h|$, $\mathbf{n} = \mathbf{k} \times \mathbf{s}$) reference frame can be decomposed into two components,

$$\mathbf{u}_h \cdot \boldsymbol{\nabla}_h \mathbf{u}_h = \frac{\delta}{\delta s}(\frac{u^2}{2})\mathbf{s} + u^2 \kappa \mathbf{n}, \tag{3.7}$$

where κ is the streamline curvature and $\delta/\delta s$ is the directional derivative along $\mathbf{s}$ (Pallàs-Sanz and Viúdez, 2007). The first term on the rhs of (3.7) is the speed acceleration and the second term is the centripetal acceleration. As the horizontal advective acceleration clearly points to the eddy center (Fig. 3.10c), it is strongly suggested that the centripetal acceleration dominates the distribution. As a conclusion, horizontal ASC within the PUMP eddy is mainly driven by the centripetal acceleration.

3.3.6 Interpretation of the sources of ASC

The forcing term S_{DEF} can be decomposed into two components:

$$S_{DEF} = 2\boldsymbol{\nabla}_h \cdot \mathbf{Q}_h = 2\boldsymbol{\nabla}_h \cdot (\boldsymbol{\nabla}_h \mathbf{u}_h \cdot \boldsymbol{\nabla}_h b) = 2\boldsymbol{\nabla}_h^2 \mathbf{u}_h \cdot \boldsymbol{\nabla}_h b + 2\boldsymbol{\nabla}_h \mathbf{u}_h : \boldsymbol{\nabla}_h(\boldsymbol{\nabla}_h b),$$

and, using the thermal wind balance relation, $\boldsymbol{\nabla}_h b = \mathbf{k} \times \mathbf{u}_z^g$, and the approximation $\boldsymbol{\nabla}_h^2 \mathbf{u}_h \approx \mathbf{k} \times \boldsymbol{\nabla}_h \zeta$ (Pallàs-Sanz and Viúdez, 2005) S_{DEF} can be written as:

$$S_{DEF} \approx 2f(\mathbf{k}\times\boldsymbol{\nabla}_h\zeta)\cdot(\mathbf{k}\times\mathbf{u}_z^g)+2\boldsymbol{\nabla}_h\mathbf{u}_h : \boldsymbol{\nabla}_h(\boldsymbol{\nabla}_h b) = 2f\mathbf{u}_z^g\cdot\boldsymbol{\nabla}_h\zeta+2\boldsymbol{\nabla}_h\mathbf{u}_h : \boldsymbol{\nabla}_h(\boldsymbol{\nabla}_h b).$$

The first term is the horizontal advection of vertical relative vorticity by the geostrophic vertical shear, and the second term is related to a correlation between spatial changes of $\mathbf{u}_h$ and $\boldsymbol{\nabla}_h b$. A scale analysis of these two components shows similar orders of magnitude and, hence, both terms contribute to the S_{DEF} forcing term. On the other hand, S_{ADV} can be approximated as the horizontal advection of

vertical relative vorticity by the ageostrophic vertical shear,

$$S_{ADV} = f\zeta^a_{ph} \cdot \boldsymbol{\nabla}^2_h \mathbf{u}_h \approx f(\mathbf{k} \times \mathbf{u}^a_{hz}) \cdot (\mathbf{k} \times \boldsymbol{\nabla}_h \zeta) \approx f\mathbf{u}^a_{hz} \cdot \boldsymbol{\nabla}_h \zeta.$$

A comparison of the magnitudes of S_{DEF} and S_{ADV} forcing terms reveals the dominance of S_{ADV} ($S_{DEF}/S_{ADV} \sim 0.4$):

$$f\mathbf{u}^a_{hz} \cdot \boldsymbol{\nabla}_h \zeta > 2f\mathbf{u}^g_z \cdot \boldsymbol{\nabla}_h \zeta + 2\boldsymbol{\nabla}_h \mathbf{u}_h : \boldsymbol{\nabla}_h(\boldsymbol{\nabla}_h b).$$

Hence, the sources of vertical motion are mainly driven by the horizontal advection of vertical relative vorticity by the ageostrophic vertical shear, $f\mathbf{u}^a_{hz} \cdot \boldsymbol{\nabla}_h \zeta$. The importance of including this term in the omega equation was already demonstrated by Viúdez and Dritschel (2004). Pallàs-Sanz and Viúdez (2005) found that the most important forcing term was the horizontal advection of vertical relative vorticity by the total vertical shear. We demonstrate that, for the PUMP eddy, the advection is mainly due to ageostrophic vertical shear.

The horizontal ASC within the PUMP eddy is anticyclonic ($|\mathbf{u}_h| = |\mathbf{u}^a_h + \mathbf{u}^g| > |\mathbf{u}^g|$) and mainly driven by horizontal advective acceleration which, in turn, is dominated by the centripetal acceleration of the flow. The former methodology to estimate the horizontal ageostrophic velocity from the residual of the total (ADCP) horizontal velocity and the geostrophic velocity carries some uncertainty associated with the computation of the geostrophic velocity using thermal wind balance. For the PUMP dataset, the anticlockwise rotation of the horizontal advective acceleration within the PUMP eddy core agrees well with the diagnosed horizontal ASC. Hence, the results suggest that this method of obtaining the horizontal ASC from centripetal acceleration is viable but does depend on the quality of the ADCP measurements.

3.3.7 Total vertical fluxes

The vertical heat flux is defined as $T'w'$, where $T' = T - \langle T \rangle_H$, $w' = w - \langle w \rangle_H$ and $\langle\rangle_H$ represents the horizontal average within the eddy core. In the same way, the vertical potential vorticity (Π) flux is expressed as $\Pi' w'$. Vertical profiles of the horizontal averages of both fluxes are shown in Fig. 3.11. The $\langle T'w' \rangle_H$ has negative values

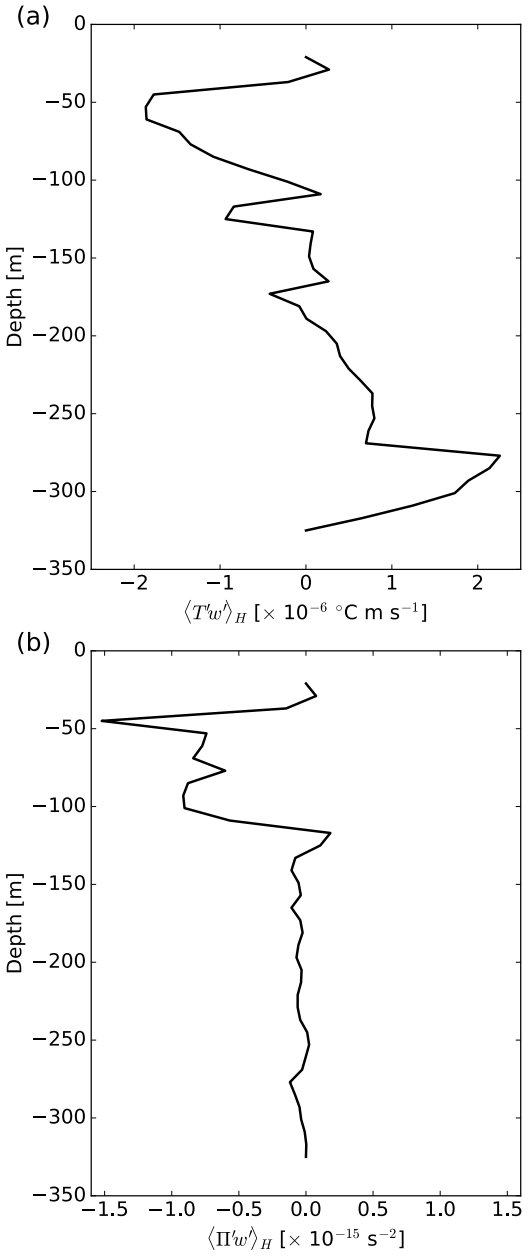

FIGURE 3.11: Horizontally averaged (a) vertical heat flux, $\langle T'w' \rangle_H$, and (b) vertical potential vorticity flux, $\langle \Pi'w' \rangle_H$, as a function of depth.

between the surface and 100 m depth, indicating that vertical motions act to cool the upper layers. On the other hand, below 200 m depth the horizontally averaged vertical heat flux has positive values, indicating that the vertical velocity is warming the deeper layers. The vertical profile of the horizontal average of the Π flux has negative values in the upper 100 m and is nearly zero below. This indicates a loss of Π in the upper layers. The intrathermocline eddy temperature anomaly field is characterized by a cold cap within the seasonal pycnocline and a deeper warm core

between 200 and 500 m depth, while the Π anomaly field is characterized by negative values in the seasonal pycnocline (Barceló-Llull et al., 2017b). These results suggest that vertical velocity contributes to the maintenance of the typical characteristics of the intrathermocline eddy.

3.4 Discussion

The vertical velocity distribution within the intrathermocline eddy is mainly characterized by extreme values at the eddy periphery, while at the eddy center vertical motions are negligible (Figs. 3.3 and 3.4). The DCM distribution reveals higher concentration of chlorophyll-a at the eddy periphery, while at the eddy center the concentration is minimum with values similar to those outside the eddy region (Fig. 3.5). Annular ring-shaped patterns of CHL have been observed around anticyclones in different regions of the global ocean from satellite data (McGillicuddy, 2016): Mizobata et al. (2002) in the Bering Sea, Kahru et al. (2007) in the Southern Ocean, and José et al. (2014) in the Mozambique Channel. To explain this eddy boundary enhancement, two mechanisms have been proposed: lateral entrainment and local enhancement (McGillicuddy, 2016). Our results suggest that the higher chlorophyll-a concentration around the PUMP eddy may be due to the deeper upwelling cell (Figs. 3.3c and 3.4) which would introduce nutrients to the euphotic layer, while in the upper layers the small upwelling cells would redistribute the nutrients within the euphotic layer. The time expected for biological removal of the introduced nutrients is quicker than that of the vertical velocity supply/subduction (McGillicuddy et al., 1998; Mahadevan et al., 2008). Hence, the upwelled nutrients would be rapidly assimilated by phytoplankton around the eddy periphery and distributed by the horizontal flow that is several orders of magnitude larger than the vertical motions.

Several dynamical mechanisms have been proposed to explain the physical processes responsible for creating the observed biological patterns within mesoscale eddies. According to the eddy pumping mechanism, the doming of the seasonal pycnocline would induce an input of nutrients and high chlorophyll-a concentrations within the cores of intrathermocline eddies. This enhancement has been observed in the Sargasso Sea (McGillicuddy et al., 1998), but it is not the case for the PUMP eddy

(Fig. 3.5). On the other hand, linear Ekman pumping, which predicts a monopole of positive vertical velocities within anticyclonic eddies (Martin and Richards, 2001), has been computed for the PUMP eddy and is weaker than the nonlinear contribution to the eddy-wind interaction (Figs. 3.9c, d). The nonlinear Ekman pumping within the PUMP eddy induces a dipolar distribution of w with maximum values of $\pm$ 0.5 m d^{-1} at the base of the Ekman layer, located at 32 m. Hence, the nonlinear Ekman pumping has to be compared with the horizontal distribution of the diagnosed w in the upper layers (Fig. 3.3a). Its multipolar structure differs from the nonlinear Ekman pumping dipolar pattern; nevertheless, the w_{ADV} contribution within the seasonal pycnocline (Fig. 3.7b) is also characterized by a dipolar pattern with similar maximum values. Hence, the w distribution in the upper layers may be partly explained by nonlinear Ekman pumping. On the other hand, the w_{DEF} contribution in the upper layers (Fig. 3.7a) is characterized by an octopolar pattern with alternating upwelling/downwelling cells. Buongiorno Nardelli (2013) proposed vortex Rossby waves as a possible mechanism for modulating the vertical velocity field within mesoscale eddies. Although this hypothesis is difficult to demonstrate, w_{DEF} shows an azimuthal wavelike distribution with a wavenumber of 4.

The w_{ADV} contribution within the depressed main pycnocline has a dipolar structure (Fig. 3.8b) with a broader and intenser downwelling cell in the west and a weaker upwelling cell in the east. The nonnegligible ageostrophic horizontal velocity over the whole water column (Fig. 3.10) suggests the possibility of deep wind influence. On the other hand, w_{DEF} has a quadripolar structure (Fig. 3.8a) already predicted by Viúdez and Dritschel (2003) with a primitive equation model. The w dipolar structure within an intrathermocline eddy was first seen south of Fuerteventura by Benítez-Barrios et al. (2011) from low-resolution *in situ* data.

3.5 Conclusions

For the first time we have estimated the ASC within an anticyclonic intrathermocline eddy from high-resolution quasi-synoptical 3D observational data. The intrathermocline eddy is characterized by two different horizontal distributions of w. In the seasonal pycnocline, the w distribution is characterized by alternating upwelling and downwelling cells located at the eddy periphery. Below 85 m depth (main pycnocline) the w distribution changes gradually in depth toward a dipolar pattern with a downwelling cell on the western edge of the eddy and an upwelling cell on the eastern edge of the eddy. Maximum values of w of -6.4 m d^{-1} and 3.4 m d^{-1} are located between 160 and 185 m depth. A similar w magnitude was found by Benítez-Barrios et al. (2011) within an intrathermocline eddy south of Fuerteventura island. In the upper layers, the w multipolar distribution may be the result of a combination of nonlinear Ekman pumping with modulation by vortex Rossby waves, although the latter is difficult to demonstrate with the available data (Buongiorno Nardelli, 2013). The deeper w dipolar distribution suggests the possibility of a deep wind influence through relatively intense ageostrophic vertical shear. The w_{DEF} contribution in the deeper layers has a quadripolar distribution already predicted by theoretical models (Viúdez and Dritschel, 2003). The interaction of both contributions, w_{DEF} and w_{ADV}, gives rise the final w dipolar distribution already detected from low-resolution data by Benítez-Barrios et al. (2011) in the region of study. The w_{DEF} contribution in the whole water column is mainly dominated by its geostrophic counterpart; hence, the w distribution within the PUMP eddy is mainly driven by both w_{DEFG} and w_{ADV}. These contributions can be interpreted respectively as the horizontal deformation of the density field by the geostrophic velocity and the advection of vertical relative vorticity by the ageostrophic vertical shear.

Our observations from *in situ* data reveal that a typical intrathermocline eddy under typical atmospheric forcing enhances chlorophyll-a concentration, and this enhancement occurs at the eddy periphery instead of at the eddy center. This coincides with the occurrence of upwelling cells along the eddy periphery that may bring nutrients to the euphotic layer. Our analysis suggests that part of these cells may be result of eddy-wind interaction through nonlinear Ekman pumping, but also

other processes may be at work, such as the plausible occurrence of vortex Rossby waves.

The horizontal ageostrophic velocity acts to close the dipolar vertical velocity distribution within the intrathermocline eddy. The anticyclonic horizontal ASC is proportional to the anticlockwise rotation of the horizontal advective acceleration, which is mainly dominated by the centripetal acceleration. Vertical velocities maintain the intrathermocline eddy structure through fluxes of heat and potential vorticity. The vertical velocity acts to cool the upper layers and warm the deeper layers, while contributing to a loss of potential vorticity in the seasonal pycnocline.

Though more experimental studies are needed to corroborate the generality of these results, we conclude that the dipolar distribution of mesoscale vertical velocity in the PUMP eddy is robust and may be ubiquitous in wind-forced and elliptically shaped anticyclonic intrathermocline eddies in the Canary Eddy Corridor. This result contrasts with the quadripolar distribution of w expected in an f-plane and non-forced numerical elliptical anticyclone (Viúdez and Dritschel, 2003). The reasons for this difference between theory and observations are expected to be a source of future work.

Chapter 4

Validation of a multivariate global ocean state estimate with high-resolution *in situ* data

Barceló-Llull, B., Pascual, A., Mason, E., and Mulet, S. Validation of a multivariate global ocean state estimate with high-resolution *in situ* data, in prep.

Abstract

Validation of the new products developed in operational oceanography is of fundamental importance in order to provide high quality data management procedures. A multivariate global ocean state estimate (ARMOR3D), which merges remote sensing observations with *in situ* vertical profiles of temperature and salinity, is validated here with independent high-resolution *in situ* observations. Apart from the validation of the hydrography, it is performed a validation of derived variables such as the quasi-geostrophic (QG) vertical velocity. The final objective of this study is to assess the ability of the reanalysis technique to describe the three-dimensional (3D) hydrography and dynamics of mesoscale eddies. *In situ* CTD and horizontal current observations are obtained from an oceanographic cruise near the Canary Islands in the northeast Atlantic ocean. An anticyclonic intrathermocline eddy was intensively sampled using CTDs, acoustic Doppler current profiler (ADCP), microstructure turbulence profiler, water samples and buoys. Comparison between these data and contemporaneous ARMOR3D data is done over (i) a high-resolution meridional

transect crossing the eddy center and (ii) a 3D grid centered on the eddy center and covering the eddy region. The ARMOR3D product is able to reproduce the hydrographic vertical structure of the independently sampled eddy below the upper seasonal thermocline. ARMOR3D density fields also show the observed elliptical eddy shape, with the major axis oriented NW-SE, and a deceleration of the flow at the northern edge of the eddy. The ARMOR3D geostrophic flow is surface intensified and underestimated by a factor of 2, which implies an underestimation of the Rossby number by a factor of 3. High correlation coefficients are obtained for the density, geostrophic velocity and Rossby number fields within the eddy region. Despite the underestimation, inferred quasi-geostrophic (QG) vertical velocity patterns have the same multipolar distribution observed in the *in situ*-derived QG vertical velocity. The QG vertical velocity is characterized by an octopolar pattern with the magnitude underestimated by a factor of 3 to 4.

4.1 Introduction

Advancement in our knowledge of the ocean depends profoundly on high quality three-dimensional (3D) observations of the global ocean. However, *in situ* oceanographic sampling strategies only cover specific regions of the ocean during short periods of time, providing knowledge of specific oceanographic features. Moreover, synopticity is a key factor in the *in situ* sampling of the ocean, partly solved by satellites which are able to sample the globe in a short period of time. Despite the global coverage of the remote sensing observations, they only provide a surface view of the ocean. In order to complement satellite observations, the ARGO project yields real-time *in situ* vertical profiles of temperature and salinity in a global, but sparse, grid.

In order to take advantage of the global coverage of remote sensing observations and the available *in situ* vertical profiles of temperature and salinity, Guinehut et al. (2012) achieved the first attempt to merge remote sensing observations (sea level anomaly, SLA, and sea surface temperature, SST) with *in situ* temperature and salinity vertical profiles (XBTs, CTDs, moorings and ARGO profiles) to empirically infer

3D upper-ocean structure. This multivariate observation-based product, named ARMOR3D, provides global 3D data sets of temperature and salinity on a $1/4^o$ Mercator horizontal grid with weekly temporal resolution. The period available is from 1998 to 2009 and the product is freely available.

Several studies have taken advantage of the ability of this innovative product to analyze mesoscale dynamics. Buongiorno Nardelli et al. (2012) carried out the first attempt to apply the quasi-geostrophic (QG) approximation to the observation-based product in order to map 3D mesoscale dynamics. Pascual et al. (2015) and Barceló-Llull et al. (2016) derive the QG mesoscale vertical velocity from the ARMOR3D fields in order to analyze its distribution in different regions of the global ocean as well as its contribution to nutrient advection and phytoplankton growth. On the other hand, Mason et al. (2017) construct eddy-centric composites of tracers, geostrophic currents and QG vertical velocity diagnosed from ARMOR3D in the energetic Brazil-Malvinas Confluence region. Through subregional composites they are able to reveal and analyze mesoscale eddy heterogeneity.

Besides the growing capacities of the new products developed in operational oceanography (Schiller and Brassington, 2011; Bell et al., 2015; Chakraborty et al., 2015; Le Traon et al., 2015; Hernandez et al., 2015; Kaurkin et al., 2016; Sotillo et al., 2016), the validation of these products with high-resolution *in situ* data is of fundamental importance in order to provide high quality data management procedures. The objective of the present study is to validate the innovative ARMOR3D product with high-resolution *in situ* CTD and horizontal current observations obtained from the intensively sampling of an anticyclonic intrathermocline eddy inside the Canary Eddy Corridor in the northeast Atlantic (Sangrà et al., 2009; Barceló-Llull et al., 2017b). Apart from the validation of the hydrographic structure, we also validate derived variables such as the QG vertical velocity that has previously been computed and analyzed from ARMOR3D fields but has not yet been validated with *in situ* data. The last objective is to prove the capability of the ARMOR3D product to detect mesoscale eddies and reproduce their hydrographic and dynamic 3D structure. In Section 4.2 we describe the data set used for the validation, in Section 4.3 we expose the results from the comparison, and in Section 4.4 we summarize the main conclusions.

4.2 Data and methods

4.2.1 Temperature, salinity and geostrophic currents from ARMOR3D

The ARMOR3D product is a multivariate global ocean state estimation which provides weekly 3D synthetic temperature and salinity fields in a $1/4^o$ horizontal Mercator grid with 33 unevenly spaced layers between the surface and 5500 m depth (Guinehut et al., 2012). The observation-based product combines remote sensing observations (SLA and SST) with *in situ* vertical profiles of temperature and salinity (mainly from Argo) using statistical methods. From the resulting global 3D data set of temperature and salinity, the geostrophic currents are estimated through the thermal wind relation considering the reference level at the surface, where geostrophic currents are derived from altimetry (Mulet et al., 2012). Mulet et al. (2012) also perform a validation of the ARMOR3D product by comparison with model reanalysis and in-situ observations (ANDRO current velocities from Argo floats displacements and velocity measurements from the RAPID-MOCHA current meter array). The multivariate ocean state data set is freely available for the Copernicus Marine Environment Monitoring Service (CMEMS) users. The version used here is the near-real-time ARMOR3D L4 analysis (the product available at the time of the study) which uses near-real-time altimetry maps that benefit from the same improvements done for DT14 altimetry reprocessing (Capet et al., 2014a; Pujol et al., 2016). However, a consistent ARMOR3D 1993-2016 reprocessing is also available. The date used for the comparison is 10 September 2014, although for the QG vertical velocity estimation we have also used the fields for 3 September 2014. In order to compare with the *in situ* data set, we used TEOS-10 algorithms to compute conservative temperature, Θ, absolute salinity, S_A, and potential density anomaly, σ_Θ, from the ARMOR3D temperature and practical salinity (Feistel, 2003, 2008).

4.2.2 High-resolution *in situ* data set

High-resolution *in situ* data are obtained from the interdisciplinary sampling of the subtropical intrathermocline eddy PUMP (Barceló-Llull et al., 2017b). The eddy was shed by the island of Tenerife in May 2014, and the survey took place 4 months later in a region 550 km to the southwest (Fig. 4.1). The sampling strategy included a

meridional transect crossing the eddy center consisted of 24 CTD stations 5 nautical miles apart and to a nominal depth of 1000 m (named the *Le Tourmalet* transect), and a 3D grid centered on the eddy center consisted of six SeaSoar and three discrete CTD zonal transects 90 nautical miles long. The SeaSoar provided vertical profiles from 10 m down to 325 m separated by 4 km, while the rosette stations were 10 nautical miles apart with a nominal depth of 400 m. The 3D survey was conducted over 5 days (6-11 September) and the *Le Tourmalet* transect was sampled over 3 days (12-15 September). The 3D sampling was centered at (20.1°W, 26.1°N) while the *Le Tourmalet* transect crossed the eddy center at 20.3°W as the eddy moved westward with a translation speed of 4 km d^{-1}. Raw data files were processed with Sea-Bird SEASOFT (`http://www.seabird.com/software/softrev.htm`). We used TEOS-10 algorithms to compute conservative temperature, Θ, absolute salinity, S_A, and potential density anomaly, σ_Θ (Feistel, 2003, 2008).

In all phases, current velocities were measured continuously using a hull-mounted acoustic Doppler current profiler (ADCP) working at 75 kHz. The potential density anomaly and horizontal velocity fields obtained from the 3D sampling were objectively interpolated onto a regular grid with a horizontal resolution of 0.1° (Lx = Ly = 40 km) and a vertical resolution of 8 m. Geostrophic velocities were diagnosed from the 3D potential density anomaly through thermal wind balance, imposing the ADCP velocity at the reference level (325 m depth). See Barceló-Llull et al. (2017b,a) for detailed description of the sampling strategy and data processing.

4.2.3 QG vertical velocity

Vertical velocity is inferred by integrating the QG omega equation (Hoskins et al., 1978) using the geostrophic velocity and density fields from the ARMOR3D product, obtaining w_{QGar}, and from the *in situ* data, obtaining w_{QGis}:

$$N^2 \boldsymbol{\nabla}_h^2 w + f(f + \zeta^g) w_{zz} = 2 \boldsymbol{\nabla}_h \cdot \mathbf{Q}^g, \tag{4.1}$$

where f = 6.4 $\times$ 10^{-5} s^{-1} is the Coriolis parameter (considered constant and computed at the mean latitude); $N^2 = -g\alpha_0\rho_z$ is the Brunt-Väisälä frequency, where

$\alpha_0 = \rho_0^{-1}$ is the mean specific volume, g is gravity, ρ is density and subscript z indicates a vertical derivative; $\zeta^g = v_x^g - u_y^g$ is the geostrophic vertical relative vorticity, where x and y subscripts represent partial derivatives in the eastward and northward directions; and the $\mathbf{Q}^g$ vector is defined as $\mathbf{Q}^g = \boldsymbol{\nabla}_h \mathbf{u}_h^g \cdot \boldsymbol{\nabla}_h b$, where $b = \rho g \alpha_0$ is the buoyancy. Vertical velocity is set to zero at the boundaries of the domain. Previous studies have demonstrated w_{QG} to be largely independent to the choice of boundary conditions a few grid points away from the boundary (e.g. Pascual et al., 2004).

4.3 Results

Five months before the cruise, Barceló-Llull et al. (2017b) periodically monitored the signature of the eddies generated by the Canary Islands in SLA maps provided by AVISO in order to select an anticyclonic eddy with a robust signature to be the target for their study. In the first stage of the eddy survey, with the aim to precisely detect the eddy center with perpendicular Seasoar transects, they realized that the real eddy size was smaller than was expected from the SLA maps. The overestimation of the eddy size in the SLA maps may be due to their lower resolution ($1/4°$) and the correlation scales used to construct the product. As the ARMOR3D dynamic height (dh) is derived from altimetry, this characteristic is also reflected in its signature as can be seen in Fig. 4.1, where the magenta box delimits the eddy region considering an *in situ*-derived radius of 46 km (Barceló-Llull et al., 2017b), while the cyan box highlights the eddy region from the dh signal.

The *in situ* meridional transect performed from 12 to 15 September 2014 allows comparison of the hydrography and dynamics of the eddy from the surface to 1000 m depth. Vertical sections of conservative temperature and absolute salinity anomalies (computed with respect the averaged value for each depth layer) for the *in situ* 2D transect and the ARMOR3D product are represented in Fig. 4.2. The PUMP eddy is characterized by a narrow cold and fresher upper layer located at 30 m depth and by an eddy hydrographic core centered between 200 and 500 m depth that is warmer and saltier than the surrounding waters (Barceló-Llull et al., 2017b). The ARMOR3D conservative temperature anomaly also shows a warm region between 200

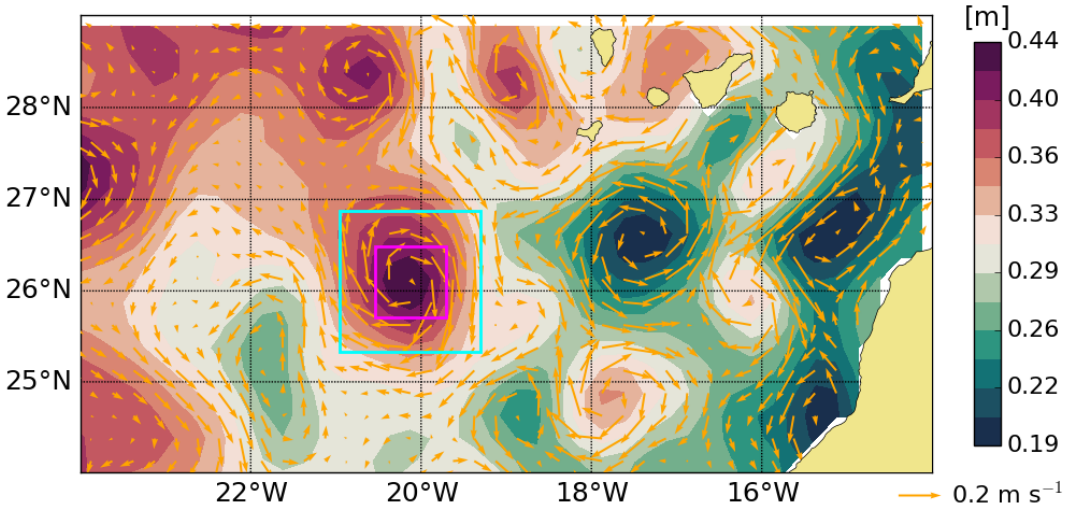

FIGURE 4.1: Absolute Dynamic Topography (ADT) with geostrophic velocity vectors at the sea surface from the ARMOR3D product (10-09-2014). Cyan box delimits the eddy region from the ARMOR3D data. Magenta box delimits the real eddy size from the *in situ* eddy data.

and 500 m depth with maximum values of ∼+0.7 ^{o}C, in agreement with the location of the eddy hydrographic core. However, the upper layer in the ARMOR3D field is warmer than the surrounding waters. The ARMOR3D absolute salinity anomaly also reflects the presence of the PUMP eddy between 200 and 500 m depth, although the saltier region is slightly vertically tilted to the south. The temperature and salinity anomalies introduced by the eddy in the ARMOR3D fields are smaller than in the high-resolution *in situ* fields.

The ARMOR3D density field, mainly dominated by temperature, is well correlated with *in situ* observations (black contours in Fig. 4.3a). The ARMOR3D field shows a depression of the isopycnals below 100 m and between 25°N and 27.5°N in accordance with the presence of an anticyclonic eddy, while the seasonal pycnocline remains flat. The ARMOR3D isopycnals are smoothed due to the lower resolution of this field in comparison with the *in situ* data, however the main pycnocline resembles well the depression depicted in the *in situ* data. Moreover, the eddy signal can be observed from 100 m to the maximum sampled depth (1000 m) in both fields. The upper doming of the seasonal pycnocline observed in the *in situ* data is the result of thermal wind balance in accordance with the vertical shear induced by the subsurface intensified anticyclonic flow (Barceló-Llull et al., 2017b). On the other

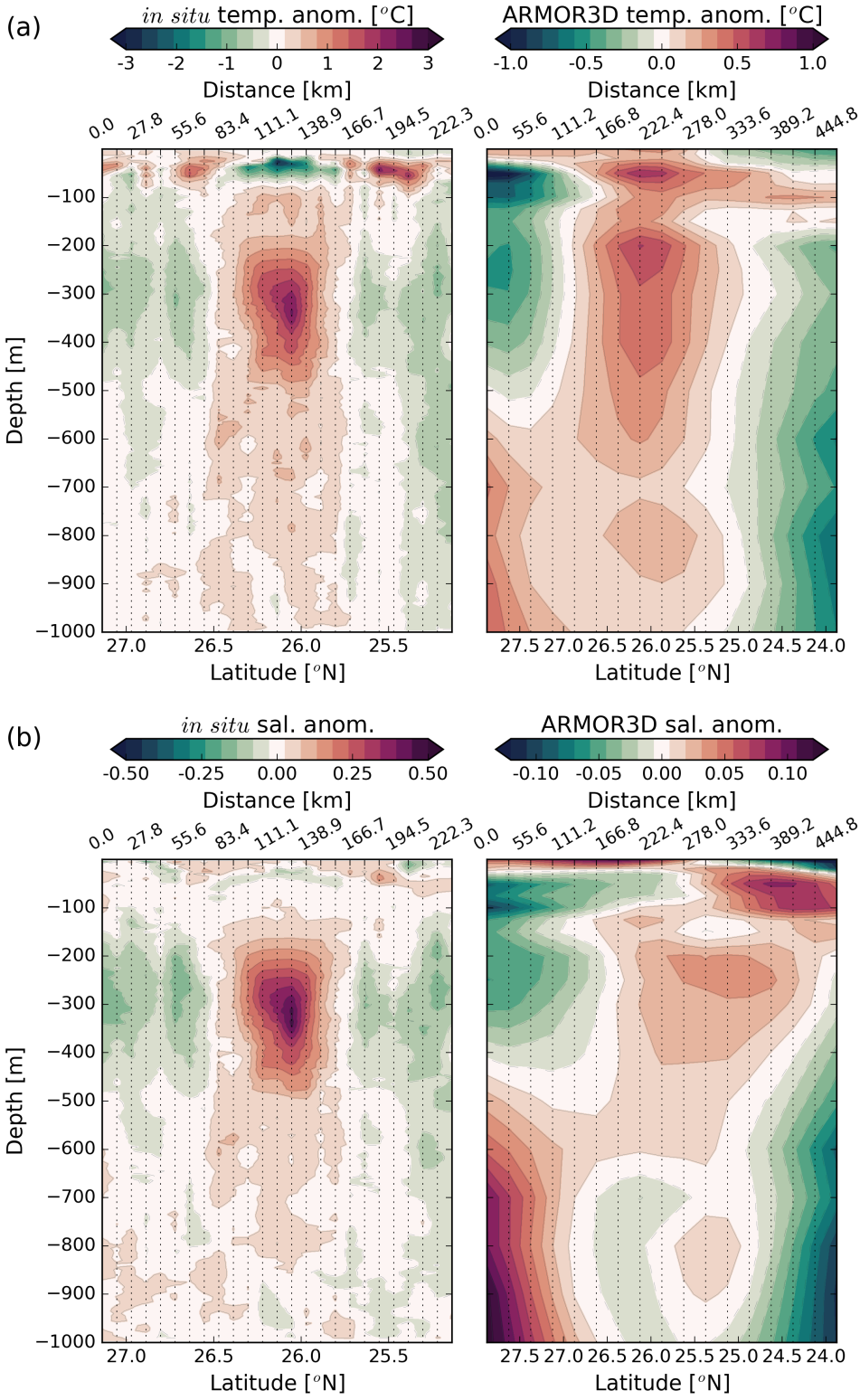

FIGURE 4.2: Meridional sections of conservative temperature (a) and absolute salinity (b) anomalies computed with respect the averaged value for each depth layer from the *in situ* Le Tourmalet transect (left panels) and the ARMOR3D product (right panels). The meridional sections are taken along 20.1°W for the ARMOR3D data and along 20.3°W for the *in situ* data in order to cross the eddy center in accordance with each data set.

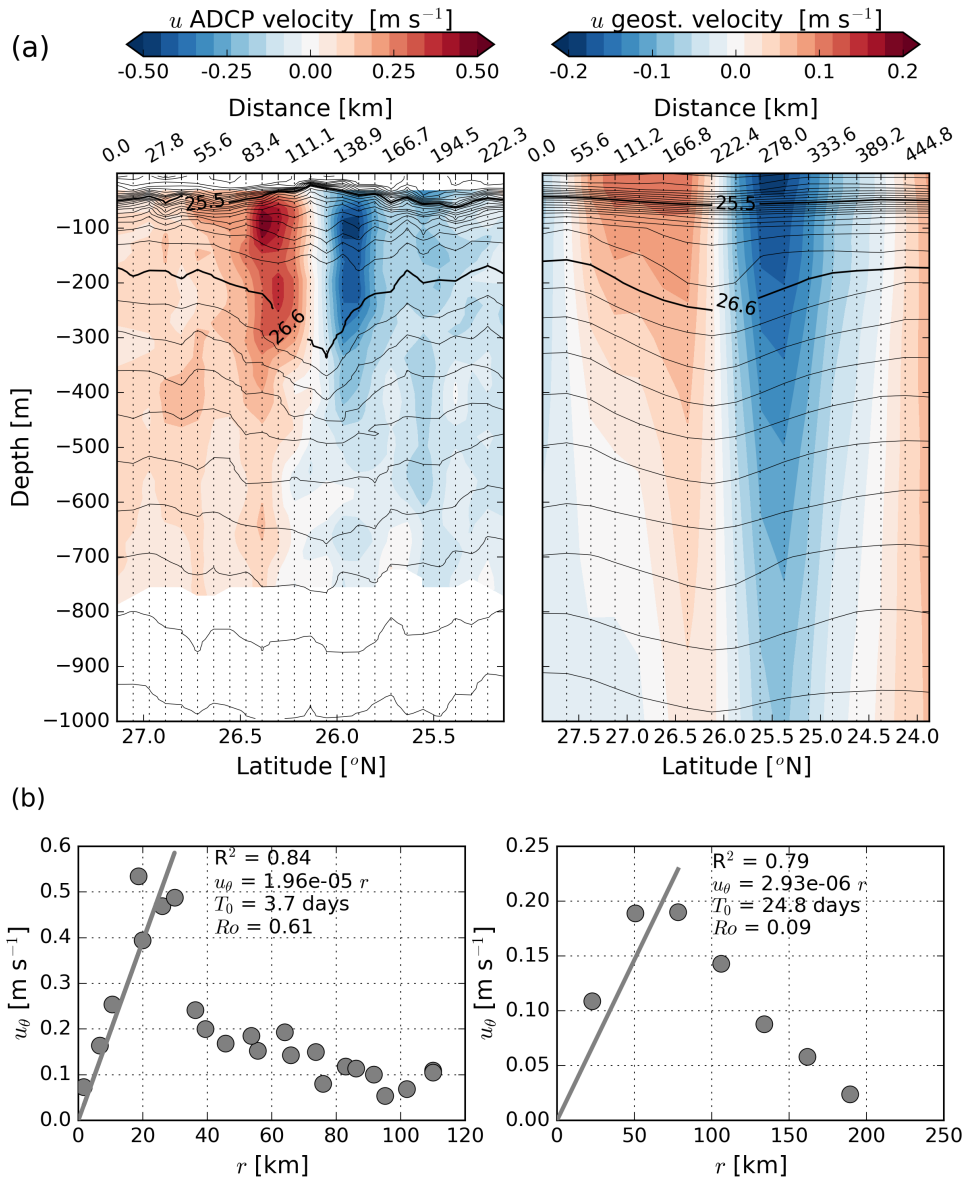

FIGURE 4.3: (a) u-component of the ADCP (left panel, *in situ* Le Tourmalet transect) and geostrophic (right panel, ARMOR3D data) velocities with superimposed contours of potential density anomaly, σ_Θ, with a contour interval of 0.1 kg m^{-3}. (b) Radial sections of absolute azimuthal velocity from the *in situ* Le Tourmalet transect (left) and ARMOR3D (right). Sections are taken at the depth of maximum azimuthal velocity: 97 m (surface) for the *in situ* Le Tourmalet transect (ARMOR3D).

hand, the ARMOR3D geostrophic velocities have higher values at the surface and, in accordance with thermal wind balance, the upper pycnocline remains flat.

The horizontal velocity measured with the ADCP during the meridional transect, which includes geostrophic and ageostrophic motions, has maxima of 0.38 (-0.35) m s^{-1} at 81 (97) m, while the ARMOR3D geostrophic velocity has maxima of 0.11 (-0.19)

m s^{-1} at the sea surface (Fig. 4.3a). The anticyclonic circulation in the ARMOR3D field extends from ∼24.5°N to ∼27.5°N in the upper layers with the maximum intensification concentrated in the upper 500 m depth, defined as the eddy base from *in situ* observations (Barceló-Llull et al., 2017b) although eddy influence is apparent at least until the maximum sampled depth (1000 m). From radial sections of azimuthal velocity at the depth of maximum intensification of the anticyclonic flow we may define its distribution as a Rankine profile in both data sets, with a linear increase of the azimuthal velocity from the eddy center to the eddy core edge (defined as the inner eddy region that is in near solid body rotation) and a slow decrease outside the eddy core. With the radial sections represented in Fig. 4.3b we can locate the eddy core edge at 30 km from the eddy center for the *in situ* data and 78 km for ARMOR3D. With the linear adjustment within the eddy core, we can obtain a period of rotation and Rossby number, Ro=ζ/f, at the eddy center of 3.7 days (24.8 days) and Ro = 0.61 (0.09) with the *in situ* (ARMOR3D) data. However, these results are sensitive to the low resolution of the ARMOR3D data.

In order to better compare both data sets and using the *in situ* 3D fields, we have taken advantage of a normalization of the axis in accordance with the *in situ*-derived eddy radius, r_{is} = 46 km, and an estimated ARMOR3D radius of $r_{ar} = 2r_{is}$ = 92 km (estimated from density and dh fields). Horizontal maps of the density field with superimposed vectors of geostrophic velocity for different depth layers are represented in Fig. 4.4. The eddy has a similar elliptical shape with the major axis oriented NW-SE in both data sets. The slight difference in magnitude is due to the shallower depression of the ARMOR3D isopycnals in comparison with the deeper depressed *in situ* isopycnals as can be observed in Fig. 4.5a (black contours). However, in the main pycnocline both data sets are well correlated with a correlation coefficient of 0.7-0.8 (Fig. 4.5b). The upper anticorrelation within the seasonal pycnocline is due to the dome-shape of the *in situ* isopycnals mentioned previously. On the other hand, *in situ* geostrophic velocity magnitude is double the ARMOR3D geostrophic velocity magnitude with a similar deceleration of the flow at the northern part of the eddy (Fig. 4.4). Correlation coefficients are high over all of the water column (Fig. 4.5b).

The scaled geostrophic vertical relative vorticity, $\mathrm{Ro}_g=\zeta^g/f$, is represented in Fig.

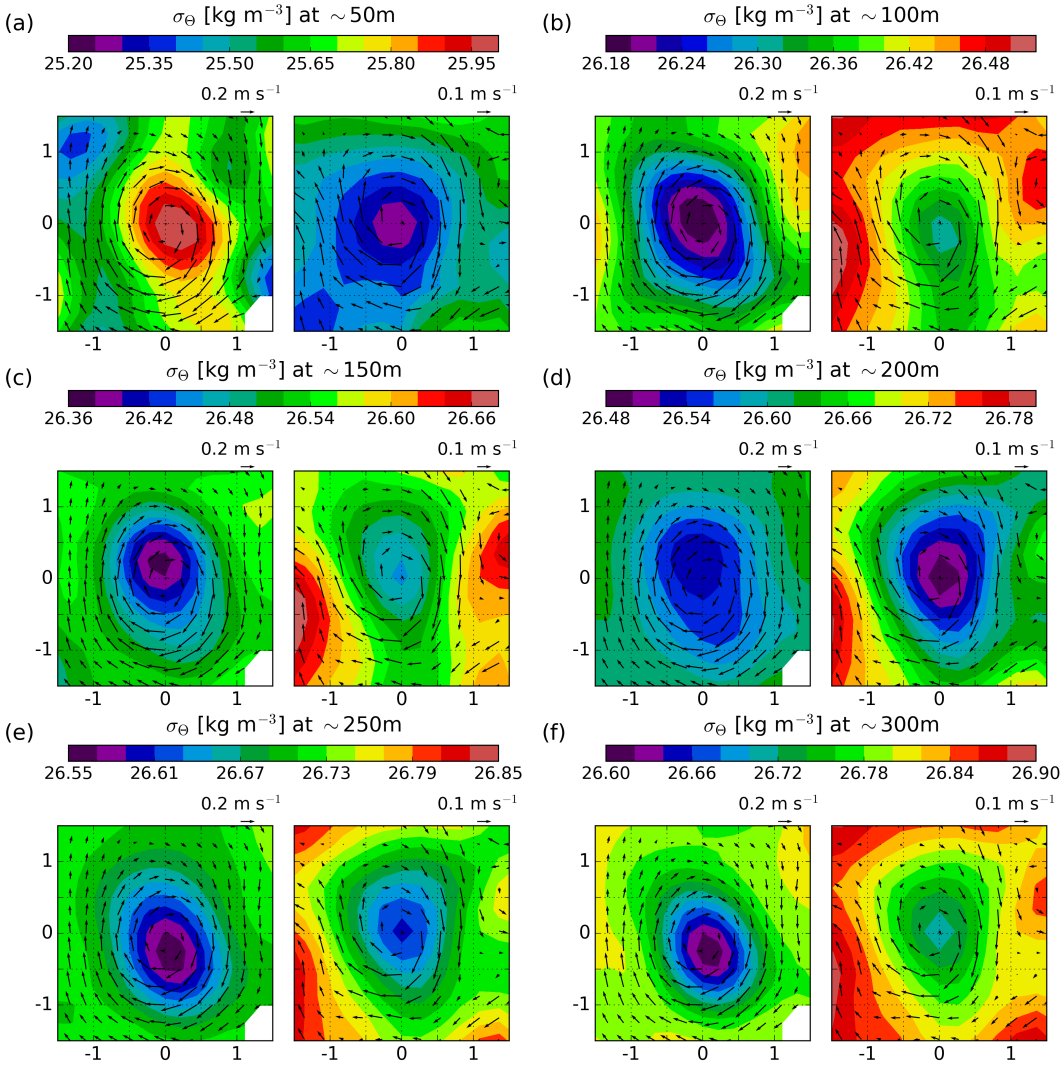

FIGURE 4.4: Horizontal sections of the potential density anomaly field, σ_Θ, at different depths with superimposed vectors of geostrophic velocity. Left (right) panel in each subplot represents the *in situ* (ARMOR3D) data. The longitude and latitude coordinates of the eddy are normalized by the eddy radius: 46 (92) km for the *in situ* (ARMOR3D) data.

4.5a and shows different vertical distributions for each data set related to the subsurface intensification of the *in situ* flow in contrast to the surface intensified ARMOR3D flow. The ARMOR3D field has an extreme value at the eddy center of Ro_g=-0.16, while with the *in situ* data we obtain a Ro_g=-0.46, almost three times larger. The correlation coefficient between both fields remains high in all the water column, 0.6-0.7.

QG vertical velocity has been estimated for both data sets. For the ARMOR3D case, we have derived the w_{QGar} for two consecutive weeks: 03-09-2014 and 10-09-2014, as the *in situ* 3D sampling was carried out in the middle of this two dates.

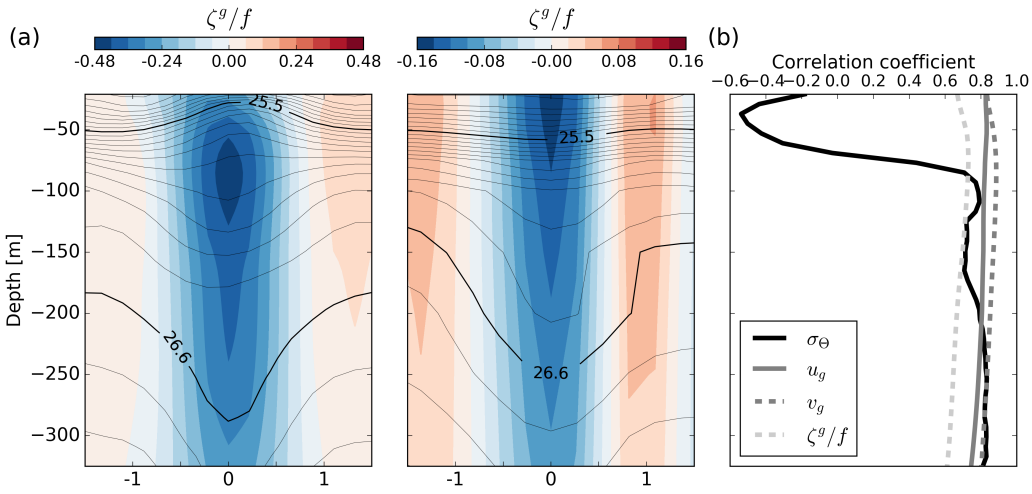

FIGURE 4.5: (a) Vertical section along 26.1°N of the geostrophic vertical relative vorticity scaled by the planetary vorticity ($\mathrm{Ro}_g = \zeta^g/f$). Contours represent the potential density anomaly, σ_Θ, with a contour interval of 0.1 kg m^{-3} for reference. Left (right) plot shows the *in situ* (ARMOR3D) data. The longitude coordinate is normalized by the eddy radius: 46 (92) km for the *in situ* (ARMOR3D) data. (b) Correlation coefficient of the *in situ* and ARMOR3D fields within the normalized eddy region. Black line is the potential density anomaly correlation coefficient, dark grey lines are the geostrophic velocity correlation coefficients, while light grey is the Ro_g correlation coefficient.

Horizontal maps of the inferred QG vertical velocity are represented in Fig. 4.6. The w_{QGis} has two different horizontal distribution in the seasonal and main pycnoclines (Barceló-Llull et al., 2017a). A horizontal map of the w_{QGis} at 50 m depth (Fig. 4.6a) shows the multipolar distribution typical for the upper layers, composed by small cells with alternate signs located along the eddy periphery. At the main pycnocline (Fig. 4.6c), the w_{QGis} distribution is characterized by a quadripolar pattern. On the other hand, w_{QGar} is characterized by the same horizontal distribution in all the water column (Figs. 4.6b and d). Its distribution is also composed of small cells with alternate signs located along the eddy periphery. More precisely, it shows 8 cells with alternate signs, as is the case for the w_{QGis} at 50 m depth (Fig. 4.6a). In consecutive weeks the location of the cells seems to be slightly rotated. If we compare the w_{QGar} distribution in 03-09-2014 with w_{QGis} at 50 m depth, we observe that the upwelling and downwelling cells are located at similar azimuthal positions in both cases. Besides this striking similarity, an underestimation of the magnitude of w_{QGar} is observed in comparison with w_{QGis}, which is 3 to 4 times higher.

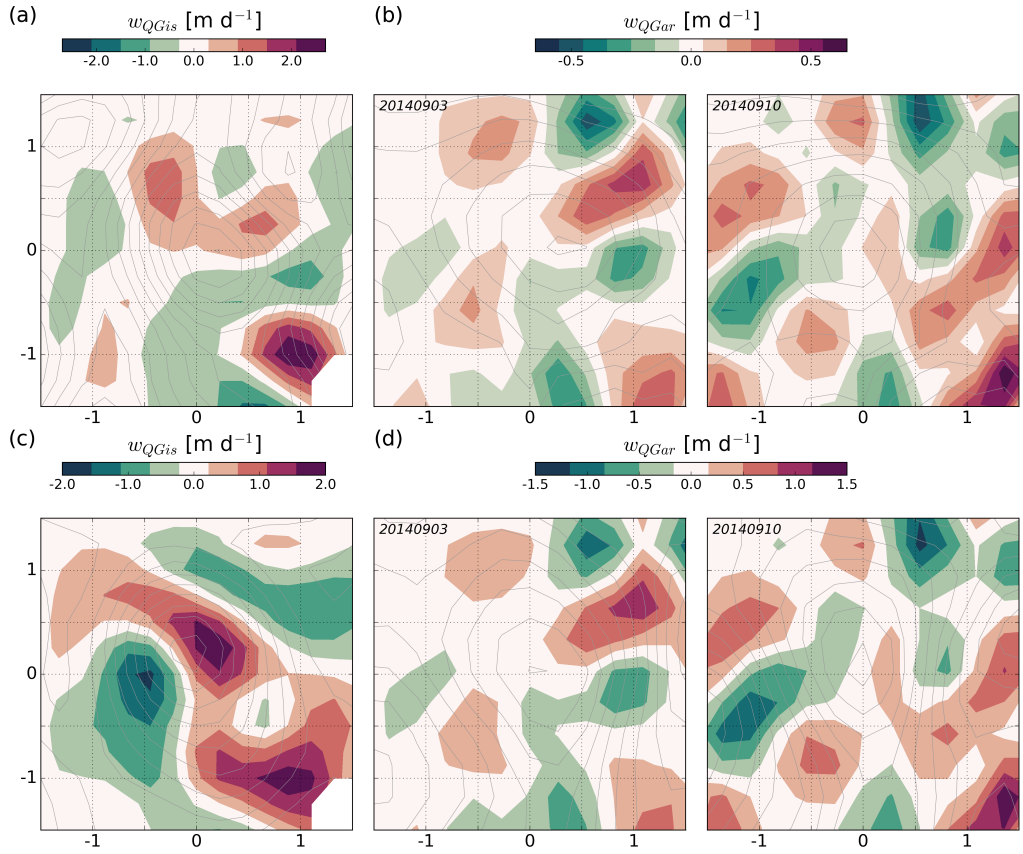

FIGURE 4.6: QG vertical velocity estimated with the *in situ* data (a and c) and with the ARMOR3D product (b and d) for two consecutive weeks (03-09-2014 and 10-09-2014). Upper (lower) plots show the QG vertical velocity at $\sim$ 50 (150) m depth. Contours of potential density anomaly, σ_Θ, are represented for reference with the same contour levels as Fig. 4.4. The longitude and latitude coordinates of the eddy are normalized by the eddy radius: 46 (92) km for the *in situ* (ARMOR3D) data.

4.4 Concluding remarks

We have presented a validation of the ARMOR3D hydrographic and dynamic fields with high-resolution *in situ* observations in order to analyze the ability of the ARMOR3D product to describe the 3D structure of mesoscale eddies. ARMOR3D is capable of reproducing the hydrographic vertical signature of the eddy below the seasonal pycnocline although it inherits the overestimation of the eddy size by a factor of 2 from altimetry. The elliptical eddy shape is well characterized by the ARMOR3D density field as well as the deceleration of the flow at the northern edge of the eddy. ARMOR3D resolves a surface intensified eddy with geostrophic currents underestimated by a factor 2, while the Rossby number is underestimated by

a factor of 3. Inferred QG vertical velocity resembles well the *in situ*-derived QG vertical velocity distribution typical of the upper layers, with a magnitude 3 to 4 times smaller. In conclusion, the ARMOR3D product is capable of describing the 3D signature of the eddy with an underestimation of the geostrophic and QG vertical velocities. Moreover, in addition to the near-real-time ARMOR3D product used here, a full reprocessing exists and slightly improves the results.

Data from multiplatform experiments such as PUMP can play an important role in validation of products such as ARMOR3D, and we expect to see more exemplars in the future as the need for and benefit of these types of experiment become apparent (Shcherbina et al., 2015; Pascual et al., 2017). These approaches are complementary to the traditional statistical validations such as by, e.g., Guinehut et al. (2012) and Mulet et al. (2012). The ARMOR3D data used here clearly benefited from the simultaneous presence of three Argo floats near/within the sampling area. However, multiyear subregional eddy composites based on ARMOR3D tracers and velocities have been shown to be statistically robust at the Brazil-Malvinas Confluence (Mason et al., 2017), suggesting that ARMOR3D eddies are generally well resolved.

Part III

General conclusions and future perspective

In this thesis we have analyzed different aspects of mesoscale dynamics with emphasis on the anatomy of an anticyclonic intrathermocline eddy and mesoscale vertical motions. In Chapter 1 we demonstrate the importance of vertical motions on driving nutrient fluxes from the deep ocean to the euphotic zone in regions with mesoscale activity (as meanders and eddies) and pre-existing vertical gradients of nutrients. The Lagrangian simulations reveal that vertical motions may account for local increases of nitrate uptake rates of up to 30% in oligotrophic regions with moderate mesoscale activity.

The high mesoscale activity characteristic of the Canary Eddy Corridor makes it suitable for the study of the hydrography and dynamics of mesoscale eddies, including the ageostrophic secondary circulation and its impact on marine ecosystems. With this aim it was conduced the interdisciplinary sampling of the PUMP eddy. In Chapter 2 we describe the sampling strategy, the resulting dataset, and the anatomy of the eddy. The PUMP eddy was generated at the Tenerife Island in May 2014. The survey took place in September 2014, when the PUMP eddy was 4 months old, at its mature stage, 550 km to the southwest of the eddy generation region. The sampling effort included transects crossing the eddy center with continuous tows of a CTD probe on an undulating vehicle (SeaSoar), a 3D grid centered on the eddy center consisting on SeaSoar and rosette zonal transects spaced 10 nm apart, and a near submesoscale meridional transect crossing the eddy center with 24 CTD stations spaced 5 nm, microstructure measurements, and water samples for biogeochemical studies. Current velocities were measured continuously using an ADCP. With these data we have been able to analyze the 2D eddy signature from the surface to 1000 m depth, and the 3D eddy structure to a maximum depth of 325 m.

The anatomy of the eddy can be summarized as follows. The PUMP eddy is an intrathermocline eddy characterized by a biconvex shape of the isopycnals with a subsurface intensification of the flow located around 85 m depth, which we named the eddy dynamical core. The eddy has as a particular feature the presence of a homogeneous layer of subtropical mode water centered at 225 m depth. The biconvex shape of the eddy and the presence of a homogeneous layer are in accordance with the occurrence of two minimums of PV as the decrease of stratification reduces

PV through the stretching term. The eddy has a radius of 46 km and a vertical extension of 500 m, although it influences the water column to at least 1000 m depth. The doming of the upper layers induces a denser and colder narrow region, while the deeper depression of the main pycnocline, thermocline, and halocline leads a lighter, warmer, and saltier region between 200 and 500 m depth that we named the eddy hydrographic core. This eddy region is also characterized by a relative maximum of DO. The horizontal density field reveals an elliptical eddy shape. The eddy has a central core that is in near solid body rotation with a period of $\sim$4 days surrounded by a narrow outer ring that rotates slowly. The maximum Rossby number within the eddy is 0.6, hence, the eddy is moderately ageostrophic. As a particular characteristic of the PUMP eddy it has a larger content of kinetic energy than available potential energy. The eddy has the capacity of trapping fluid within its core with little mixing with the surrounding waters. The contents of available heat and salt anomalies within the eddy have been computed. These contents, in terms of units per volume, are higher than those estimated in other intrathermocline eddies of the California EBUS and PCCS.

As already mentioned, in Chapter 1 we have added evidences to the importance of mesoscale vertical motions on sustaining primary production. In particular, mesoscale eddies are associated with important biogeochemical activity. However, the details of the vertical velocity field within these features are still under discussion. In Chapter 3 we take advantage of the 3D data obtained during the PUMP cruise to infer, for the first time, the vertical velocity field within an intrathermocline eddy through the integration of a generalized omega equation valid for the high Rossby regime. The inferred mesoscale vertical velocity has two different horizontal distributions: in the seasonal pycnocline it is characterized by a multipolar distribution along the eddy periphery, while in the main pycnocline it has a dipolar distribution with a downwelling cell on the west and an upwelling cell on the east. Maximum values of mesoscale vertical velocity are located between 160 and 185 m depth reaching up to 6.4 m d^{-1}. Our observations indicate that the eddy enhances cholorophyll-a concentration at the eddy periphery, coinciding with the occurrence of upwelling cells along the eddy periphery that may bring nutrients into the euphotic layer.

We have also analyzed the forcing mechanisms for the inferred mesoscale vertical velocity. In the upper layers, the dominant forcing may be a combination of nonlinear Ekman pumping and modulation by vortex Rossby waves. In the deeper layers, the dipolar distribution of mesoscale vertical velocity suggests the possibility of a deep wind influence through an enhancement of ageostrophic vertical shear. This dipolar distribution arises from the interaction of the horizontal deformation of the density field by the geostrophic velocity and the advection of vertical relative vorticity by the ageostrophic vertical shear. The horizontal ageostrophic secondary circulation closes the dipolar vertical velocity distribution inside the intrathermocline eddy and is mainly dominated by the centripetal acceleration.

In Chapter 4, the ARMOR3D product used in Chapter 1 is compared with the independent *in situ* data obtained from the PUMP survey. ARMOR3D is able to reproduce the hydrographic vertical structure of the PUMP eddy below the seasonal pycnocline, and its horizontal elliptical shape. The ARMOR3D flow is surface intensified and also shows velocity asymmetry, that is, a deceleration in the northern edge of the eddy. The eddy size in the ARMOR3D fields is overestimated by a factor of 2, while the geostrophic velocity and the Rossby number are underestimated. The QG vertical velocity inferred with AMOR3D fields resembles the *in situ*-derived QG vertical velocity, showing the same multipolar distribution found with *in situ* data in the upper layers.

In this thesis we have quantified the importance of the (large) mesoscale vertical velocities on the injection of nutrients into the euphotic layer in an oligotrophic region of the world ocean. This quantification is an underestimation of the real vertical velocity contribution as the ARMOR3D horizontal resolution used for this analysis is only $1/3^{\circ}$. The eddy sampling carried out within the Canary Eddy Corridor has provided the necessary high-resolution data to analyse in detail the eddy anatomy and the induced mesoscale vertical velocity. The inference of the vertical velocity field within mesoscale eddies requires quasi-synoptic high-resolution 3D fields. Because of this, there are few studies of ASC in mesoscale eddies, and these analysis are based on low-resolution data. Hence, the ASC inferred in this dissertation constitutes the first estimation performed within an anticyclonic intrathermocline eddy with high-resolution *in situ* data. Moreover, we have provided a detailed analysis of

the forcing mechanisms responsible for the inferred ASC field.

Besides the advances on the knowledge of mesoscale dynamics provided by this thesis, more experimental studies are needed to corroborate the generality of these results. Moreover, a high uncertainty still exists in our understanding of the role of submesoscale dynamics on the oceanic vertical pump and, hence, more observational efforts are required to analyze the small scale dynamics (Klein and Lapeyre, 2009; Mahadevan, 2016). Fine resolution satellite observations from the wide-swath SWOT altimeter will allow unique observations in the 15-100 km range of wavelength that will bring insight into this issue (Fu and Ferrari, 2008) .

As specific future work, it remains to understand the reason for the difference between the predicted quadripolar distribution of mesoscale vertical velocity in an f-plane and non-forced numerical elliptical anticyclonic PV ball (see Part I), and the dipolar distribution of mesoscale vertical velocity inferred with *in situ* data shown in Chapter 3. Also, taking advantage of the demonstrated capacity of the ARMOR3D product to reproduce mesoscale eddies, we aim to lead a work based on eddy composites of ARMOR3D tracers and velocities in the Canary Eddy Corridor to analyze the mesoscale eddy structure, evolution, and heterogeneity in this highly dynamical region.

Part IV

Resumen en español

(Spanish summary)

Introducción

Las estructuras oceánicas de mesoescala, como los frentes o los remolinos, tienen una función importante en la circulación global oceánica mediante la generación de flujos de gran escala de calor, sal, momento y trazadores biogeoquímicos (Danabasoglu et al., 2012, 2008; Jochum et al., 2008; Griffies, 2004). Además, estas estructuras inducen fuertes velocidades horizontales y verticales que tienen una influencia importante en los procesos biológicos (McGillicuddy, 2016; Rodríguez et al., 2001; Mahadevan and Archer, 2000). Los afloramientos costeros o las áreas frontales son ejemplos de estructuras mesoescalares con intensas velocidades verticales que pueden contribuir a la introducción de nutrientes en la capa fótica (Mahadevan, 2014).

Un tipo particular de estructuras de mesoescala son los remolinos, estructuras coherentes del orden de 100 km que tienen la capacidad de atrapar fluido de las regiones de formación dentro de sus núcleos (e.g. Chelton et al., 2011b). Los remolinos de mesoescala se pueden alejar de la costa durante meses, o incluso años, con una velocidad tangencial mayor que la velocidad de translación. En consecuencia, los remolinos transportan calor, masa y trazadores biogeoquímicos dentro de sus núcleos durante largas distancias y, por lo tanto, tienen una contribución importante en la circulación general termohalina, en la distribución de masas de agua y en la biología oceánica (McWilliams, 2008). Además, las velocidades verticales dentro de los remolinos de mesoescala pueden tener un papel importante en el intercambio vertical de calor, sal y trazadores biogeoquímicos entre el océano profundo y las capas superficiales (McGillicuddy, 2016). Sin embargo, existe una gran incertidumbre respecto a los mecanismos mediante los cuales las estructuras de mesoescala, especialmente los remolinos, influyen en los ecosistemas marinos (e.g. Martin and Richards, 2001; McGillicuddy et al., 2007, 2008; Chelton et al., 2011a; Buongiorno Nardelli, 2013).

El archipiélago Canario contituye una cadena zonal formada por siete islas situadas al noroeste de África. Todas las islas, excepto Fuerteventura y Lanzarote, son montañosas con picos que exceden los 1000 m. Las Islas Canarias están localizadas en la zona de transición entre el océano abierto y el afloramiento costero de la costa noroeste africana, caracterizada por la presencia de la Corriente Canaria y los vientos alisios (Barton et al., 1998; Barton and Arístegui, 2004; Pelegrí et al., 2005). Por lo

tanto, el archipiélago Canario actúa como obstáculo para la Corriente Canaria y los vientos alisios siendo, en consecuencia, una fuente de generación de remolinos de mesoescala (Arístegui et al., 1994; Barton et al., 2000; Jiménez et al., 2008; Piedeleu et al., 2009; Sangrà et al., 2005, 2007, 2009).

Los remolinos de mesoescala generados por las Islas Canarias contribuyen al Corredor de Remolinos de Canarias (CEC), el cual constituye el camino principal para los remolinos de larga duración ($>$ 3 meses) del Atlántico noreste subtropical (Sangrà et al., 2009). Las características geográficas y topográficas de las Islas Canarias, así como la presencia del corredor de remolinos, hacen de la región Canaria un laboratorio natural para el estudio de remolinos mesoescalares. Durante las pasadas décadas varios autores han investigado remolinos generados en esta zona (e.g. Arístegui et al., 1994; Sangrà et al., 2007). Dichos remolinos se generan principalmente en primavera y verano (Piedeleu et al., 2009) con diámetros similares a la dimensión de la isla donde se generan y con una extensión vertical de 300-700 m. La evolución del remolino está constituida por tres fases: una etapa temprana, donde el núcleo del remolino, que rota en sólido rígido siguiendo un perfil de Rankine, ocupa todo el remolino; una etapa madura donde el núcleo está rodeado por un anillo que rota más lentamente, y una etapa de decaimiento en la cual el remolino se disipa (Sangrà et al., 2005, 2007). Los remolinos maduros pueden caracterizarse por una forma elíptica así como también circular (Sangrà et al., 2005, 2007; Pacheco and Hernández-Guerra, 1999).

Objetivos

El objetivo general de la tesis es investigar las estructuras termohalina y dinámica, incluyendo la circulación secundaria ageostrófica, de estructuras de mesoescala basándonos en observaciones remotas e *in situ*, prestando especial atención a los remolinos de mesoescala y a las velocidades verticales inducidas. Para conseguir esto utilizamos una reconstrucción basada en observaciones llamada ARMOR3D, la cual incorpora observaciones remotas (anomalía del nivel del mar y temperatura de la superficie del mar) con perfiles verticales de temperatura y salinidad de datos *in situ* disponibles (principalmente de Argo) para obtener una estimación del estado

del océano global tridimensional (3D). Además, analizamos datos de alta resolución obtenidos del muestreo interdisciplinar de un remolino intratermoclino dentro del Corredor de Remolinos de Canarias. Con estos conjuntos de datos resolvemos diferentes versiones de la ecuación omega para diagnosticar la velocidad vertical mesoescalar y estudiar su contribución en la distribución de nutrientes, así como también determinar por primera vez a partir de datos *in situ* de alta resolución la estructura 3D de la circulación secundaria ageostrófica dentro de un remolino intratermoclino mesoescalar.

El muestreo interdisciplinar que tuvo lugar en Septiembre de 2014 tenía como objetivo principal estudiar la bomba vertical oceánica dentro de un remolino anticiclónico (Klein and Lapeyre, 2009). El remolino muestreado (llamado remolino PUMP) fue identificado a partir de altimetría y fue intensivamente muestreado con CTD, ADCP, perfilador de microturbulencia, muestras de agua y boyas. Aquí pretendemos realizar un análisis detallado de la estructura hidrográfica del remolino PUMP que aportará el conocimiento hidrográfico necesario para la comprensión de los procesos dinámicos acaecidos dentro del remolino, por ejemplo, atrapamiento de ondas quasi-inerciales, circulación secundaria ageostrófica (Barceló-Llull et al., 2017a), mezcla vertical, etc.

A pesar de que el muestreo *in situ* con alta resolución de estructuras mesoescalares es fundamental para describir en detalle la hidrografía y los procesos oceánicos, éste solo es capaz de cubrir cortos períodos de tiempo y reducidas regiones del océano global. Por ello, se han desarrollado otras metodologías para analizar la variabilidad espacial y temporal de las estructuras de mesoescala. Dentro de estos métodos se sitúa el producto ARMOR3D, el cual proporciona datos globales y 3D de temperatura, salinidad y velocidad geostrófica con una resolución horizontal de $1/4^\circ \times 1/4^\circ$ y con una resolución temporal semanal. Aquí vamos a realizar una validación del producto ARMOR3D con los datos *in situ* independientes obtenidos del muestreo del remolino PUMP, con el objetivo de demostrar las capacidades del producto ARMOR3D para detectar remolinos mesoescalares y reproducir su estructura hidrográfica 3D.

Resumen y conclusiones

En esta tesis hemos analizado diferentes aspectos de la dinámica mesoescalar con especial atención a la estructura y circulación de un remolino intratermoclino anticiclónico. En el Capítulo 1 hemos demostrado la importancia de las velocidades verticales en la redistribución de nutrientes en regiones con moderada actividad mesoescalar. Los resultados demuestran que las velocidades verticales, aunque tengan una magnitud relativamente pequeña, pueden ser importantes en la introducción de nutrientes dentro de la capa fótica en áreas con gradientes verticales de nutrientes. Las simulaciones Lagrangianas revelan que las velocidades verticales inducen un aumento local de la asimilación de nitratos de hasta el 30% en regiones oligotróficas.

La alta actividad mesoescalar característica del Corredor de Remolinos de Canarias hace de esta región un lugar idóneo para el estudio hidrográfico y dinámico de remolinos mesoescalares, incluyendo la circulación secundaria ageostrófica y su impacto en los ecosistemas marinos. Con este objetivo se realizó el muestreo interdisciplinar del remolino PUMP. En el Capítulo 2 se describe la estrategia de muestreo seguida, los datos obtenidos y la anatomía del remolino. El remolino PUMP fue generado por la Isla de Tenerife en Mayo del 2014. El muestreo se realizó en Septiembre de 2014, cuando el remolino tenía 4 meses de edad, en su fase madura, 550 km al suroeste de la región de formación. El muestreo incluyó transectos cruzando el centro del remolino con el arrastre continuo de una sonda CTD en un vehículo undulante (SeaSoar), una malla 3D centrada en el centro del remolino consistente en transectos zonales con SeaSoar y roseta separados 10 millas náuticas, y un transecto meridional cercano a la submesoescala constituido por 24 estaciones CTD separadas 5 nm, medidas de microestructura y muestras de agua para estudios biogeoquímicos. La velocidad de las corrientes horizontales fue medida en continuo usando un ADCP. Con estos datos hemos podido analizar la señal 2D del remolino desde la superficie hasta 1000 m de profundidad, y la estructura 3D hasta una profundidad máxima de 325 m.

La anatomía del remolino se puede resumir como sigue. El remolino PUMP es un remolino intratermoclino caracterizado por una forma biconvexa de las isopicnas

con una intensificación subsuperficial del flujo alrededor de los 85 m de profundidad. A esta zona de intensificación subsuperficial la llamamos núcleo dinámico del remolino. El remolino tiene como característica particular la presencia de una capa homogénea de agua modal subtropical centrada en 225 m. La forma biconvexa del remolino y la presencia de una capa homogénea concuerdan con la presencia de dos mínimos de vorticidad potencial (PV) debido a que la disminución de la estratificación reduce la PV. El remolino tiene un radio de 46 km y una extensión vertical de 500 m, aunque influencia la columna de agua hasta al menos los 1000 m. El abombamiento de las capas superiores induce una región estrecha densa y fría, mientras que la depresión de la picnoclina, la termoclina y la haloclina principales da lugar a una región menos densa, más cálida y más salina situada entre 200 y 500 m que nosotros llamamos núcleo hidrográfico del remolino. Esta región se caracteriza también por un máximo relativo de oxígeno disuelto (DO). El campo horizontal de densidad indica que el remolino tiene forma elíptica. El remolino está formado por un núcleo central que rota en sólido rígido con un período de $\sim$4 días rodeado por un anillo fino que rota más lentamente. El número de Rossby extremo dentro del remolino es de -0.6 y, por lo tanto, el remolino es moderadamente ageostrófico. Como característica particular del remolino PUMP, éste tiene un valor de energía cinética mayor que el valor de energía potencial disponible. El remolino tiene la capacidad de atrapar fluido en su núcleo con poco intercambio con las aguas de alrededor. Se han calculado los contenidos de calor y sal disponible dentro del núcleo del remolino. Estos contenidos por unidad de volumen son mayores que las estimaciones correspondientes a otros remolinos intratermoclinos de los EBUS Californiano y de Peru-Chile.

En el Capítulo 1 hemos dado evidencias de la importancia de las velocidades verticales de mesoescala en el sustento de la producción primaria. En particular los remolinos de mesoescala están asociados a una importante actividad biológica. Sin embargo, los detalles del campo de velocidad vertical dentro de estas estructuras están aún en discusión. En el Capítulo 3, a partir de los datos 3D obtenidos en la campaña PUMP, hemos calculado, por primera vez, el campo de velocidad vertical dentro de un remolino intratermoclino a partir de la integración de una ecuación omega generalizada válida para valores altos del número de Rossby. La velocidad

vertical obtenida tiene dos distribuciones horizontales diferentes: en la picnoclina estacional está caracterizada por una distribución multipolar a lo largo de la periferia del remolino, mientras que en la picnoclina principal tiene una distribución dipolar con una celda de subducción en el oeste y una celda de afloramiento en el este. Los valores máximos de velocidad vertical se sitúan entre 160 y 185 m y llegan a los 6.4 m d^{-1}. Nuestras observaciones indican que el remolino aumenta la concentración de clorofila a lo largo de la periferia del remolino, coincidiendo con la presencia de celdas de afloramiento que podrían introducir nutrientes en la capa fótica.

También hemos analizado los mecanismos de forzamiento de la velocidad vertical calculada. En las capas superiores, el forzamiento dominante podría ser una combinación de Ekman pumping no lineal y de una modulación por ondas de Rossby de vórtice. En las capas profundas, la distribución dipolar de velocidad vertical sugiere la posibilidad de una influencia profunda del viento a través del aumento de la cizalla vertical ageostrófica. Esta distribución dipolar surge de la interacción de la deformación horizontal del campo de densidad por parte de la velocidad geostrófica y la advección de vorticidad vertical relativa por parte de la cizalla vertical ageostrófica. La circulación secundaria ageostrófica horizontal cierra la distribución dipolar de velocidad vertical dentro del remolino intratermoclino, y está principalmente dominada por la aceleración centrípeta.

In el Capítulo 4 hemos comparado los campos ARMOR3D con los datos *in situ* independientes obtenidos de la campaña PUMP. ARMOR3D es capaz de reproducir la estructura vertical hidrográfica del remolino PUMP por debajo de la picnoclina estacional, así como también su forma horizontal elíptica. La velocidad geostrófica de ARMOR3D está intensificada superficialmente y también muestra asimetría, es decir, una deceleración en el borde norte del remolino. El tamaño del remolino en los campos ARMOR3D está sobreestimado por un factor 2, mientras que la velocidad geostrófica y el número de Rossby están infraestimados. La velocidad vertical quasi-geostrófica (QG) inferida con los campos ARMOR3D se asemeja a la velocidad vertical QG derivada con los campos *in situ*, mostrando la misma distribución multipolar encontrada con los datos *in situ* en las capas superiores.

En esta tesis se ha cuantificado la importancia de la velocidad vertical

mesoescalar en la introducción de nutrientes en la capa fótica en una región oligotrófica del océano global. Esta cuantificación es una infraestimación de la contribución real de la velocidad vertical ya que la resolución de ARMOR3D utilizada para este análisis es solamente $1/3°$. El muestreo del remolino realizado dentro del Corredor de Remolinos de Canarias ha aportado los datos de alta resolución necesarios para analizar en detalle la anatomía del remolino y la velocidad vertical mesoescalar inducida. La estimación del campo de velocidad vertical dentro de remolinos de mesoescala requiere datos 3D, quasi-sinópticos y de alta resolución. Por ello, se han realizado pocos estudios de la circulación secundaria ageostrófica (ASC) en remolinos de mesoescala, y estos estudios se basan en datos de baja resolución. Por lo tanto, la ASC calculada en el marco de esta tesis representa la primera estimación realizada dentro de un remolino intratermoclino anticiclónico con datos *in situ* de alta resolución. Además, hemos realizado un análisis detallado de los forzamientos responsables del campo de ASC.

A pesar de los avances en el conocimiento de la dinámica mesoescalar aportados por esta tesis, se necesitan más estudios experimentales para corroborar la generalidad de estos resultados. Además, aún existe una gran incertidumbre respecto al papel que tiene la dinámica submesoescalar en la bomba vertical oceánica y, por lo tanto, se necesitan más esfuerzos observacionales para analizar las dinámicas de pequeña escala (Klein and Lapeyre, 2009; Mahadevan, 2016). Las observaciones satelitarias con resolución fina obtenidas del altímetro SWOT van a permitir observaciones únicas en el rango de longitud de onda de 15-100 km (Fu and Ferrari, 2008).

Como trabajo futuro, aún queda por entender el motivo de la diferencia entre la distribución quadrupolar de velocidad vertical predecida numéricamente (vea la Parte I), y la distribución de velocidad vertical dipolar obtenida con los datos *in situ*. También, aprovechando la demostrada capacidad del producto ARMOR3D de reproducir los remolinos de mesoescala, tenemos como objetivo realizar un trabajo basado en reconstrucciones medias de trazadores y velocidades de ARMOR3D dentro de remolinos en la zona del Corredor de Remolinos de Canarias para analizar la estructura de los remolino de mesoescala, su evolución y heterogeneidad en esta zona con alta dinámica.

Bibliography

Allen, J. T., Pollard, R. T., and New, A. L. (2012). *Ocean Variability & Acoustic Propagation*, chapter How do eddies modify the stratification of the thermocline?, pages 432–448. Springer Science & Business Media.

Allen, J. T. and Smeed, D. A. (1996). Potential Vorticity and Vertical Velocity at the Iceland-Færœs Front. *J. Phys. Oceanogr.*, 26(12):2611–2634.

Allen, J. T., Smeed, D. A., Nurser, A. J. G., Zhang, J. W., and Rixen, M. (2001). Diagnosis of vertical velocities with the QG omega equation: an examination of the errors due to sampling strategy. *Deep Sea Res.*, 48(2):315–346.

Alonso-González, I. J., Arístegui, J., Lee, C., Sánchez-Vidal, A., Calafat, A., Fabrés, J., Sangrà, P., and Mason, E. (2013). Carbon Dynamics within Cyclonic Eddies: Insights from a Biomarker Study. *PLoS ONE*, 8(12):e82447.

Arístegui, J., Sangrà, P., Hernández-León, S., Cantón, M., Hernández-Guerra, A., and Kerling, J. L. (1994). Island-induced eddies in the Canary Islands. *Deep-Sea Res.*, 49(10):1087–1101.

Arístegui, J., Tett, P., Hernández-Guerra, A., Basterretxea, G., Montero, M. F., Wild, K., Sangrà, P., Hernández-León, S., Cantón, M., García-Braun, J. A., Pacheco, M., and Barton, E. D. (1997). The influence of island-generated eddies on chlorophyll distribution: A study of mesoscale variation around Gran Canaria. *Deep-Sea Res.*, 44(1):71–96.

Badin, G. (2012). Surface semi-geostrophic dynamics in the ocean. *Geophys. Astrophys. Fluid Dyn.*, 107(5).

Barceló-Llull, B., Mason, E., Capet, A., and Pascual, A. (2016). Impact of vertical and horizontal advection on nutrient distribution in the southeast Pacific. *Ocean Sci.*, 12:1003–1011.

Barceló-Llull, B., Pallàs-Sanz, E., Sangrà, P., Martínez-Marrero, A., Estrada-Allis, S. N., and Arístegui, J. (2017a). Ageostrophic Secondary Circulation in a Subtropical Intrathermocline Eddy. *J. Phys. Oceanogr.*, 47(5):1107–1123.

Barceló-Llull, B., Sangrà, P., Pallàs-Sanz, E., Barton, E. D., Estrada-Allis, S. N., Martínez-Marrero, A., Aguiar-González, B., Grisolía, D., Gordo, C., Rodríguez-Santana, A., Marrero-Díaz, A., and Arístegui, J. (2017b). Anatomy of a subtropical intrathermocline eddy. *Deep Sea Res. Part I*.

Barton, E. D. (2001). *Encyclopedia of Ocean Sciences*, volume 3, chapter Island wakes, pages 1397–1403. Academic Press, London.

Barton, E. D. and Arístegui, J. (2004). The canary islands coastal transition zone – upwelling, eddies and filaments [editorial]. *Prog. Oceanogr.*, 62:67–69.

Barton, E. D., Arístegui, J., Tett, P., Canton, M., Garcia-Braun, J., Hernández-León, S., Nykjaer, L., Almeida, C., Almunia, J., Ballesteros, S., Basterretxea, G., Escánez, J., García-Weill, L., Hernández-Guerra, A., López-Laatzen, F., Molina, R., Montero, M. F., Navarro-Pérez, E., Rodríguez, J. M., van Lenning, K., Vélez, H., and Wild, K. (1998). The transition zone of the Canary Current upwelling region. *Prog. Oceanogr.*, 41(4):455–504.

Barton, E. D., Basterretxea, G., Flament, P., Mitchelson-Jacob, E. G., Jones, B., Arístegui, J., and Herrera, F. (2000). Lee region of Gran Canaria. *J. Geophys. Res.*, 105(C7):17173–17194.

Bashmachnikov, I., Neves, F., Calheiros, T., and Carton, X. (2015). Properties and pathways of Mediterranean water eddies in the Atlantic. *Progress in Oceanography*, 137:149–172.

Basterretxea, G., Barton, E. D., Tett, P., Sangrà, P., Navarro-Pérez, E., and Arístegui, J. (2002). Eddy and deep chlorophyl maximum response to wind-shear in the lee of Gran Canaria. *Deep-Sea Res.*, 49(6):1087–1101.

Bell, M. J., Schiller, A., Le Traon, P.-Y., Smith, N. R., Dombrowsky, E., and Wilmer-Becker, K. (2015). An introduction to GODAE OceanView. *Journal of Operational Oceanography*, 8(1):s2–s11.

Benítez-Barrios, V., Pelegrí, J. L., Hernández-Guerra, A., Lwiza, K. M. M., Gomis, D., Vélez-Belchí, P., and Hernández-León, S. (2011). Three-dimensional circulation in the NW Africa coastal transition zone. *Prog. Oceanogr.*, 91:516–533.

Bower, A. S. (1991). A simple kinematic mechanism for mixing fluid parcels across a meandering jet. *J. Phys. Oceanogr.*, 21(1):173–180.

Bretherton, F. P., Davis, R. E., and Fandry, C. B. (1976). A technique for objective analysis and design of oceanographic experiments applied to MODE73. *Deep Sea Res.*, 23(7):559–582.

Brink, K. H. and Robinson, A. R., editors (2005). *The Sea, Volume 11: The Global Coastal Ocean: Regional Studies and Syntheses*. Harvard University Press.

Brown, S. L., Landry, M. R., Selph, K. E., Jin Yang, E., Rii, Y. M., and Bidigare, R. R. (2008). Diatoms in the desert: Plankton community response to a mesoscale eddy in the subtropical North Pacific. *Deep-Sea Res.*, 55(10-13):1321–1333.

Buongiorno Nardelli, B. (2013). Vortex waves and vertical motion in a mesoscale cyclonic eddy. *J. Geophys. Res. Oceans*, 118:5609–5624.

Buongiorno Nardelli, B., Guinehut, S., Pascual, A., Drillet, Y., Ruiz, S., and Mulet, S. (2012). Towards high resolution mapping of 3-D mesoscale dynamics from observations. *Ocean Sci.*, 8:885–901.

Buongiorno Nardelli, B., Santoleri, R., and Sparnocchia, S. (2001). Small Mesoscale Features at a Meandering Upper-Ocean Front in the Western Ionian Sea (Mediterranean Sea): Vertical Motion and Potential Vorticity Analysis. *J. Phys. Oceanogr.*, 31:2227–2250.

Caldeira, R. M. A., Stegner, A., Couvelard, X., Araújo, I. B., Testor, P., and Lorenzo, A. (2014). Evolution of an oceanic anticyclone in the lee of Madeira Island: In situ and remote sensing survey. *J. Geophys. Res. Oceans*, 119.

Calil, P. H. R. and Richards, K. J. (2010). Transient upwelling hot spots in the oligotrophic North Pacific. *J. Geophys. Res.*, 115.

Capet, A., Mason, E., Rossi, V., Troupin, C., Faugère, Y., Pujol, I., and Pascual, A. (2014a). Geophysical Research Letters Volume 41, Issue 21, 16 November 2014, Pages 7602-7610 Implications of refined altimetry on estimates of mesoscale activity and eddy-driven offshore transport in the Eastern Boundary Upwelling Systems . *Geophys. Res. Lett.*, 41(21):7602–7610.

Capet, A., Mason, E., Rossi, V., Troupin, C., Faugère, Y., Pujol, I., and Pascual, A. (2014b). Implications of refined altimetry on estimates of mesoscale activity and eddy-driven offshore transport in the Eastern Boundary Upwelling Systems. *Geophys. Res. Lett.*, 41:7602–7610.

Capet, X. J., Campos, E. J., and Paiva, A. M. (2008). Submesoscale activity over the Argentinian shelf. *Geophys. Res. Lett.*, 35.

Cardona, Y. and Bracco, A. (2012). Enhanced vertical mixing within mesoscale eddies due to high frequency winds in the south china sea. *Ocean Modell.*

Carr, S. D., Capet, X. J., McWilliams, J. C., Pennington, J. T., and Chavez, F. P. (2008). The influence of diel vertical migration on zooplankton transport and recruitment in an upwelling region: estimates from a coupled behavioral-physical model. *Fish. Oceanogr.*, 17(1):1–15.

Carton, X., Daniault, N., Alves, J., Chérubin, L., and Ambar, I. (2010). Meddy dynamics and interaction with neighboring eddies southwest of Portugal: Observations and modeling. *J. Geophys. Res.*, 115:C06017.

Carton, X., Le Cann, B., Serpette, A., and Dubert, J. (2013). Interaction of surface and deep anticyclonic eddies in the Bay of Biscay. *J. Marine Systems*, 109-110, Supplement:S45–S59.

Chaigneau, A., Le Texier, M., Eldin, G., Grados, C., and Pizarro, O. (2011). Vertical structure of mesoscale eddies in the eastern South Pacific Ocean: A composite analysis from altimetry and Argo profiling floats. *Journal of Geophysical Research*, 116(C11025).

Chakraborty, A., Kumar, R., Basu, S., and Sharma, R. (2015). Improving Ocean State by Assimilating SARAL/AltiKa Derived Sea Level and Other Satellite-Derived Data in MITGCM. *Marine Geodesy*, 38(1):328–338.

Chavanne, C., Flament, P., Lumpkin, R., Dousset, B., and Bentamy, A. (2002). Scatterometer observations of wind variations induced by oceanic islands: Implications for wind-driven ocean circulation. *Can. J. Rem. Sens.*, 28(3):466–474.

Chelton, D. B., deSzoeke, R. A., Schlax, M. A., El Naggar, K., and Siwertz, N. (1998). Geographical variability of the first-baroclinic Rossby radius of deformation. *J. Phys. Oceanogr.*, 28(3):433–460.

Chelton, D. B., Gaube, P., Schlax, M. G., Early, J. J., and Samelson, R. M. (2011a). The Influence of Nonlinear Mesoscale Eddies on Near-Surface Oceanic Chlorophyll. *Science*, 334:328–332.

Chelton, D. B., Schlax, M. A., and Samelson, R. M. (2011b). Global observations of nonlinear mesoscale eddies. *Prog. Oceanogr.*, 91(2):167–216.

Chelton, D. B., Schlax, M. G., Samelson, R. M., and de Szoeke, R. A. (2007). Global observations of large oceanic eddies. *Geophys. Res. Lett.*, 34.

Chelton, D. B. and Xie, S.-P. (2010). Coupled ocean-atmosphere interaction at oceanic mesoscales. *Oceanography*, 23(4):52–69.

Chopra, K. P. (1973). *Advances in Geophysics*, volume 16, chapter Atmospheric and Oceanic Flow Problems Introduced By Islands, pages 297–421. Elsevier.

Clement, A. C. and Gordon, A. L. (1995). The absolute velocity field of Agulhas eddies and the Benguela Current. *J. Geophys. Res.*, 100(C11):22591–22601.

Danabasoglu, G., Bates, S., Briegleb, B., Jayne, S., Jochum, M., Large, W., Peacock, S., and Yeager, S. (2012). The ccsm4 ocean component. *J. Clim.*, 25:1361–1389.

Danabasoglu, G., Ferrari, R., and McWilliams, J. C. (2008). Sensitivity of an ocean general circulation model to a parameterization of near-surface eddy fluxes. *J. Clim.*, 21:1192–1208.

D'Asaro, E., Lee, C., Rainville, L., Harcourt, R., and Thomas, L. (2011). Enhanced Turbulence and Energy Dissipation at Ocean Fronts. *Science*, 332:318–322.

D'Asaro, E. A. (1988). Observations of small eddies in the Beaufort Sea. *J. Geophys. Res. Oceans*, 93(C6):6669–6684.

Davies-Jones, R. (1991). The Frontogenetical Forcing of Secondary Circulations. Part I: The Duality and Generalization of the Q Vector. *J. Atmos. Sci.*, 48:497–509.

Dibarboure, G., Pujol, M.-I. ., Briol, F., Le Traon, P.-Y., Larnicol, G., Picot, N., Mertz, F., and Ablain, M. (2011). Jason-2 in DUACS: Updated system description, first tandem results and impact on processing and products. *Marine Geodesy*, 34(3-4):214–241.

Ducet, N., Le Traon, P.-Y., and Reverdin, G. (2000). Global high-resolution mapping of ocean circulation from TOPEX/Poseidon and ERS-1 and -2. *J. Geophys. Res.*, 105(C8):19477–19498.

Dugan, J. P., Mied, R. P., Mignerey, P. C., and Schuetz, A. F. (1982). Compact, intrathermocline eddies in the Sargasso Sea. *J. Geophys. Res.*, 87(C1):385–393.

Durran, D. R. and Snellman, L. W. (1987). The Diagnosis of Synoptic-Scale Vertical Motion in an Operational Environment. *Weather and Forecasting*, 2(1):17–31.

Eppley, R. W., Rogers, J. N., and McCarthy, J. J. (1969). Half-saturation constants for uptake of nitrate and ammonium by marine phytoplankton. *Limnology and oceanography*, 14(6):912–920.

Feistel, R. (2003). A new extended Gibbs thermodynamic potential of seawater. *Prog. Oceanogr.*, 58(1):43–114.

Feistel, R. (2008). A Gibbs function for seawater thermodynamics for -6 to 80^{o}C and salinity up to 120g kg^{-1}. *Deep Sea Res. Part I: Oceanographic Research Papers*, 55(12):1639–1671.

Firing, E., Ranada, J., and Caldwell, P. (1995). Processing ADCP data with the CODAS software system version 3.1. *Joint Institute for Marine and Atmospheric Research, University of Hawaii & National Oceanographic Data Center.*

Flierl, G. R. (1981). Particle motions in largeamplitude wave fields. *Geophys. Astrophys. Fluid Dyn.*, 18:39–74.

Fu, L.-L. and Ferrari, R. (2008). Observing Oceanic Submesoscale Processes From Space. *Eos Trans. AGU*, 89(48):488–488.

Garcia-Soto, C., Pingree, R. D., and Valdés, L. (2002). Navidad development in the southern bay of biscay: climate change and swoddy structure from remote sensing and in situ measurements. *J. Geophys. Res.*, 107(3118).

Gaube, P., Chelton, D. B., Samelson, R. M., Schlax, M. G., and O'neill, L. W. (2015). Satellite Observations of Mesoscale Eddy-Induced Ekman Pumping. *J. Phys. Oceanogr.*, 45:104–132.

Gaube, P., Chelton, D. B., Strutton, P. G., and Behrenfeld, M. J. (2013). Satellite observations of chlorophyll, phytoplankton biomass, and Ekman pumping in nonlinear mesoscale eddies. *Journal of Geophysical Research*, 118:6349–6370.

Gaube, P., McGillicuddy Jr., D. J., Chelton, D. B., Behrenfeld, M. J., and Strutton, P. G. (2014). Regional variations in the influence of mesoscale eddies on near-surface chlorophyll. *J. Geophys. Res. Oceans*, 119:8195–8220.

Giordani, H., Prieur, L., and Caniaux, G. (2006). Advanced insights into sources of vertical velocity in the ocean. *Ocean Dynam.*, 56(5-6):513–524.

Gomis, D., Ruiz, S., and Pedder, M. A. (2001). Diagnostic analysis of the 3D ageostrophic circulation from a multivariate spatial interpolation of CTD and ADCP data. *Deep-Sea Research Part I: Oceanographic Research Papers*, 48:269–295.

Gordon, A. L., Giulivi, C. F., Lee, C. M., Furey, H. H., Bower, A., and Talley, L. (2002). Japan/East Sea Intrathermocline Eddies. *J. Phys. Oceanogr.*, 32:1960–1974.

Griffies, S. M. (2004). *Fundamentals of Ocean Climate Models*. Princeton University Press.

Guinehut, S., Dhomps, A.-L., Larnicol, G., and Le Traon, P.-Y. (2012). High resolution 3-d temperature and salinity fields derived from in situ and satellite observation. *Ocean Sci.*, 8:845–857.

Hanawa, K. and Talley, L. D. (2001). *Ocean Circulation and Climate*, chapter Mode Waters, pages 373–386. Academic Press.

Hansen, C., Kvaleberg, E., and Samuelsen, A. (2010). Anticyclonic eddies in the Norwegian Sea; their generation, evolution and impact on primary production. *Deep-Sea Res.*, 57:1079–1091.

Hansen, D. V. and Paul, C. A. (1987). Vertical motion in the Eastern equatorial Pacific inferred from drifting buoys. *Oceanologica Acta*, (Special issue):27–32.

Harcourt, R. R., Steffen, E. L., Garwood, R. W., and D'Asaro, E. A. (2002). Fully Lagrangian Floats in Labrador Sea Deep Convection: Comparison of Numerical and Experimental Results. *J. Phys. Oceanogr.*, 32(2):493–510.

Hebert, D. (1988). The Available Potential Energy of An Isolated Feature . *J. Geophys. Res.*, 93(C1):556–564.

Hebert, D., Oakey, N., and Ruddick, B. (1990). Evolution of a Mediterranean Salt Lens: Scalar Properties. *J. Phys. Oceanogr.*, 20:1468–1483.

Hernandez, F., Blockley, E., Brassington, G. B., Davidson, F., Divakaran, P., Drévillon, M., Ishizaki, S., Garcia-Sotillo, M., Hogan, P. J., Lagemaa, P., Levier, B., Martin, M., Mehra, A., Mooers, C., Ferry, N., Ryan, A., C., R., Sellar, A., Smith, G. C., Sofianos, S., Spindler, T., Volpe, G., Wilkin, J., Zaron, E. D., and Zhang, A. (2015). Recent progress in performance evaluations and near real-time assessment of operational ocean products. *Journal of Operational Oceanography*, 8(2):s221–s238.

Hernández-Guerra, A., Arístegui, J., Cantón, M., and Nykjaer, L. (1993). Phytoplankton pigment patterns in the Canary Islands area as determined using Coastal Zone Colour Scanner data. *Int. J. Rem. Sens.*, 14(7):1431–1437.

Hogan, P. J. and Hurlburt, H. E. (2006). Why do IntraThermocline Eddies Form in the Japan/East Sea? A Modeling Perspective. *Oceanography*, 19(3):134–143.

Holm-Hansen, O., Lorenzen, C. J., Holmes, R. W., and Strickland, J. D. H. (1965). Fluorometric determination of chlorophyll. *J. Cons. Int. Explor. Mer*, 30(1):3–15.

Hormazabal, S., Combes, V., Morales, C. E., Correa-Ramirez, M. A., Di Lorenzo, E., and Nuñez, S. (2013). Intrathermocline eddies in the coastal transition zone off central chile (31-–41°S). *J. Geophys. Res.*, 118:1–11.

Hoskins, B. J. and Bretherton, F. P. (1972). Atmospheric frontogenesis models: Mathematical formulation and solution. *J. Atmos. Sci.*, 29:11–37.

Hoskins, B. J. and Draghici, I. (1977). The Forcing of Ageostrophic Motion According to the Semi-Geostrophic Equations and in an Isentropic Coordinate Model. *J. Atmos. Sci.*, 34(12):1859–1897.

Hoskins, B. J., Draghici, I., and Davies, H. C. (1978). A new look at the ω-equation. *Quart. J. R. Met. Soc.*, 104:31–38.

Imawaki, S., Bower, A. S., Beal, L., and Qiu, B. (2013). Chapter 13 - western boundary currents. In Gerold Siedler, Stephen M. Griffies, J. G. and Church, J. A., editors, *Ocean Circulation and Climate A 21st Century Perspective*, volume 103 of *International Geophysics*, pages 305 – 338. Academic Press.

Jiménez, B., Sangrà, P., and Mason, E. (2008). A numerical study of the relative importance of wind and topographic forcing on oceanic eddy shedding by tall deep water islands. *Ocean Modell.*, 22(3-4):146–157.

Jochum, M., Danabasoglu, G., Holland, M., Kwon, Y.-O., and Large, W. G. (2008). Ocean viscosity and climate. *J. Geophys. Res.*, 113(C6):C06017.

José, Y. S., Aumont, O., Machu, E., Penven, P., Moloney, C. L., and Maury, O. (2014). Influence of mesoscale eddies on biological production in the Mozambique Channel: Several contrasted examples from a coupled ocean-biogeochemistry model. *Deep Sea Res.*, 100:79–93.

Kahru, M., Mitchell, B. G., Gille, S. T., Hewes, C. D., and Holm-Hansen, O. (2007). Eddies enhance biological production in the Weddell-Scotia Confluence of the Southern Ocean. *Geophys. Res. Lett.*, 34(L14603).

Käse, R. H., Zenk, W., Sanford, T. B., and Hiller, W. (1985). Currents, fronts and eddy fluxes in the Canary Basin. *Prog. Oceanogr.*, 14:231–257.

Kaurkin, M. N., Ibrayev, R. A., and Belyaev, K. P. (2016). ARGO data assimilation into the ocean dynamics model with high spatial resolution using Ensemble Optimal Interpolation (EnOI). *Oceanology*, 56(6):774–781.

Klein, B. and Seidler, G. (1989). On the origin of the Azores Current. *J. Geophys. Res.*, 94:6159–6168.

Klein, P. and Lapeyre, G. (2009). The Oceanic Vertical Pump Induced by Mesoscale and Submesoscale Turbulence. *Annu. Rev. Marine Sci.*, 1:351–375.

Kloosterziel, R. and van Heijst, G. (1991). An experimental study of unstable barotropic vortices in a rotating fluid. *J. Fluid Mech.*, 223:1–24.

Koszalka, I., Bracco, A., McWilliams, J. C., , and Provenzale, A. (2009). Dynamics of wind-forced coherent anticyclones in the open ocean. *J. Geophys. Res. Oceans*, 114(C8).

Koszalka, I., Ceballos, L., and Bracco, A. (2010). Vertical mixing and coherent anticyclones in the ocean: the role of stratification. *Nonlinear Process. Geophys.*, 17(1):37–47.

La Violette, P. E. (1974). A Satellite-Aircraft Thermal Study of the Upwelled Waters off Spanish Sahara. *J. Phys. Oceanogr.*, 4(4):676–684.

Large, W. G. (1979). *The Turbulent Fluxes of Momentum and Sensible Heat over the Open Sea during Moderate to Strong Winds*. PhD thesis, University of British Columbia.

Lasternas, S., Piedeleu, M., Sangrà, P., Duarte, C. M., and Agustí, S. (2013). Forcing of dissolved organic carbon release by phytoplankton by anticyclonic mesoscale eddies in the subtropical NE Atlantic Ocean. *Biogeosciences*, 10:2129–2143.

Lathuiliere, C., Levy, M., and Echevin, V. (2011). Impact of eddy-driven vertical fluxes on phytoplankton abundance in the euphotic layer. *Journal of Plankton Research*, 33:827–831.

Le Traon, P.-Y. (1990). A method for optimal analysis of fields with spatially-variable mean. *J. Geophys. Res.*, 95:13543–13547.

Le Traon, P.-Y., Antoine, D., Bentamy, A., Bonekamp, H., Breivik, L. A., Chapron, B., Corlett, G., Dibarboure, G., DiGiacomo, P., Donlon, C., Faugère, Y., Font, J., Girard-Ardhuin, F., Gohin, F., Johannessen, J. A., Kamachi, M., Lagerloef, G., Lambin, J., Larnicol, G., Le Borgne, P., Leuliette, E., Lindstrom, E., Martin, M. J., Maturi, E., Miller, L., Mingsen, L., Morrow, R., Reul, N., Rio, M. H., Roquet, H., Santoleri, R., and Wilkin, J. (2015). Use of satellite observations for operational oceanography: recent achievements and future prospects. *Journal of Operational Oceanography*, 8(1).

Lévy, M., Klein, P., and Treguier, A. M. (2001). Impact of sub-mesoscale physics on production and subduction of phytoplankton in an oligotrophic regime. *Journal of Marine Research*, 59(4):535–565.

L'Hégaret, P., Carton, X., Ambar, I., Ménesguen, C., Lien Hua, B., Chérubin, L., Aguiar, A., Le Cann, B., Daniault, N., and Serra, N. (2014). Evidence of Mediterranean Water dipole collision in the Gulf of Cadiz. *J. Geophys. Res. Oceans*, 119:5337–5359.

Lindstrom, S. S. and Watts, D. P. (1994). Vertical Motion in the Gulf Stream Near 68^{o}W. *J. Phys. Oceanogr.*, 24(11):2321–2333.

MacIsaac, J. and Dugdale, R. (1972). Interactions of light and inorganic nitrogen in controlling nitrogen uptake in the sea. In *Deep Sea Research and Oceanographic Abstracts*, volume 19, pages 209–232. Elsevier.

Mahadevan, A. (2014). Eddy effects on biogeochemistry. *Nature*, 506:168–169.

Mahadevan, A. (2016). The Impact of Submesoscale Physics on Primary Productivity of Plankton. *Annu. Rev. Mar. Sci.*, 8:161–184.

Mahadevan, A. and Archer, D. (2000). Modeling the impact of fronts and mesoscale circulation on the nutrient supply and biogeochemical of the upper ocean. *J. Geophys. Res.*, 105(C1):1209–1225.

Mahadevan, A., D'Asaro, E., Lee, C., and Perry, M. J. (2012). Eddy-driven stratification initiates North Atlantic spring phytoplankton blooms. *Science*, 336:54–58.

Mahadevan, A. and Tandon, A. (2006). An analysis of mechanisms for submesoscale vertical motion at ocean fronts. *Ocean Modell.*, 14(3-4):241–256.

Mahadevan, A., Thomas, L. N., and Tandon, A. (2008). Comment on "Eddy/Wind Interactions Stimulate Extraordinary Mid-Ocean Plankton Blooms". *Science*, 320.

Marra, J. F., Lance, V. P., Vaillancourt, R. D., and Hargreaves, B. R. (2014). Resolving the ocean's euphotic zone. *Deep Sea Res. Part I: Oceanographic Research Papers*, 83:45–50.

Martin, A. P. and Richards, K. J. (2001). Mechanisms for vertical nutrient transport within a North Atlantic mesoscale eddy. *Deep-Sea Research Part II: Topical Studies in Oceanography*, 48:757–773.

Mason, E., Colas, F., Molemaker, M. J., Shchepetkin, A. F., Troupin, C., McWilliams, J. C., and Sangrà, P. (2011). Seasonal variability of the Canary Current: a numerical study. *J. Geophys. Res.*, 116.

Mason, E., Colas, F., and Pelegrí, J. L. (2012). A Lagrangian study tracing water parcel origins in the Canary Upwelling System. *Sci. Mar.*, 76(S1):79–94.

Mason, E., Pascual, A., Gaube, P., Ruiz, S., Pelegrí, J. L., and Delepoulle, A. (2017). Subregional characterization of mesoscale eddies across the brazil-malvinas confluence. *J. Geophys. Res. Oceans*.

McGillicuddy, D. J. (2015). Formation of Intrathermocline Lenses by Eddy–Wind Interaction. *J. Phys. Oceanogr.*, 45:606–612.

McGillicuddy, D. J. (2016). Mechanisms of Physical-Biological-Biogeochemical Interaction at the Oceanic Mesoscale. *Annual Review of Marine Science*, 8:125–159.

McGillicuddy, D. J., Anderson, L. A., Bates, N. R., Bibby, T., Buesseler, K. O., Carlson, C. A., Davis, C. S., Ewart, C., Falkowski, P. G., Goldthwait, S. A., Hansell, D. A., Jenkins, W. J., Johnson, R., Kosnyrev, V. K., Ledwell, J. R., Li, Q. P., Siegel, D. A., and Steinberg, D. K. (2007). Eddy Wind interactions stimulate extraordinary mid-ocean plankton blooms. *Science*, 316:1021–1026.

McGillicuddy, D. J., Ledwell, J. R., and Anderson, L. A. (2008). Response to Comment on "Eddy/Wind Interactions Stimulate Extraordinary Mid-Ocean Plankton Blooms". *Science*, 320(448c).

McGillicuddy, D. J., Robinson, A. R., Siegel, D. A., Jannasch, H. W., Johnson, R., Dickey, T. D., McNeil, J., Michaels, A. F., and Knap, A. H. (1998). Influence of mesoscale eddies on new production in the Sargasso Sea. *Nature*, 394:263–266.

McWilliams, J. C. (1985). Submesoscale, Coherent Vortices in the Ocean. *Rev. Geophys.*, 23(2):165–182.

McWilliams, J. C. (2008). *Ocean Modeling in an Eddying Regime*, chapter The Nature and Consequences of Oceanic Eddies. American Geophysical Union.

McWilliams, J. C., Graves, L. P., and Montgomery, M. T. (2003). A Formal Theory for Vortex Rossby Waves and Vortex Evolution. *Geophysical & Astrophysical Fluid Dynamics*, 97(4):275–309.

Mittelstaedt, E. (1991). The ocean boundary along the northwest African coast: Circulation and oceanographic properties at the sea surface. *Prog. Oceanogr.*, 26(4):307–355.

Mizobata, K., Saitoh, S. I., Shiomoto, A., Miyamura, T., Shiga, N., Imai, K., Toratani, M., Kajiwara, Y., and Sasaoka, K. (2002). Bering Sea cyclonic and anticyclonic eddies observed during summer 2000 and 2001. *Prog. Oceanogr.*, 55:65–75.

Morel, A., Claustre, H., and Gentili, B. (2010). The most oligotrophic subtropical zones of the global ocean: similarities and differences in terms of chlorophyll and yellow substance. *Biogeosciences*, 7:3139–3151.

Mulet, S., Rio, M.-H., Mignot, A., Guinehut, S., and Morrow, R. (2012). A new estimate of the global 3D geostrophic ocean circulation based on satellite data and in-situ measurements. *Deep-Sea Research Part II: Topical Studies in Oceanography*, 77-80:70–81.

Nagai, T., Tandon, A., and Rudnick, D. L. (2006). Two-dimensional ageostrophic secondary circulation at ocean fronts due to vertical mixing and large-scale deformation. *J. Geophys. Res.*, 111(C9).

Nauw, J. J., van Aken, H. M., Lutjeharms, J. R. E., and de Ruijter, W. P. M. (2006). Intrathermocline eddies in the Southern Indian Ocean. *J. Geophys. Res.*, 111(C03006).

Naveira Garabato, A. C., Leach, H., Allen, J. T., Pollard, R. T., and Strass, V. H. (2001). Mesoscale Subduction at the Antarctic Polar Front Driven by Baroclinic Instability. *J. Phys. Oceanogr.*, 31(8):2087–2107.

Oka, E. (2009). Seasonal and Interannual Variation of North Pacific Sub- tropical Mode Water in 2003–2006. *Journal of Oceanography*, 65:151–164.

Olson, D. B., Schmitt, R. W., Kennelly, M., and Joyce, T. M. (1985). A two-layer diagnostic model of the long-term physical evolution of warm-core ring 82B. *J. Geophys. Res. Oceans*, 90(C5):8813–8822.

Omand, M. M. and Mahadevan, A. (2015). The shape of the oceanic nitracline. *Biogeosciences*, 12:3273–3287.

Pacheco, M. M. and Hernández-Guerra, A. (1999). Seasonal variability of recurrent phytoplankton pigment patterns in the Canary Islands area. *Int. J. Rem. Sens.*, 20(7):1405–1418.

Pallàs-Sanz, E., Johnston, T. M. S., and Rudnick, D. L. (2010a). Frontal dynamics in a California Current System shallow front: 1. Frontal processes and tracer structure. *J. Geophys. Res.*, 115(C12067):1–14.

Pallàs-Sanz, E., Johnston, T. M. S., and Rudnick, D. L. (2010b). Frontal dynamics in a California Current System shallow front: 2. Mesoscale vertical velocity. *J. Geophys. Res.*, 115(C12068):1–13.

Pallàs-Sanz, E. and Viúdez, A. (2005). Diagnosing Mesoscale Vertical Motion from Horizontal Velocity and Density Data. *J. Phys. Oceanogr.*, 35(10):1744–1762.

Pallàs-Sanz, E. and Viúdez, A. (2007). Three-Dimensional Ageostrophic Motion in Mesoscale Vortex Dipoles. *J. Phys. Oceanogr.*, 37(1):84–105.

Pascual, A., Faugère, Y., Larnicol, G., and Le Traon, P.-Y. (2006). Improved description of the ocean mesoscale variability by combining four satellite altimeters. *Geophys. Res. Lett.*, 33.

Pascual, A., Gomis, D., Haney, R. L., and Ruiz, S. (2004). A Quasigeostrophic Analysis of a Meander in the Palamos Canyon: Vertical Velocity, Geopotential Tendency, and a Relocation Technique. *J. Phys. Oceanogr.*, 34(10):2274–2287.

Pascual, A., Ruiz, S., Buongiorno Nardelli, B., Guinehut, S., Iudicone, D., and Tintoré, J. (2015). Net primary production in the Gulf Stream sustained by quasigeostrophic vertical exchanges. *Geophys. Res. Lett.*, 42(2):441–449.

Pascual, A., Ruiz, S., Olita, A., Troupin, C., Claret, M., Casas, B., Mourre, B., Poulain, P.-M., Tovar-Sanchez, A., Capet, A., Mason, E., Allen, J. T., Mahadevan, A., and Tintoré, J. (2017). A Multiplatform Experiment to Unravel Meso- and Submesoscale Processes in an Intense Front (AlborEx). *Front. Mar. Sci.*, 4:39.

Pedder, M. A. and Thorpe, A. J. (1999). The semi-geostrophic diagnosis of vertical motion. I: Formulation and coordinate transformations. *Quart. J. R. Met. Soc.*, 125(556):1231–1256.

Pegliasco, C., Chaigneau, A., and Morrow, R. (2015). Main eddy vertical structures observed in the four major Eastern Boundary Upwelling Systems. *J. Geophys. Res.*, 120:6008—-6033.

Pelegrí, J. L., Arístegui, J., Cana, L., González-Dávila, M., Hernández-Guerra, A., Hernández-León, S., Marrero-Díaz, A., Montero, M. F., Sangrà, P., and Santana-Casiano, M. (2005). Coupling between the open ocean and the coastal upwelling region off northwest Africa: water recirculation and offshore pumping of organic matter. *J. Mar. Syst.*, 54(1-4):3–37.

Pelland, N. A., Eriksen, C. C., and Lee, C. M. (2013). Subthermocline Eddies over the Washington Continental Slope as Observed by Seagliders, 2003–09. *J. Phys. Oceanogr.*, 43:2025–2053.

Penven, P., Marchesiello, P., Debreu, L., and Lefèvre, J. (2008). Software tools for pre- and post-processing of oceanic regional simulations. *Environmental Modelling and Software*, 23:660–662.

Pidcock, R., Martin, A., Allen, J., Painter, S. C., and Smeed, D. (2013). The spatial variability of vertical velocity in an iceland basin eddy dipole. *Deep-Sea Res.*, 72:121–140.

Piedeleu, M., Sangrà, P., Sánchez-Vidal, A., Fabrés, J., Gordo, C., and Calafat, A. (2009). An observational study of oceanic eddy generation mechanisms by tall deep-water islands (Gran Canaria). *Geophys. Res. Lett.*, 36.

Pingree, R. D. (1996). A Shallow Subtropical Subducting Westward Propagating Eddy (Swesty). *Philosophical Transactions: Mathematical, Physical and Engineering Sciences*, 354(1710):979–1026.

Pingree, R. D. and Le Cann, B. (1992a). Anticyclonic Eddy X91 in the Southern Bay of Biscay, May 1991 to February 1992. *J. Geophys. Res.*, 97(c9):14353–14367.

Pingree, R. D. and Le Cann, B. (1992b). Three anticyclonic slope water oceanic eddies (swoddies) in the southern bay of biscay in 1990. *Deep-Sea Res.*, 39(7-8):1147–1175.

Pinot, J.-M., Tintoré, J., and Wang, D.-P. (1996). A study of the omega equation for diagnosing vertical motions at ocean fronts. *Journal of Marine Research*, 54(2):239–259.

Pollard, R. T. and Regier, L. A. (1992). Vorticity and Vertical Circulation at an Ocean Front. *J. Phys. Oceanogr.*, 22:609–625.

Prater, M. D. and Sanford, T. B. (1994). A Meddy off Cape St. Vincent. Part I: Description. *J. Phys. Oceanogr.*, 24:1572–1586.

Pujol, M.-I., Faugère, Y., Taburet, G., Dupuy, S., Pelloquin, C., Ablain, M., and Picot, N. (2016). DUACS DT2014: the new multi-mission altimeter data set reprocessed over 20 years. *Ocean Sci.*, 12(5):1067–1090.

Qiu, B. and Chen, S. (2004). Seasonal modulations in the Eddy Field of the South Pacific Ocean. *J. Phys. Oceanogr.*, 34(7):1515–1527.

Qiu, B., Scott, R. B., and Chen, S. (2008). Length Scales of Eddy Generation and Nonlinear Evolution of the Seasonally Modulated South Pacific Subtropical Countercurrent. *J. Phys. Oceanogr.*, 38(7):1515–1528.

Ras, J., Claustre, H., and Uitz, J. (2008). Spatial variability of phytoplankton pigment distributions in the Subtropical South Pacific Ocean: Comparison between in situ and predicted data. *Biogeosciences*, 5:353–369.

Rodríguez, J., Tintoré, J., Allen, J. T., Blanco, J. M., Gomis, D., Reul, A., Ruiz, J., Rodríguez, V., Echevarría, F., and Jiménez-Gómez, F. (2001). Mesoscale vertical motion and the size structure of phytoplankton in the ocean. *Nature*, 410:360–363.

Rudnick, D. L. (1996). Intensive surveys of the Azores Front: 2. Inferring the geostrophic and vertical velocity fields. *J. Geophys. Res. Oceans*, 101(C7):16291–16303.

Ruiz, S., Pascual, A., Garau, B., Pujol, M.-I. ., and Tintoré, J. (2009). Vertical motion in the upper ocean from glider and altimetry data. *Geophys. Res. Lett.*, 36.

Ruiz, S., Pelegrí, J. L., Emelianov, M., Pascual, A., and Mason, E. (2014). Geostrophic and ageostrophic circulation of a shallow anticyclonic eddy off cape bojador. *J. Geophys. Res. Oceans*, 119(2):1257–1270.

Sánchez, R. and Gil, J. (2004). 3D structure, mesoscale interactions and potential vorticity conservation in a swoddy in the Bay of Biscay. *J. Marine Systems*, 46:47–68.

Sangrà, P., Auladell, M., Marrero-Díaz, A., Pelegrí, J. L., Fraile-Nuez, E., Rodríguez-Santana, A., Martín, J. M., Mason, E., and Hernández-Guerra, A. (2007). On the nature of oceanic eddies shed by the island of Gran Canaria. *Deep-Sea Res.*, 54(5):687–709.

Sangrà, P., Pascual, A., Rodríguez-Santana, A., Machín, F., Mason, E., McWilliams, J. C., Pelegrí, J. L., Dong, C., Rubio, A., Arístegui, J., Marrero-Díaz, A., Hernández-Guerra, A., Martínez-Marrero, A., and Auladell, M. (2009). The Canary Eddy Corridor: a major pathway for long-lived eddies in the subtropical North Atlantic. *Deep-Sea Res.*, 56:2100–2114.

Sangrà, P., Pelegrí, J. L., Hernández-Guerra, A., Arregui, I., Martín, J. M., Marrero-Díaz, A., Martínez, A., Ratsimandresy, A. W., and Rodríguez-Santana, A. (2005). Life history of an anti-cyclonic eddy. *J. Geophys. Res.*, 110.

Sato, O. T. and Polito, P. S. (2014). Observation of South Atlantic subtropical mode waters with Argo profiling float data. *J. Geophys. Res. Oceans*, 119:2860–2881.

Schiller, A. and Brassington, G. B., editors (2011). *Operational Oceanography in the 21st Century*. Springer Netherlands, 1 edition.

Schmid, C., Schäfer, H., Zenk, W., and Podestá, G. (1995). The Vitória Eddy and Its Relation to the Brazil Current. *J. Phys. Oceanogr.*, 25:2532–2546.

Schultz Tokos, K. and Rossby, T. (1991). Kinematics and dynamics of a mediterranean salt lens. *J. Phys. Oceanogr.*, 21:879–892.

Schultz Tokos, K. L., Hinrichsen, H.-H., and Zenk, W. (1994). Merging and Migration of Two Meddies. *J. Phys. Oceanogr.*, 24(10):2129–2141.

Schütte, F., Brandt, P., and Karstensen, J. (2015). Occurrence and characteristics of mesoscale eddies in the tropical northeast Atlantic Ocean. *Ocean Sci. Discuss.*, 12:3043–3097.

Shapiro, G. I., Zenk, W., Meschanov, S. L., and Schultz Tokos, K. L. (1995). Self-similarity of the meddy family in the eastern north atlantic. *Oceanologica Acta*, 18(1):29–42.

Shcherbina, A. Y., Sundermeyer, M. A., Kunze, E., D'Asaro, E., Badin, G., Birch, D., Brunner-Suzuki, A.-M. E. G., Callies, J., Cervantes, B. T. K., Claret, M., Concannon, B., Early, J., Ferrari, R., Goodman, L., Harcourt, R. R., Klymak, J. M., Lee, C. M., Lelong, M.-P., Levine, M. D., Lien, R.-C., Mahadevan, A., McWilliams, J. C., Molemaker, M. J., Mukherjee, S., Nash, J. D., Özgökmen, T., Pierce, S. D., Ramachandran, S., Samelson, R. M., Sanford, T. B., Shearman, R. K., Skyllingstad, E. D., Smith, K. S., Tandon, A., Taylor, J. R., Terray, E. A., Thomas, L. N., and Ledwell, J. R. (2015). The latmix summer campaign: Submesoscale stirring in the upper ocean. *Bulletin of the American Meteorological Society*, 96(8):1257–1279.

Shearman, R. K., Barth, J. A., Allen, J. S., and Haney, R. L. (2000). Diagnosis of the Three-Dimensional Circulation in Mesoscale Features with Large Rossby Number. *J. Phys. Oceanogr.*, 30(11):2687–2709.

Siedler, G., Kuhl, A., and Zenk, W. (1987). The madeira mode water. *J. Phys. Oceanogr.*, 17:1561–1570.

Siegel, D. A., Court, D. B., Menzies, D. W., Peterson, P., Maritorena, S., and Nelson, N. B. (2008). Satellite and in situ observations of the bio-optical signatures of two mesoscale eddies in the Sargasso Sea. *Deep-Sea Research Part II: Topical Studies in Oceanography*, 55:1218–1230.

Siegel, D. A., McGillicuddy, D. J., and Fields, E. A. (1999). Mesoscale eddies, satellite altimetry, and new production in the Sargasso Sea. *Journal of Geophysical Research C: Oceans*, 104:13359–13379.

Skamarock, W. C., Klemp, J. B., Dudhia, J., Gill, D. O., Barker, D. M., Duda, M. G., Xiang-Yu, H., Wang, W., and Powers, J. G. (2008). A Description of the Advanced Research WRF Version 3. Technical report, NCAR, Boulder, Colorado, USA.

Sotillo, M. G., Amo-Balandrón, A., Padorno, E., Garcia-Ladona, E., Orfila, A., Rodríguez-Rubio, P., Conti, D., Jiménez Madrid, J. A., de los Santos, F. J., and Alvarez Fanjul, E. (2016). How is the surface Atlantic water inflow through the Gibraltar Strait forecasted? A lagrangian validation of operational oceanographic services in the Alboran Sea and the Western Mediterranean. *Deep Sea Res. Part II: Tropical Studies in Oceanography*, 133:100–117.

Spall, M. A. (1997). Baroclinic jets in confluent flow. *J. Phys. Oceanogr.*, 27:1054–1071.

Stern, M. E. (1965). Interaction of a uniform wind stress with a geostrophic vortex. *Deep Sea Res.*, 12(3):355–367.

Stramma, L., Bange, H. W., Czeschel, R., Lorenzo, A., and Frank, M. (2013). On the role of mesoscale eddies for the biological productivity and biogeochemistry in the eastern tropical Pacific Ocean off Peru. *Biogeosciences*, 10:7293–7306.

Strub, P. T., Combes, V., Shillington, F. A., and Pizarro, O. (2013). Chapter 14 - currents and processes along the eastern boundaries. In Gerold Siedler, Stephen M. Griffies, J. G. and Church, J. A., editors, *Ocean Circulation and Climate A 21st Century Perspective*, volume 103 of *International Geophysics*, pages 339 – 384. Academic Press.

Thomas, L. N. (2008). Formation of intrathermocline eddies at ocean fronts by wind-driven destruction of potential vorticity. *Dynam. Atmos. Oceans*, 45:252–273.

Thomas, L. N., Lee, C. M., and Yoshikawa, Y. (2010). The Subpolar Front of the Japan/East Sea. Part II: Inverse Method for Determining the Frontal Vertical Circulation. *J. Phys. Oceanogr.*, 40(1):3–25.

Tintoré, J., Gomis, D., Alonso, S., and Parrilla, G. (1991). Mesoscale Dynamics and Vertical Motion in the Alborán Sea. *J. Phys. Oceanogr.*, 21(6):811–823.

Trenberth, K. E. (1978). On the Interpretation of the Diagnostic Quasi-Geostrophic Omega Equation. *Monthly Weather Review*, 106(1):131–137.

Viúdez, A. and Dritschel, D. G. (2003). Vertical velocity in mesoscale geophysical flows. *J. Fluid Mech.*, 483:199–223.

Viúdez, A. and Dritschel, D. G. (2004). Potential Vorticity and the Quasigeostrophic and Semigeostrophic Mesoscale Vertical Velocity. *J. Phys. Oceanogr.*, 34(4):865–887.

Viúdez, A., Tintoré, J., and Haney, R. L. (1996). About the Nature of the Generalized Omega Equation. *Journal of the Atmospheric Sciences*, 53(5):787–795.

Weller, R. A., Furey, P. W. Spall, M. A., and Davis, R. E. (2004). The large-scale context for oceanic subduction in the Northeast Atlantic. *Deep-Sea Res.*, 51(5):665–699.

Woods, J. (1988). *Toward a Theory on Biological-Physical Interactions in the World Ocean*, chapter Scale Upwelling and Primary Production, pages 7–38. Springer Netherlands.

Xu, L., Li, P., Xie, S., Liu, Q., Liu, C., and Gao, W. (2016). Observing mesoscale eddy effects on mode-water subduction and transport in the North Pacific. *Nature Communications*, 7:10505.

Xu, Q. (1992). Ageostrophic Pseudovorticity and Geostrophic C-Vector Forcing—A New Look at the Q Vector in Three Dimensions. *J. Atmos. Sci.*, 49:981–990.